

REPORT DOCUMENTATION PAGE

1a. REPORT SECURITY CLASSIFICATION UNCLASSIFIED			1b. RESTRICTIVE MARKINGS UNCLASSIFIED		
2a. SECURITY CLASSIFICATION AUTHORITY			3. DISTRIBUTION / AVAILABILITY OF REPORT Approved for public release; distribution unlimited.		
2b. DECLASSIFICATION / DOWNGRADING SCHEDULE					
4. PERFORMING ORGANIZATION REPORT NUMBER(S) SIO REFERENCE 87-28			5. MONITORING ORGANIZATION REPORT NUMBER(S)		
6a. NAME OF PERFORMING ORGANIZATION Marine Physical Laboratory		6b. OFFICE SYMBOL (If applicable) MPL	7a. NAME OF MONITORING ORGANIZATION Office of Naval Research Department of the Navy		
6c. ADDRESS (City, State, and ZIP Code) University of California, San Diego Scripps Institution of Oceanography San Diego, CA 92152			7b. ADDRESS (City, State, and ZIP Code) 800 North Quincy Street Arlington, VA 22217-5000		
8a. NAME OF FUNDING / SPONSORING ORGANIZATION Office of Naval Research		8b. OFFICE SYMBOL (If applicable) ONR	9. PROCUREMENT INSTRUMENT IDENTIFICATION NUMBER N00014-80-C-0220		
8c. ADDRESS (City, State, and ZIP Code) Department of the Navy 800 North Quincy Street Arlington, VA 22217-5000			10. SOURCE OF FUNDING NUMBERS		
			PROGRAM ELEMENT NO.	PROJECT NO.	TASK NO.
					WORK UNIT ACCESSION NO.
11. TITLE (Include Security Classification) VELOCITY AND ATTENUATION PROFILES IN THE MONTEREY DEEP-SEA FAN					
12. PERSONAL AUTHOR(S) Richard K. Brienzo					
13a. TYPE OF REPORT Ph.D. Dissertation		13b. TIME COVERED FROM _____ TO _____		14. DATE OF REPORT (Year, Month, Day) December 1987	15. PAGE COUNT 101 pages
16. SUPPLEMENTARY NOTATION					
17. COSATI CODES			18. SUBJECT TERMS (Continue on reverse if necessary and identify by block number)		
FIELD	GROUP	SUB-GROUP			
			seismic refraction, velocity and attenuation profiles, Monterey Deep-Sea Fan, 20-element vertical array,		
19. ABSTRACT (Continue on reverse if necessary and identify by block number)					
<p>Data obtained during a refraction experiment is used to estimate velocity and attenuation profiles in an area of thick sediments (2.5 - 3 km) on the Monterey Deep-Sea Fan. A 20 element vertical hydrophone array was deployed at mid-depth in 2800 meters of water. Explosive sources, set for a depth of 1820 meters, were detonated at ranges between 3.5 km to 37 kilometers from the array. Estimates of velocity as a function of depth, and attenuation as a function of frequency and depth are obtained from an analysis of the pressure time series generated by the explosive charges and received at the array.</p> <p>To find the velocity profile, the sediment is modeled as a horizontally layered, laterally homogeneous medium. A least squares solution is found for the velocity gradients in each layer of the model. Velocity as a function of depth is obtained by integrating these gradients. A second approach to inferring velocity structure utilizes linear programming. Errors in the data are easily incorporated into the problem using this formulation. The method takes upper and lower bounds on the input data and gives as a solution upper and lower bounds on the velocity profile. All velocity profiles that are consistent with the data lie within these bounds.</p> <p>A method of spectral ratios is used to estimate attenuation in the sediment as a function of frequency and depth. The sediment is again modeled as a layered medium, with each layer having a separate attenuation coefficient. Solving for each of the coefficients gives attenuation as a function of depth.</p>					
20. DISTRIBUTION / AVAILABILITY OF ABSTRACT <input type="checkbox"/> UNCLASSIFIED/UNLIMITED <input checked="" type="checkbox"/> SAME AS RPT. <input type="checkbox"/> DTIC USERS			21. ABSTRACT SECURITY CLASSIFICATION UNCLASSIFIED		
22a. NAME OF RESPONSIBLE INDIVIDUAL			22b. TELEPHONE (Include Area Code)	22c. OFFICE SYMBOL MET	

** MAY CONTAIN EXPORT CONTROL DATA **

ADAXXXXXX MICROFICHE ARE HOUSED IN THE GENERAL MICROFORMS RM

AN (1) AD-A193 235
 FB (2) 080300
 FG (2) 170100
 CI (3) (U)
 CA (5) SCRIPPS INSTITUTION OF OCEANOGRAPHY LA JOLLA CA MARINE
 PHYSICAL LAB
 TI (6) Velocity and Attenuation Profiles in the Monterey
 Deep-Sea Fan.
 TC (8) (U)
 DN (9) Doctoral thesis.
 AU (10) Brienza, Richard K.
 RD (11) Dec 1987
 PG (12) 103
 RS (14) MPL-U-67/87
 RS (14) SID-REF-87-28
 CT (15) N00014-80-C-0220
 RC (20) Unclassified report
 DE (23) *SEDIMENTS, *OCEAN BOTTOM SOILS, *ACOUSTIC DETECTION,
 ARRAYS, ATTENUATION, COEFFICIENTS, DEEP OCEANS,
 ESTIMATES, EXPLOSIVE CHARGES, GRADIENTS, HOMOGENEITY,
 HYDROPHONES, INPUT, LAYERS, LEAST SQUARES METHOD,
 LINEAR PROGRAMMING, MODELS, PRESSURE, PROFILES, RATIOS,
 SOLUTIONS(GENERAL), SPECTRA, THICKNESS, TIME SERIES
 ANALYSIS, VERTICAL ORIENTATION, ACOUSTIC VELOCITY,
 ACOUSTIC ATTENUATION, ACOUSTIC REFRACTION, ANGLE OF
 ARRIVAL.
 DC (24) (U)
 ID (25) Monterey Peninsula.
 IC (26) (U)
 AB (27) Data obtained during a refraction experiment is used to
 estimate velocity and attenuation profiles in an area
 of thick sediments (2.5 -3 km). A vertical hydrophone
 array was deployed at mid-depth in 2800 meters of
 water. Estimates of velocity as a function of depth,
 and attenuation as a function of frequency and depth
 are obtained from an analysis of the pressure time
 series generated by the explosive charges and received
 at the array. To find the velocity profile, the
 sediment is modeled as a horizontally layered,
 laterally homogeneous medium. A least squares solution
 is found for the velocity gradients in each layer of
 the model. Velocity as a function of depth is obtained
 by integrating these gradients. A second method to
 infer velocity structure using linear programming takes
 upper and lower bounds on the input data and gives as a
 solution upper and lower bounds on the velocity
 profile. All velocity profiles consistent with the data
 lie within these bounds. Using a similar sediment
 model, a method of spectral ratios estimates
 attenuation in the sediment as a function of frequency
 and depth. Solving for each of the coefficients gives
 attenuation as a function of depth.

** MAY CONTAIN EXPORT CONTROL DATA **

ADAXXXXXX MICROFICHE ARE HOUSED IN THE GENERAL MICROFORMS RM

AC (28) (U)
 DL (33) 01
 CC (35) 217400



LIBRARY
RESEARCH REPORTS DIVISION
NAVAL POSTGRADUATE SCHOOL
MONTEREY, CALIFORNIA 93940

MARINE PHYSICAL LABORATORY

SCRIPPS INSTITUTION OF OCEANOGRAPHY
//

San Diego, California 92152

Velocity and Attenuation Profiles in the Monterey Deep-Sea Fan

✓ Richard K. Brienzo

ae Scripps Institution of Oceanography.
SIO REFERENCE 87-28

MPL-U-67/87
December 1987

Approved for public release; distribution unlimited.

UNIVERSITY OF CALIFORNIA, SAN DIEGO
MARINE PHYSICAL LABORATORY
SCRIPPS INSTITUTION OF OCEANOGRAPHY
SAN DIEGO, CALIFORNIA 92152

**Velocity and Attenuation Profiles
in the Monterey Deep-Sea Fan**

*A dissertation submitted in partial satisfaction of the
requirements for the degree Doctor of Philosophy
in Electrical Engineering (Applied Ocean Science)*

Richard K. Brienzo

SIO REFERENCE 87-28

Sponsored by the
Office of Naval Research
Contract N00014-80-C-0220

MPL-U-67/87
December 1987



Table of Contents

	Page
Abstract	vii
1. Introduction	1
2. Data	3
2.1 Experiment	3
2.2 Time series	8
2.3 Spectra	12
3. Velocity Profile Estimation	19
3.1 Introduction	19
3.2 Velocity structure in the upper sediments	20
3.3 Converting array time series data to traveltimes	22
3.4 Re-parameterization of the data	31
3.5 Sources of error	36
3.6 Inverting the data	38
3.7 Forward modeling	49
3.8 Discussion	49
4. Attenuation Estimation	53
4.1 Introduction	53
4.2 Attenuation in marine sediments	53
4.3 Methods of estimating attenuation	58
4.4 Data	58
4.5 Results	70
4.6 Discussion	71
References	76
Appendix A1 Inverting $X(p)$, $T(p)$ and $\tau(p)$ data to obtain velocity as a function of depth	81
Appendix A2 The method of spectral ratios	89

List of Figures

	Page
Chapter 2.	
2.1 Refraction experiment on the Monterey Fan	4
2.2 The Monterey Deep Sea Fan	5
2.3 Location of the refraction experiment	6
2.4 Raypaths from shot to array	7
2.5 Array time series	
(a) Shot 15	9
(b) Shot 43	10
(c) Shot 25	11
2.6 Refracted paths as a function of range	13
2.7 Received time series as a function of range	14
2.8 Single channel time series	16
2.9 Spectra of the arrivals from Figure 2.8	17
2.10 Impulsive model of the shot spectrum	18
Chapter 3.	
3.1 Associating an arrival at the array with a raypath	23
3.2 Raypaths in the water column	26
3.3 Velocity profile in the water column	26
3.4 Removing the water path contribution	29
3.5 (a) $T(X)$ data (b) $T(p)$ data	34
(c) $X(p)$ data (d) $\tau(p)$ data	35
3.6 Inversion using a one layer model	40
3.7 Inversion using a two layer model	41
3.8 Inversion using a three layer model	42
3.9 Inversion using a four layer model	43
3.10 Inversion using a five layer model	44
3.11 90% confidence bounds for the 3 and 4 layer models	45
3.12 Input bounds on $\tau(p)$ and $X(p)$ data	47
3.13 Linear programming solution	48
3.14 Forward modeling	
(a) $T(X)$ data (b) $T(p)$ data	50
(c) $X(p)$ data (d) $\tau(p)$ data	51
Chapter 4.	
4.1a Spectral ratio data, Shot 41 BR	59
4.1b Spectral ratio data, Shot 17 BR	60
4.1c Spectral ratio data, Shot 29 S-BR-S	61
4.1d Spectral ratio data, Shot 44 S-BR-S	62
4.2a Attenuation profile: 3 layer model, 3 eigenvectors retained	65

4.2b	Attenuation profile: 4 layer model, 4 eigenvectors retained	66
4.2c	Attenuation profile: 7 layer model, 5 eigenvectors retained	67
4.2d	Attenuation profile: 13 layer model, 5 eigenvectors retained	68
4.2e	Attenuation profile: 13 layer model, 7 eigenvectors retained	69
4.3	Four layer attenuation model with 90% confidence bounds	70
4.4	Relationship between the velocity gradient and Q^{-1} as a function of depth	73
4.5	Attenuation as a function of frequency	74
4.6	Attenuation as a function of depth	75

Appendix A1

A1.1	Raypath through a laterally homogeneous, vertically inhomogeneous medium	88
A1.2	Constant gradient model	88

Appendix A2

A2.1	Plane wave propagating through an attenuating medium	94
A2.2	Ray propagating through a horizontally layered, attenuating medium	94

List of Tables

	Page
Chapter 3.	
3.1 Angle of arrival at the hydrophone array	24
3.2 Velocity profile in the water column	27
3.3 Shot locations	28
3.4 Sea floor depth	29
3.5 Arrival time differences between direct and refracted paths	31
3.6 X , T , and τ data	33
3.7 Velocity profile in the sediment for a three layer model	46
3.8 Velocity profile in the sediment for a four layer model	46
Chapter 4.	
4.1 Attenuation studies	56
4.2 Spectral ratio data	63
4.3 Solutions presented in Figure 4.2	64
4.4 Attenuation profile for a 4 layer model	71
4.5 Attenuation profile for a 7 layer model	71

ABSTRACT OF THE DISSERTATION

Velocity and Attenuation Profiles in the Monterey Deep-Sea Fan

by

Richard K. Brienzo

Doctor of Philosophy in Electrical Engineering (Applied Ocean Science)
University of California, San Diego, 1987
Professor William S. Hodgkiss, Chair

Data obtained during a refraction experiment is used to estimate velocity and attenuation profiles in an area of thick sediments (2.5 - 3 km) on the Monterey Deep-Sea Fan. A 20 element vertical hydrophone array was deployed at mid-depth in 2800 meters of water. Explosive sources, set for a depth of 1820 meters, were detonated at ranges between 3.5 km to 37 kilometers from the array. Estimates of velocity as a function of depth, and attenuation as a function of frequency and depth are obtained from an analysis of the pressure time series generated by the explosive charges and received at the array.

To find the velocity profile, the sediment is modeled as a horizontally layered, laterally homogeneous medium. A least squares solution is found for the velocity gradients in each layer of the model. Velocity as a function of depth is obtained by integrating these gradients. A second approach to inferring velocity structure utilizes linear programming. Errors in the data are easily incorporated into the problem using this formulation. The method takes upper and lower bounds on the input data and gives as a solution upper and lower bounds on the velocity profile. All velocity profiles that are consistent with the data lie within these bounds.

A method of spectral ratios is used to estimate attenuation in the sediment as a function of frequency and depth. The sediment is again modeled as a layered medium, with each layer having a separate attenuation coefficient. Solving for each of the coefficients gives attenuation as a function of depth.

1. Introduction

Both the water and bottom sediment act as transmission media for acoustic signals. Since there is a general increase in sound velocity with depth in the sediment, much of the acoustic energy that enters the sediment is refracted back into the water column. Knowing the velocity and attenuation of sound in the sediment is therefore important in modeling sound propagation in the ocean as well as providing information about sediment type and structure. In this report, propagation of low frequency sound in the sediments will be studied through the estimation of velocity and attenuation profiles in the sediment.

In April 1981, the Marine Physical Laboratory conducted a refraction experiment in an area of thick sediments (2.5-3 km) on the Monterey fan. The research vessel FLIP (FLoating Instrument Platform) was moored in 2800 meters of water and utilized as a receiving station. A 20 element vertical hydrophone array with equal sensor spacing and a total aperture of 475 meters (25 meter spacing between elements) was deployed at mid-depth in the water column. Explosive sources, set for a depth of 1820 meters, were detonated at ranges between 3.5 km to 37 km from FLIP.

Acoustic energy travels along numerous paths in going from the shot to the hydrophone array. Of interest in this study is acoustic energy which enters, propagates through the sediment, and is subsequently refracted back into the water column before being received at the array. Both velocity as a function of depth, and attenuation as a function of frequency and depth are obtained from an analysis of the pressure time series generated by the explosive charges and received at the array.

The report is organized as follows. Chapter 2 contains a description of the refraction experiment on the Monterey Fan. Examples of the array time series are given and individual arrivals in the time series are related to specific raypaths. The chapter concludes with a discussion of some of the characteristics of shot spectra.

In Chapter 3, the array time series are used to estimate velocity in the sediment as a function of depth. Two methods are used to obtain information about the velocity structure. The sediment is modeled as a horizontally layered, laterally homogeneous medium. A least squares solution is found for the velocity gradients in each layer of the model. Velocity as a function of depth is obtained by integrating these gradients. Inversion for the velocity profile by this method is discussed in the context of a general linear inverse problem in Appendix A1. A second approach to inferring velocity structure utilizes linear programming. Errors in the data are easily incorporated into the problem using this formulation. The method takes upper and lower bounds on the input data and gives as a solution upper and lower bounds on the velocity profile. All velocity profiles that are consistent with the data lie within these bounds.

A method of spectral ratios is used in Chapter 4 to estimate attenuation in the sediment as a function of frequency and depth. Spectral ratios are formed by dividing the spectrum of an arrival which travels through the

sediment by that of an arrival which travels only through the water column. A derivation in Appendix A2 shows that attenuation in the sediment is proportional to the slope of the spectral ratio. The sediment is again modeled as a layered medium, with each layer having a separate attenuation coefficient. Solving for each of the attenuation coefficients gives attenuation as a function of depth.

2. Data

2.1 Experiment

In April 1981, the Marine Physical Laboratory conducted a refraction experiment in an area of thick sediments (2.5-3 km) on the Monterey fan ($36^{\circ} 37.31'N$, $122^{\circ} 41.76'W$). The research vessel FLIP (FLoating Instrument Platform) was moored in 2800 meters of water and utilized as a receiving station (Figure 2.1). Figure 2.2 shows the general area of the experiment.

A 20 element vertical hydrophone array with equal sensor spacing and a total aperture of 475 meters (25 meter spacing between elements) was deployed at mid-depth in the water column. The hydrophones were numbered from 1 to 20, with number 1 being the bottom element. Hydrophone number 1 was located at 1912 meters, which placed the top element at 1437 meters, and the midpoint of the array at 1675 meters. Hydrophones 11 - 20 were set at a gain of approximately 40 dB higher than 1 - 10 to accommodate a wide dynamic range of signals. Hydrophones 1 and 4 were later found to have malfunctioned and are not used in the data analysis. The analog hydrophone outputs were lowpass filtered at 400 Hz, digitized at 1 kHz per channel and recorded on magnetic tape.

Explosive sources were launched over two separate seven hour periods at ranges from 3.5 km to 37 km from FLIP. Figure 2.3 indicates the tracks of the two shot runs. Both shallow (300' Mk 82 SUS) and deep (6000' Mk 94 SUS + 256# TNT) charges were utilized. Only the deep charges were used for the work presented in this report. In addition to generating more energy, they are far enough from bottom and surface reflecting layers so that reflected energy does not interfere with energy arriving along other paths of interest.

The position of the shooting ship was monitored from FLIP by radar. Water temperature data were collected using 1800 meter XBT's from the shooting ship during both shot runs. A total of 19 temperature profiles were collected over a period of two days.

The Monterey fan (Figure 2.2) has been the subject of many studies [27, 47, 48, 49, 67]. It is primarily fed by the Monterey and Ascension canyon systems. The sediments are mainly terrigenous, consisting of very fine sands in the valleys, and mostly silts and clays away from the valleys and channels. The sea floor in the area of this experiment is relatively flat (Figure 2.3). The depth was 2800 meters at FLIP, increased to a depth of 2930 meters at a range of 20.2 kilometers, and to 3230 meters depth at a range of 32.4 kilometers.

Figure 2.4 illustrates a few of the raypaths that sound may take in traveling from the shot to the array. Paths that interact with the bottom more than once will not be considered in this analysis. This figure also shows the coverage (sampling) of the sediment by each type of ray. Bottom interacting rays with a small angle of incidence (BR) graze the sediment while the steeper raypaths (S-BR-S) sample deeper portions of the sediment. The maximum depth in

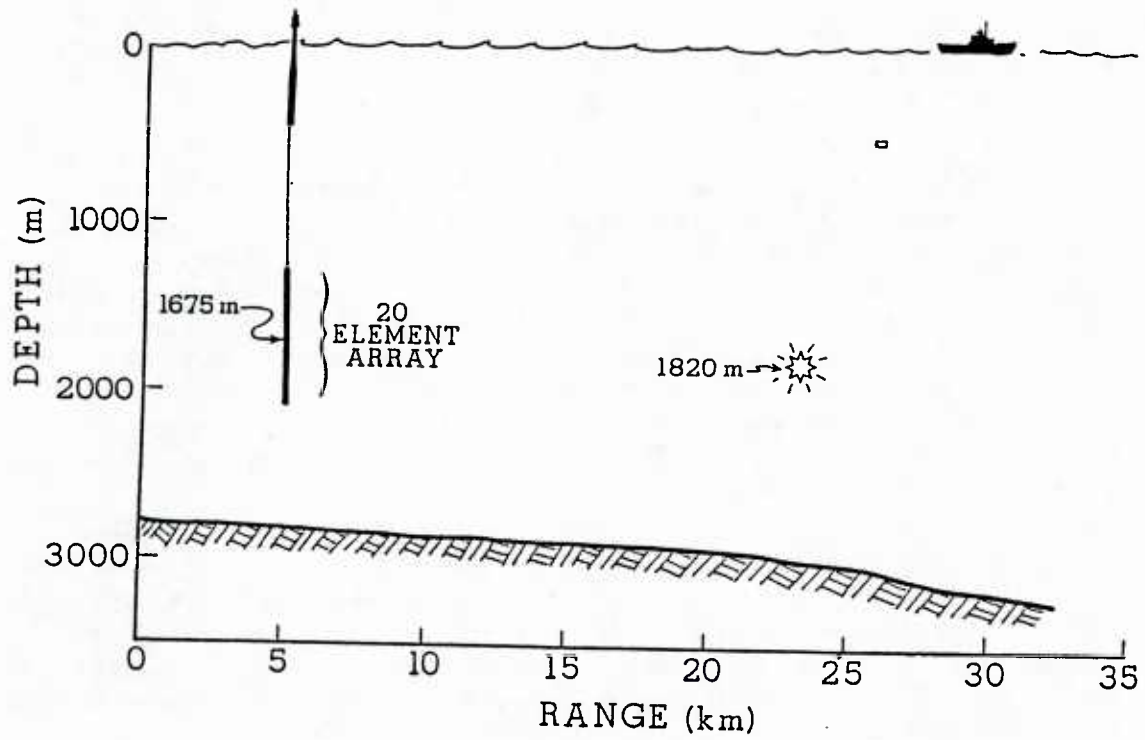


Figure 2.1 Refraction experiment on the Monterey Fan. A 20 element hydrophone array was deployed at mid-depth in 2800 meters of water. Explosive charges were detonated at ranges between 3.5 to 37 km from FLIP.

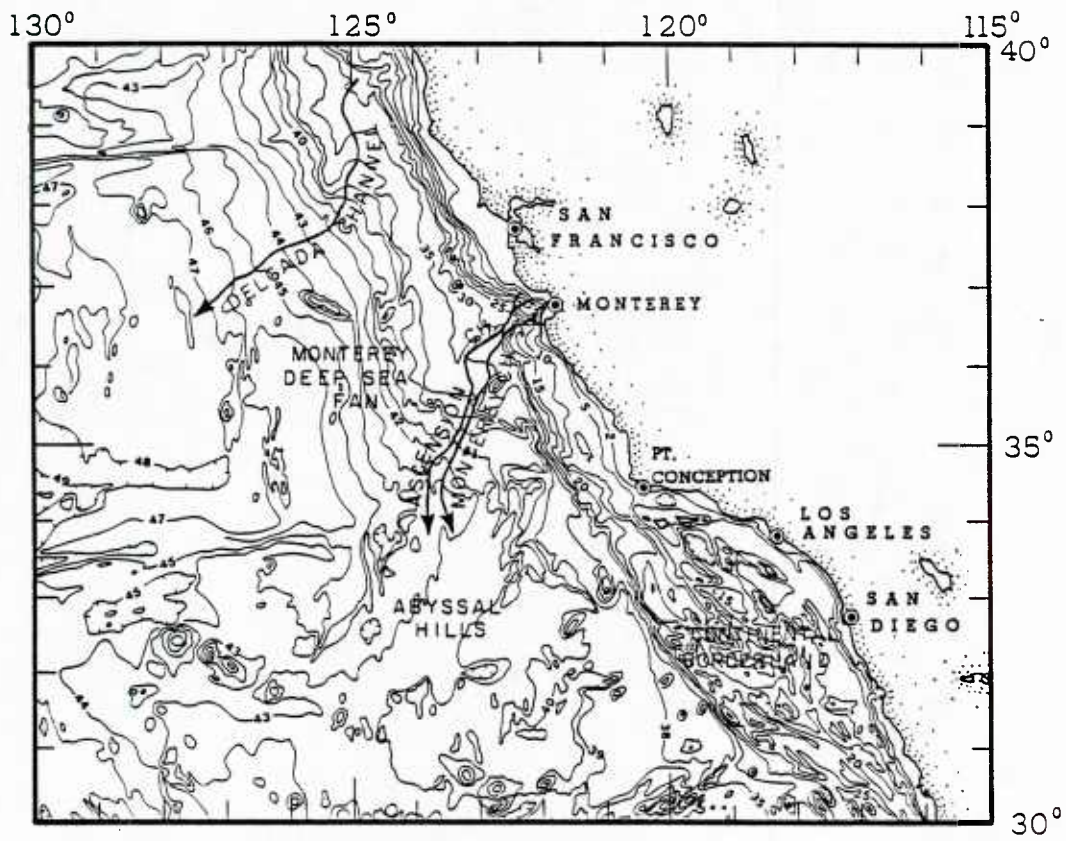


Figure 2.2 The Monterey Deep Sea Fan.
Depths are reported in meters $\times 10^{-2}$.

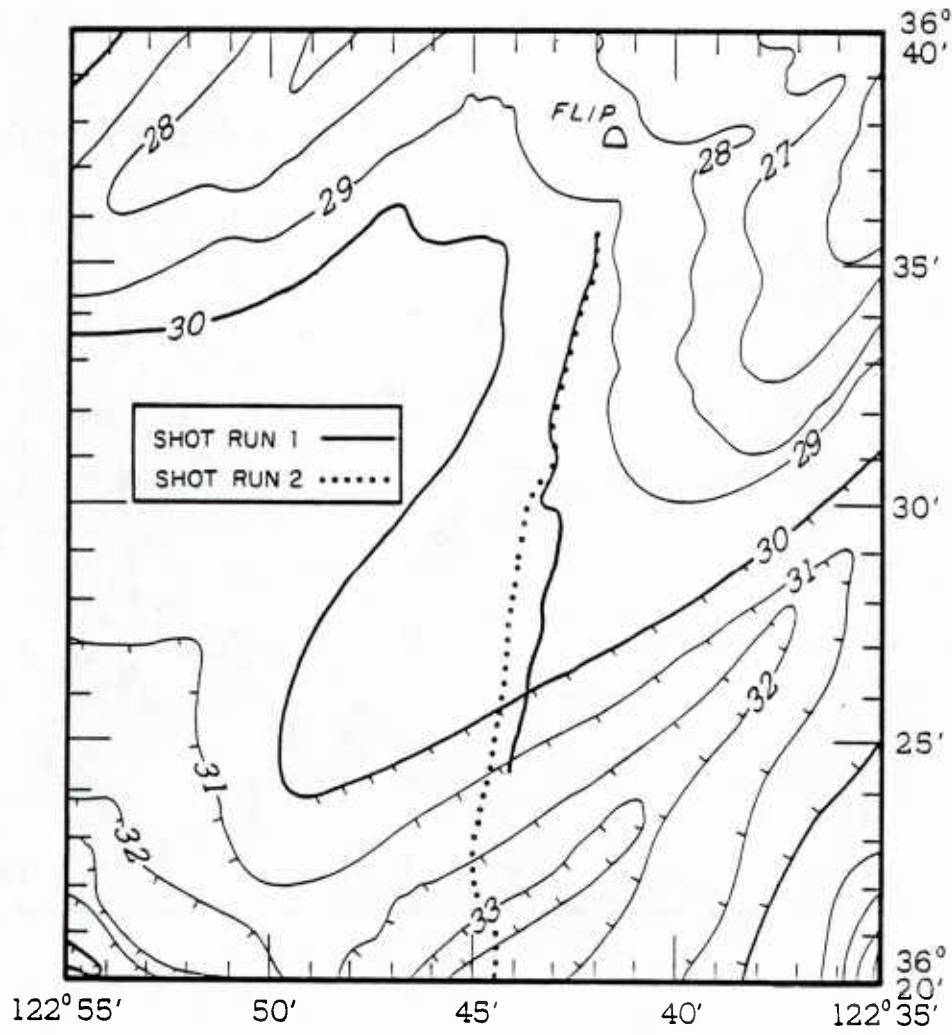


Figure 2.3 Location of the refraction experiment.
Depths are reported in meters $\times 10^{-2}$.

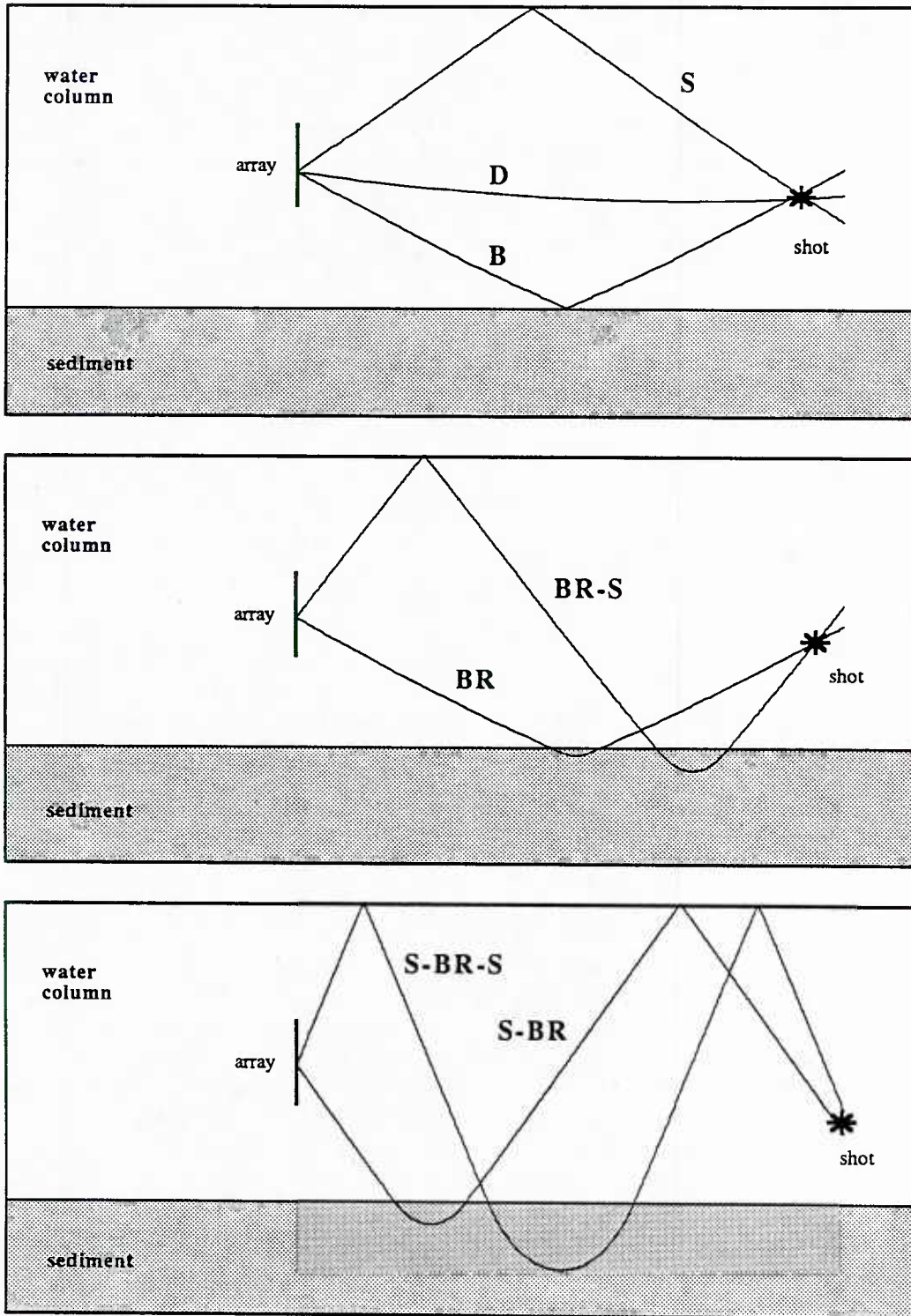


Figure 2.4 Raypaths from shot to array.

the sediment for which arrivals in this experiment are still discernible is about 625 meters.

Raypaths (see Figure 2.4)	
label	path
D	direct water path
S	surface reflection
B	bottom reflection
BR	bottom refraction
BR-S	bottom refraction - surface reflection
S-BR	surface reflection - bottom refraction
S-BR-S	surface reflection - bottom refraction - surface reflection

2.2 Time Series

Figures 2.5a, 2.5b, and 2.5c are examples of the type of data that were received at the hydrophone array. Each figure shows the output of hydrophones 11 - 20 for a single shot. The 2.048 seconds of data plotted here contains several distinct arrivals. Each of the arrivals represent acoustic energy that has traveled along a different path. The arrivals in these figures have been labeled to correspond to the raypaths in Figure 2.4. The method used to associate an arrival at the array with a raypath is described in Section 3.3.1.

The data presented in these three figures are from the high gain (upper) half of the array. The larger amplitude arrivals have saturated, and no inference should be made about the relative amplitudes of arrivals. These figures are meant to show angles at which the arrivals come into the array, and the time relationships between them. Acoustic energy coming from above the array arrives at the top hydrophone (20) first, and the line of arrivals appears to be slanted to the left (eg. shot 43, BR-S). Energy coming from the bottom arrives at the bottom element first, and the arrivals appear to be slanted to the right (eg. shot 43, S-BR). At short ranges, the arrivals are all separated in time. As the shot range increases, differences in the path lengths (hence differences in time between the arrivals) decrease, and the arrivals begin to run together.

Marine refraction experiments commonly have the source and/or receiver near the surface or bottom. This causes sediment refracted arrivals to be contaminated by reflections from these interfaces. Refraction experiments where the source is near the surface cannot be carried out in deep water since the simple raypaths refract completely in the water column and never enter the sediment. In the Monterey fan experiment both source and receiver were placed at mid-depth in relatively deep water. At short ranges (Fig. 2.5a), the arrivals are well separated in time. As the shot range increases, arrivals begin to run together (Fig. 2.5c). By 18 km, the bottom refraction (BR) disappears and the

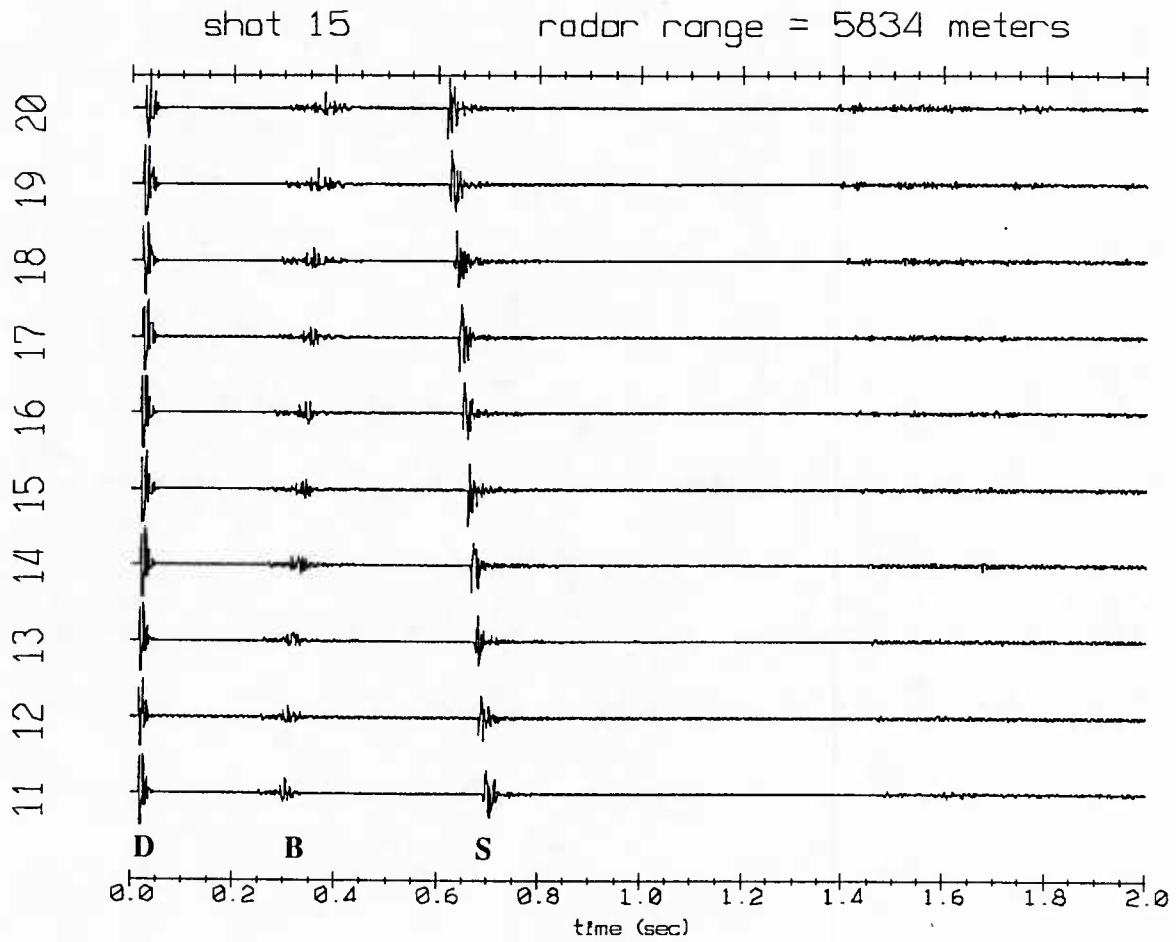


Figure 2.5a Array Time Series - Shot 15
Arrivals marked D, B and S correspond to the raypaths of Figure 2.4.

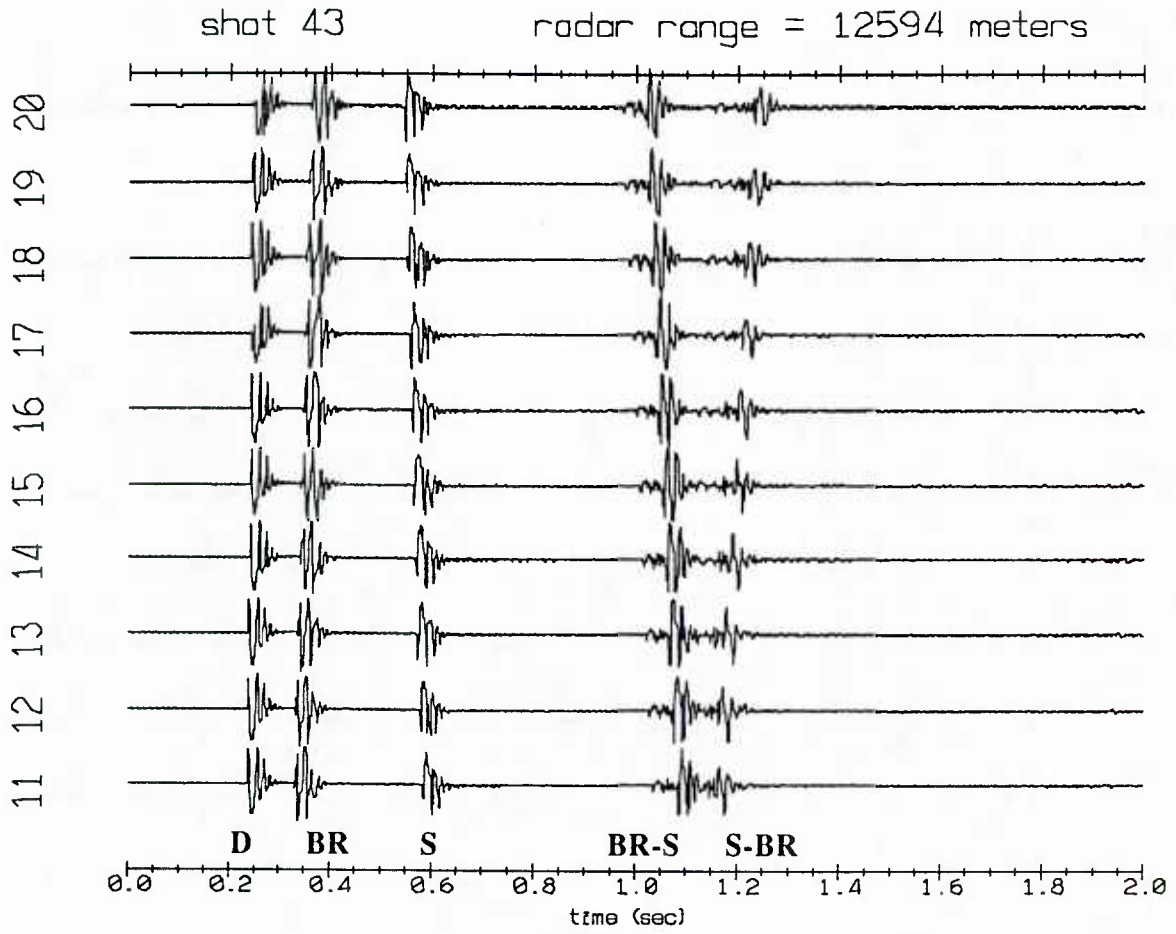


Figure 2.5b Array Time Series - Shot 43
Arrivals marked D, BR, S, BR-S and S-BR correspond to the raypaths of Figure 2.4.

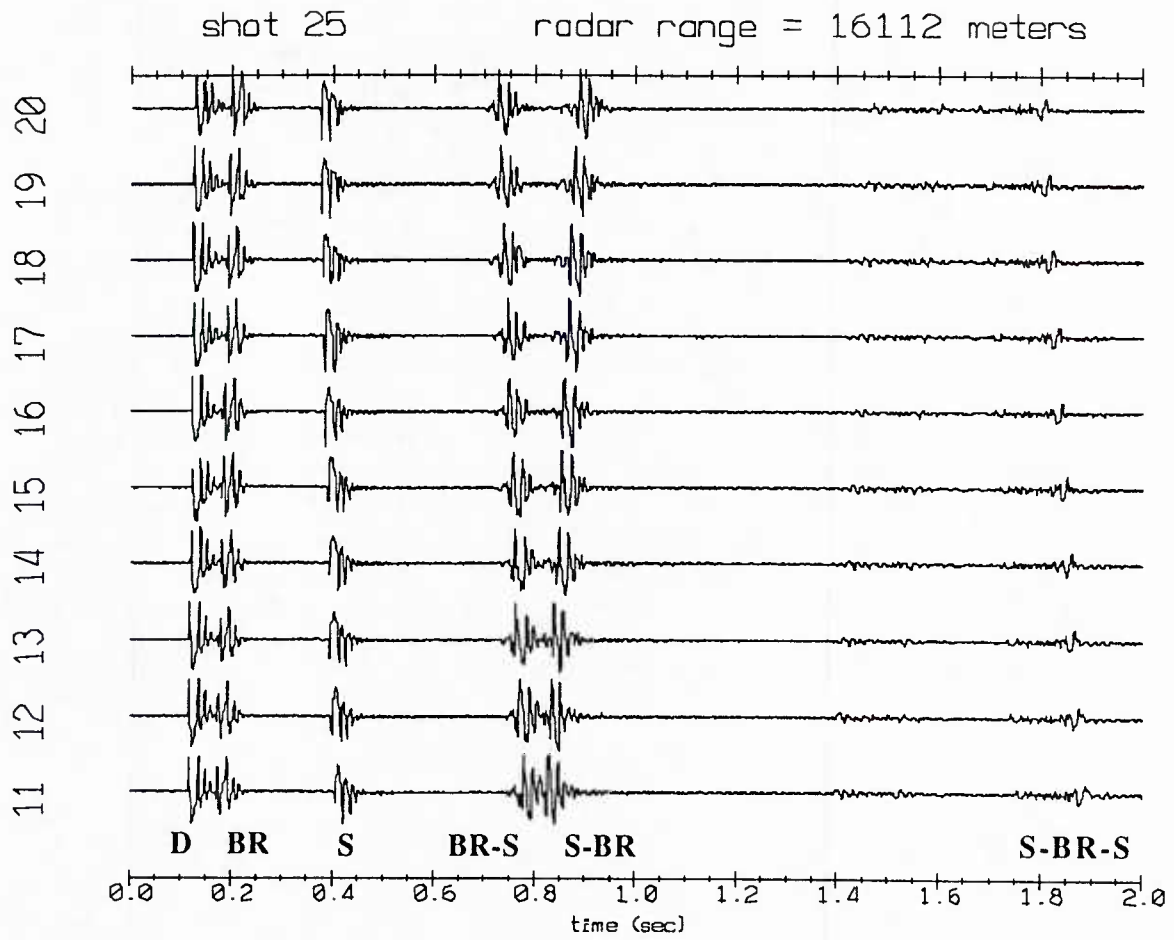


Figure 2.5c Array Time Series - Shot 25
 Arrivals marked D, BR, S, BR-S, S-BR and S-BR-S correspond to the raypaths of Figure 2.4.

ray refracts in the water column. The other sediment refracted arrivals (BR-S, S-BR, S-BR-S) exist and are separable out to about 25 km.

The time series in Figure 2.5 also indicate that bottom refracted energy does not appear at short ranges. When a wavefront encounters a change in acoustic impedance, part of the energy will be reflected and the remaining part transmitted. At short ranges, the angle of incidence at the array is large and the refracted energy penetrates deeply in the sediment. Rays with very deep turning points have long path lengths and are so highly attenuated that they do not appear in the time series. As the range increases, the angle of incidence at the array decreases, resulting in shallower turning points. The path length becomes shorter, decreasing the amount of attenuation, and refracted energy begins to appear. Figure 2.6 (reprinted from reference [7]) shows the rapid decrease in turning point depth with increasing range. Reflections off the sea floor lose much of their energy and appear as low amplitude, high frequency arrivals.

Figure 2.7 is a plot of the "stack", and illustrates some of the above features. Each time series in this figure is the output of a single channel (number 15) from a different shot. Again, note that the larger amplitude arrivals have saturated, so the time series presented here contain no information about relative amplitudes. The bottom time series is from a shot with a range of 5741 meters. There are only three distinct arrivals: a direct water path (D), a bottom reflection (B), and the surface reflection (S). By the time the range has increased to 7871 meters, a bottom refraction (BR) has emerged. At a range of 9075 meters, the first BR-S arrival is seen. Similarly, the S-BR-S arrival does not become apparent until a range of 16,112 meters. The deepest ray seen in this data has a turning depth of about 625 meters.

2.3 Spectra

Explosive sources generate energy over a wide range of frequencies. Upon detonation the explosive material is rapidly converted to a gas, and a shock wave with a very steep front is radiated into the water. If a pure impulse was generated, an explosive source would have a flat spectrum. This is not quite the case, however. As the gas bubble expands, internal pressure decreases, but because of inertia, the gas bubble overshoots its equilibrium radius. The pressure in the gas bubble goes slightly negative, and the bubble begins to contract. The gas bubble again overshoots its equilibrium radius, the pressure becomes positive and the bubble begins to expand again. The amplitude of these bubble pulses decays fairly quickly, and no more than four or five pulses are usually seen. The decaying, oscillatory nature of the resulting waveform produces a spectrum that is broadband, but not flat. Characteristics of the shot spectrum will be discussed below. Various relationships between the bubble pulse period, charge weight, shot depth, and other parameters may be found in [5, 38].

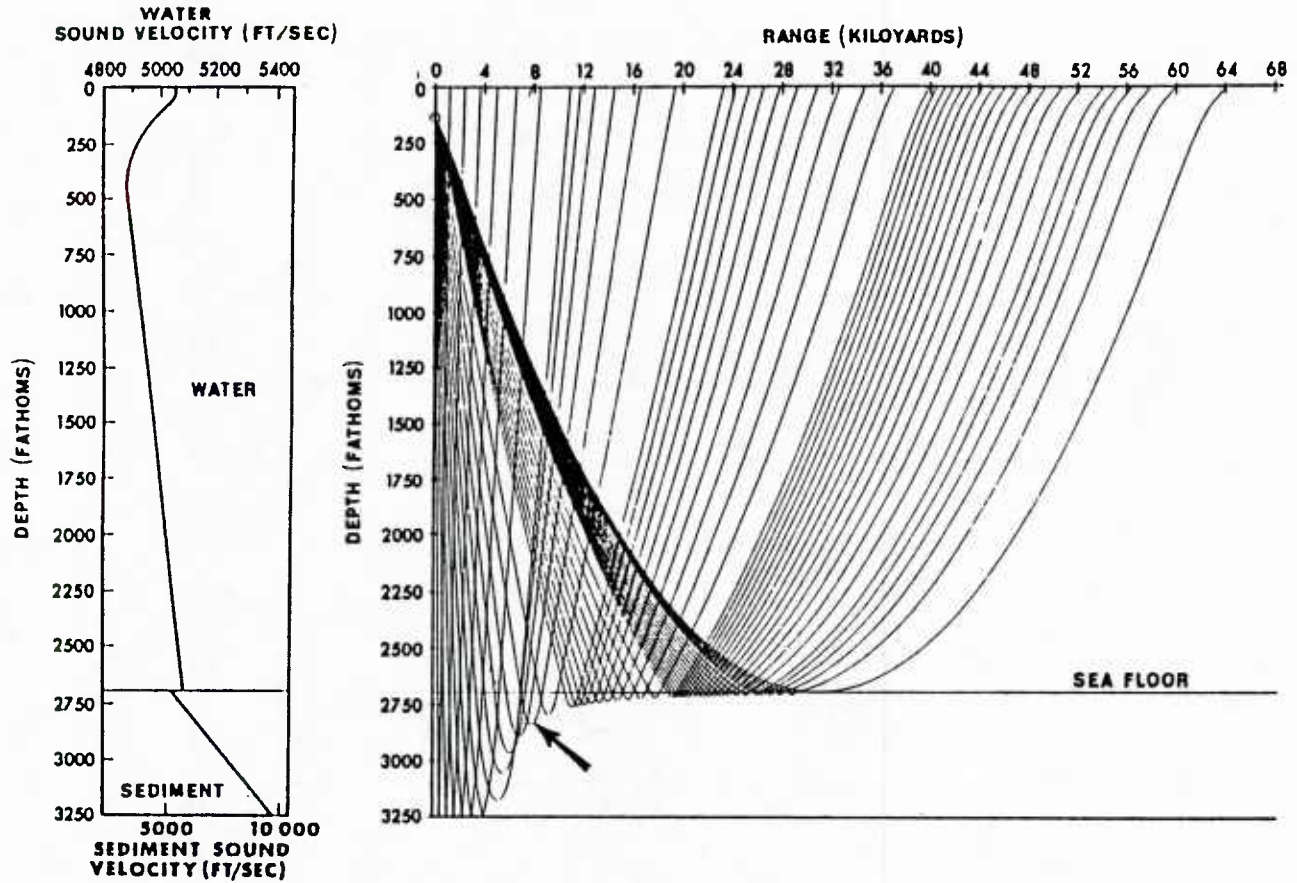


Figure 2.6 Refracted paths as a function of range
 As range increases, the depth of the turning point decreases. The arrow indicates the ray where refracted energy is first seen at the array. [Reprinted from Christensen, R.E., Frank, J.A., and Geddes, W.H., "Low frequency propagation via shallow refracted paths through deep ocean unconsolidated sediments", JASA, vol.57, No.6, 1421-1426, June 1975]

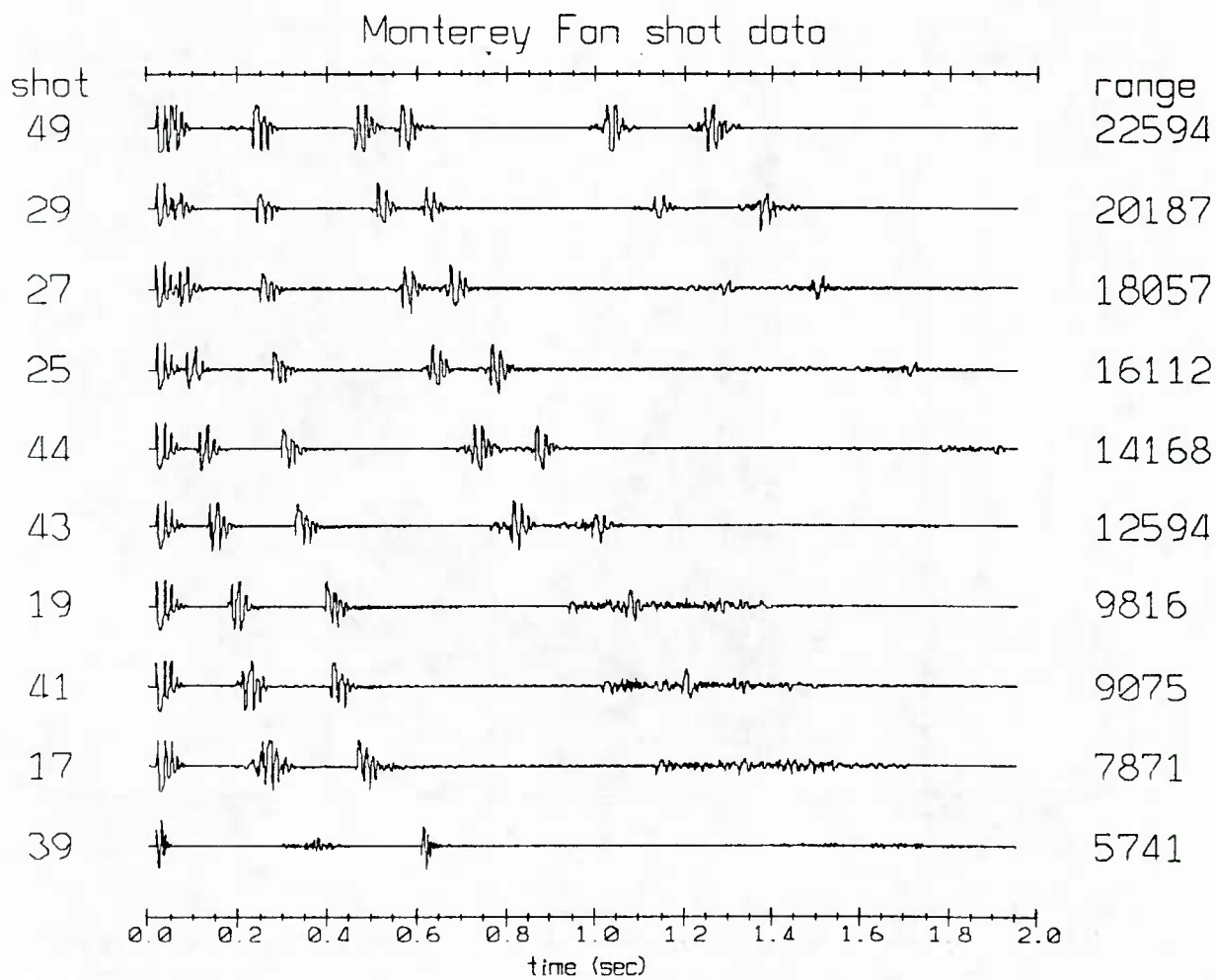


Figure 2.7 Received time series as a function of range
 Each time series is a single channel from a different shot. Shot range increases from bottom to top. Note that the ranges are not equally spaced.

Figure 2.8 shows the output of channel 3 from shot 41. Two refracted arrivals are present. There is a relatively large BR arrival, and a very deep and thus highly attenuated BR-S arrival. The individual arrivals plotted below are scaled to have the same maximum amplitudes. Spectra for these four arrivals are shown in the top of Figure 2.9. These were found by separating the individual arrivals of each type (D, BR, S, BR-S) from the eight good channels of the low gain half of the array. Discrete Fourier transforms of each type were calculated and incoherently averaged. The y-axis in these plots is $20 \log$ (magnitude). The time series was not calibrated, so in this case amplitudes represent sampled A-D levels. Calibration is not necessary since it is ratios of the various spectra that are of interest.

Spectra for the D, BR and BR-S paths are compared in the bottom plot of Figure 2.9. The direct path arrival (D) has a relatively broadband spectrum with somewhat regularly spaced peaks. When compared to the direct path spectrum, the bottom refracted (BR) spectrum appears to fall off more rapidly with increasing frequency, being nearly equal to the direct path spectrum at the bubble pulse frequency (50 Hz), and decreasing by about 8 dB at 350 Hz. The BR-S spectrum also shows an attenuation of the higher frequencies. This decrease with respect to the direct path spectrum will be exploited to find attenuation as a function of frequency and depth in Chapter Four.

A simple way to view the gross features of a shot spectrum is to consider the arrival as being a series of impulses. If it were an impulse train with a time spacing of T seconds, then its Fourier transform would be an impulse train with a frequency spacing of $1/T$. Although a shot arrival does not consist of a periodic impulse train - it is of finite length, has decreasing amplitude, and the bubble pulse period is not constant - there is a rough correspondence between the direct arrival's primary bubble pulse period of 20 msec, and a spacing of about 50 Hz in the peaks of its spectrum.

This is illustrated in Figure 2.10, where the direct path arrival is represented by four impulses with spacing and amplitude matching the peaks in the time series. The spectrum of this impulsive model along with the spectrum of the direct path arrival is plotted in Figure 2.10 (bottom). Although it is a simple model, its spectrum looks very similar to that of the actual arrival.

More complicated ways to model the shot spectrum have been devised. These models generally make the impulses look more like the real time series - for instance, putting increasing and decreasing exponentials on either side of the impulses. Modeling the shot spectrum is not a concern in this work. There is little attenuation of low frequency sound traveling short distances through the water column [36, 65 (pg. 106)], and the direct path arrival (D) is a good approximation of the source spectrum.

The array time series provides the basic data set. In Chapter Three, sediment refracted arrivals from this time series will be used to find velocity as a function of depth in the upper sediments. In Chapter Four, differences between the direct path (source) and sediment refracted spectra will be used to infer attenuation as a function of frequency and depth in the sediment.

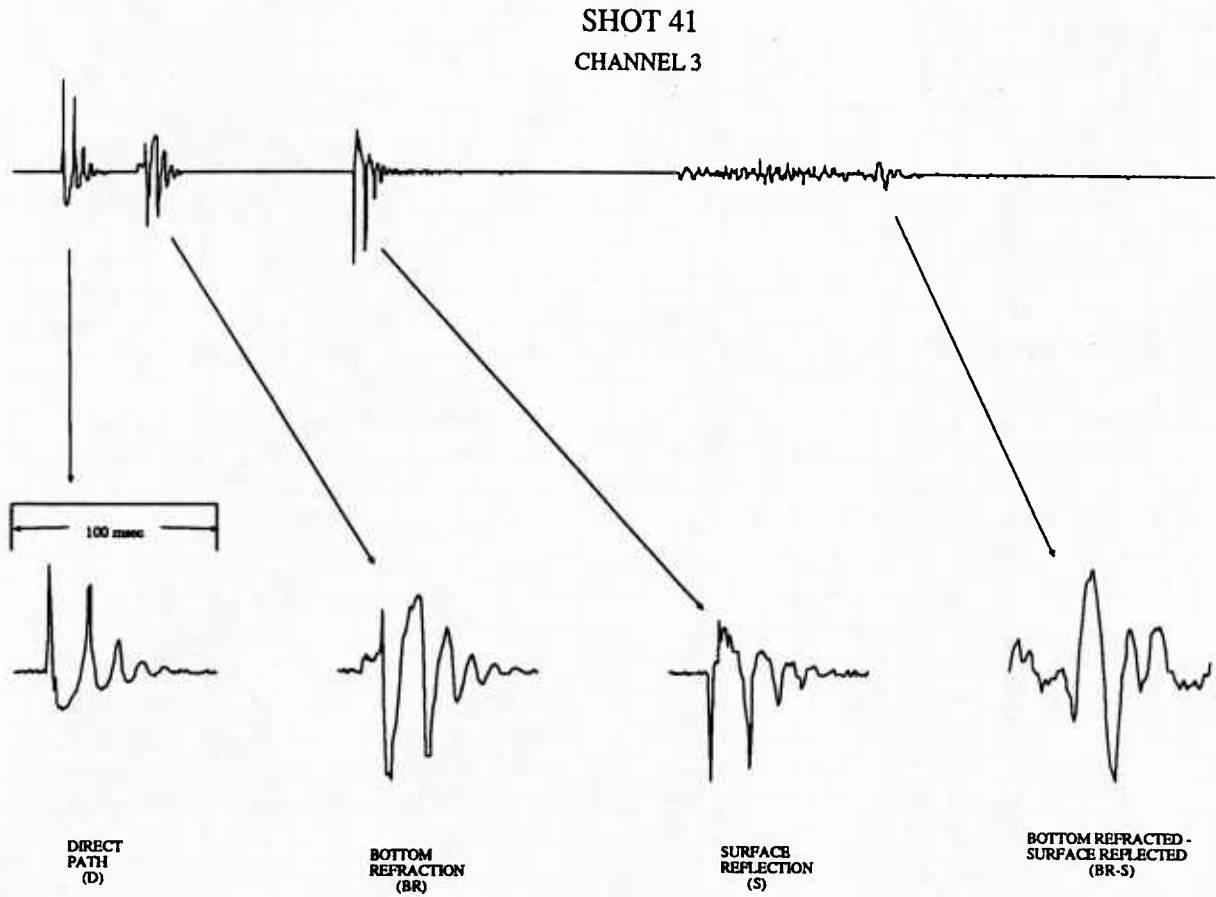


Figure 2.8 Single channel time series.
Individual arrivals plotted below are scaled to have the same maximum amplitude.

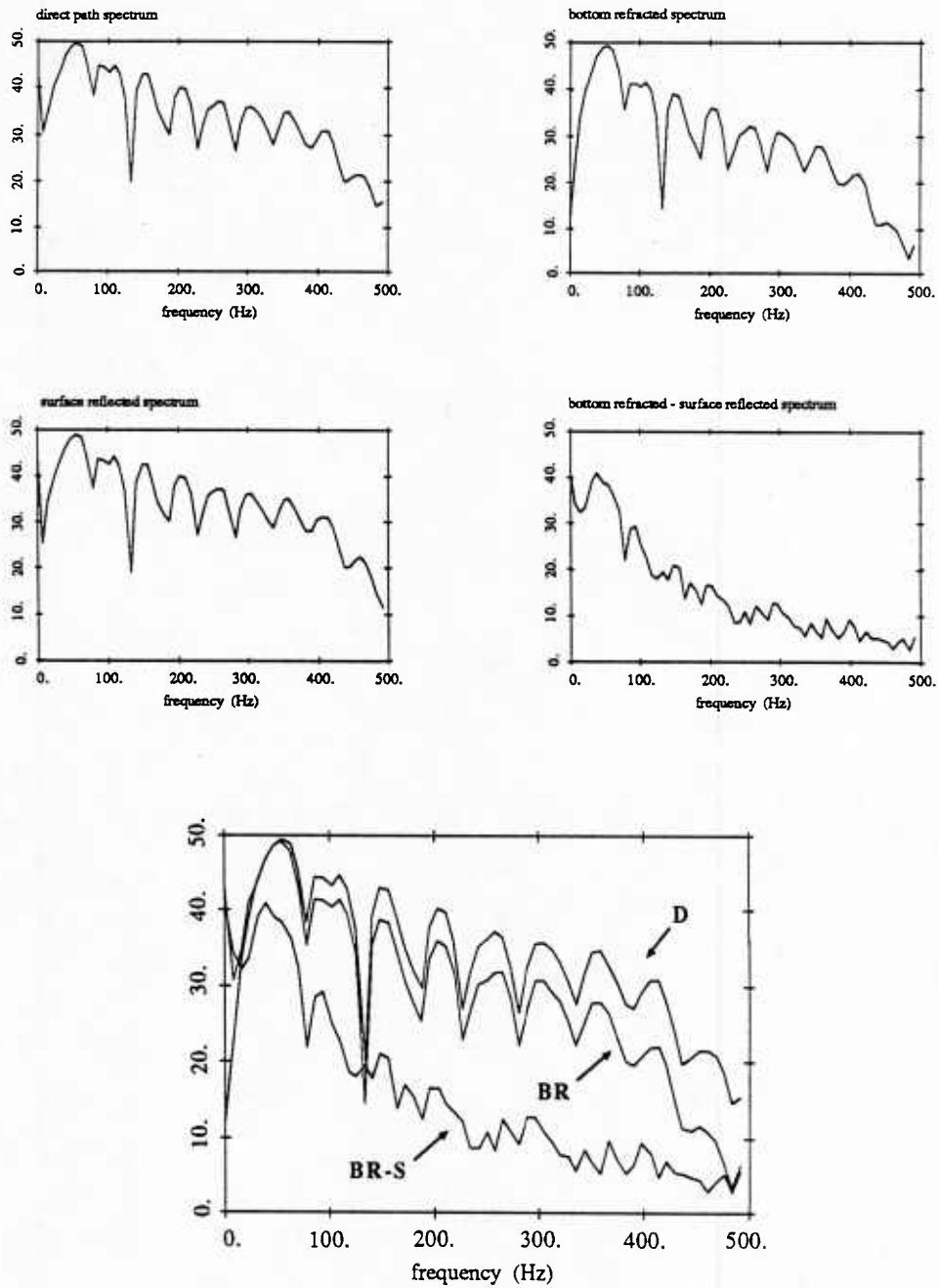


Figure 2.9 Spectra of the arrivals from Figure 2.8. y-axis is $20 \cdot \log(\text{magnitude})$

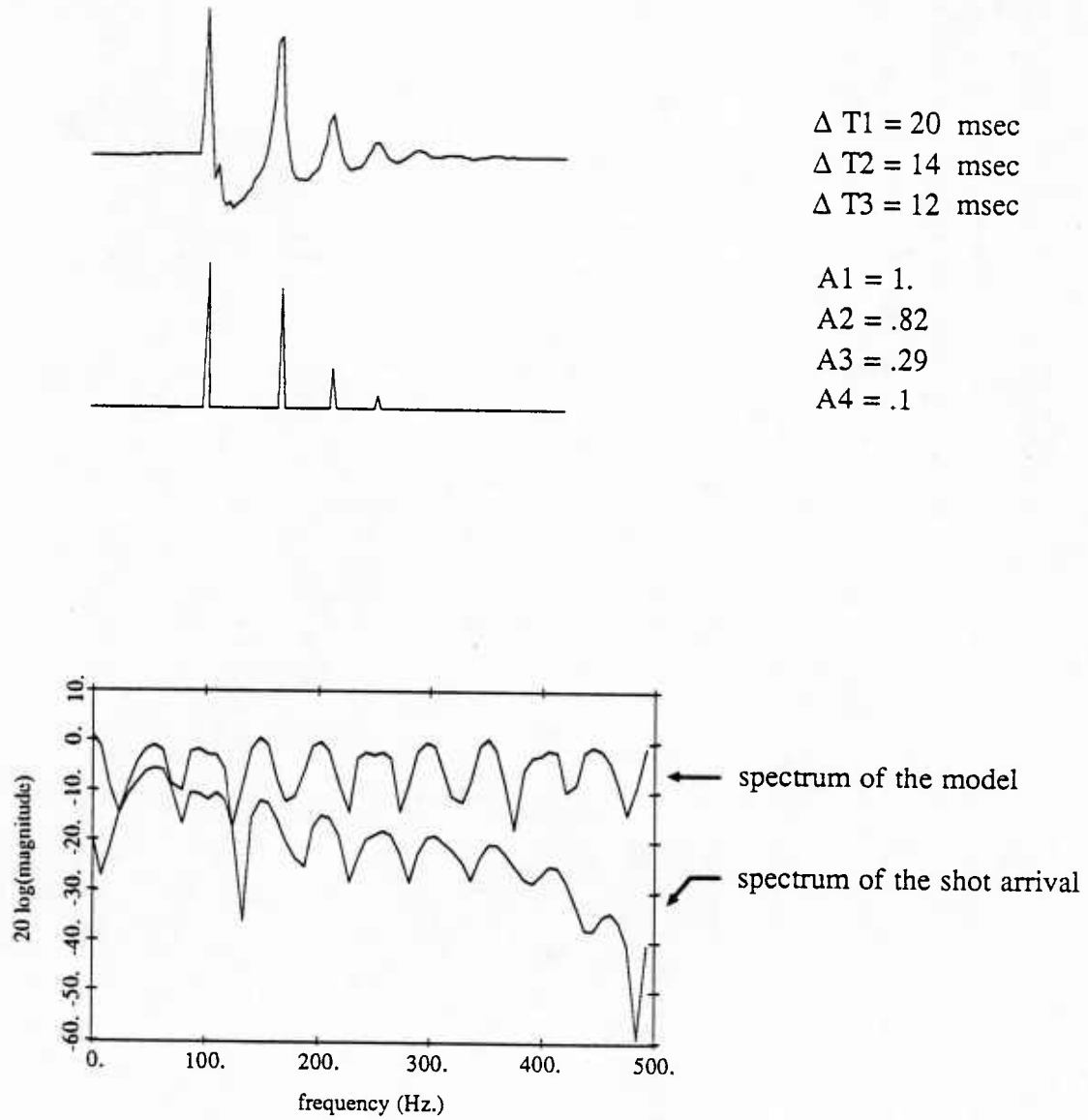


Figure 2.10 Impulsive model of the shot spectrum. Top figure is a direct path arrival (D). Middle figure is an impulsive model. Bottom figure shows the spectra of both. The spectrum of the model has been slightly offset to separate the two curves.

3. Velocity Profile Estimation

3.1 Introduction

In this chapter an estimate of the velocity profile in the upper sediment (to about 625 meters depth) is found. Since much of the acoustic energy entering the sea floor is refracted back into the water column, the velocity profile is important for modeling sound propagation in the ocean. An accurate velocity profile will also be required in Chapter Four for use in estimating attenuation as a function of depth in the sediment.

An overview of what is known about the velocity structure in the upper sediments is first presented. Next, steps taken to convert the received time series at the hydrophone array into sediment traveltimes (horizontal range in the sediment as a function of time) are described. This procedure involves several steps. A raypath must first be associated with each arrival at the array. Shot range and depth, and depth of the sea floor must be estimated. Finally, the range and time spent by the ray in the water column must be subtracted from the total range and time, yielding range and time of the ray in the sediment. This set of ranges and times form the traveltime data, giving time as a function of range $T(X)$. After re-parameterizing the data into functions of ray parameter p , they are then inverted to yield velocity as a function of depth.

Two methods are used to obtain information about velocity as a function of depth. A least squares solution will be used to find velocity gradients in a layered model. A velocity profile is obtained from these gradients. A second approach will pose the problem as a linear programming problem. Errors in the data are easily incorporated into the problem using this formulation. This method takes upper and lower bounds on the input data and gives as a solution, upper and lower bounds on the velocity profile. All velocity profiles that are consistent with the data lie within these bounds.

Placing meaningful bounds on the solution is important in interpreting the result. The least squares solution provides an answer; it gives a velocity profile which can then be used for modeling sound propagation. Because of finiteness of the data set, and errors, there are an infinite number of models which fit the data. Unless a statement regarding the quality of the result can be made, all that can be said is that the solution fits the data while minimizing a particular error criterion (the l_2 norm). Although rather pessimistic bounds are produced by the linear programming method, all models that are consistent with the data lie within these bounds. These bounds may be used to indicate the reliability of the least squares solution and show what can be inferred about the velocity structure from a finite data set containing errors. Using these two different approaches will provide a clearer interpretation of the results.

3.2 Velocity structure in the upper sediments

Hamilton, in a series of papers [16, 21, 22, 24, 25, 26], has summarized much of what is known about the velocity structure in sediments. In general, the velocity of sound in sediments increases with increasing depth. Velocity gradients are usually highest near the surface, decrease with depth, and approach a constant by about 700 meters. Mean values for velocity gradients for all sediments vary from 1.28 sec^{-1} at the surface to $.6 \text{ sec}^{-1}$ below 700 meters.

3.2.1 Causes of velocity gradients

Reduction of porosity

The most important factor is a reduction of porosity with increasing depth in the sediment. Porosity is the volume of water-filled pore space per volume of sediment. The amount of pore space in sediment is related to the size, shape, distribution, mineralogy and packing of the solid grains. In general, porosity increases as grain size decreases. As small particles, such as silts and clays fall and touch each other, they are loosely held together by interparticle forces and form a three-dimensional "cardhouse" structure. These sediments (for example, turbidites, clays and silts) near the surface are highly porous, typically 85%. Sands, which are larger and heavier, have porosities between 35 to 50%. As overburden pressure increases (with increasing depth), sediment particles are forced closer together, decreasing the porosity. As the number of interparticle contacts increase, sliding friction between particles increases. This causes an increase in rigidity, which leads to an increase in velocity. Porosity reduction accounts for about 66% of the total gradient.

Increase in temperature

An increase in temperature with depth is caused by heat flow through the sediment from the earth's crust and mantle. Hamilton [22] cites a change of about 25°C as depth in the sediment increases from 0 to 500 meters. Sound velocities vary with temperature in sediments about the same way as they do in sea water; the velocity of sound increases with increasing temperature. This accounts for about 17% of the total gradient.

Increases in mineral frame rigidity due to lithification

As sediment particles are forced together under increasing pressure, they come into closer contact. This aids in cementation of the particles (lithification) and increases the rigidity of the mineral frame, which increases the velocity. At depths below about 300–600 meters the sediment is semilithified or lithified and is called a mudstone or claystone. After lithification there is little decrease in porosity with increasing depth. Lithification is responsible for about 15% of the average gradient.

It should be noted that there is not a smooth transition between unlithified and lithified sediments. For example, calcareous sediments easily lithify into relatively high velocity chalk and limestone. These may appear at shallow depths (150–300 meters), but they are often interbedded with soft lower velocity unlithified sediments. This can cause scatter around the velocity-depth function.

For terrigenous sediments, the average linear velocity gradient between the surface and 500 meters depth is about 1 sec^{-1} . Gradients may be significantly lower in areas where sediments are rapidly deposited than in regions farther from the source. For example, Hamilton [22, pg. 920] reports a gradient of .86 near the source of the Bengal Fan, and a value of 1.87 farther to the South. When sediments accumulate in thick sections the porosity does not have time to be fully reduced under overburden pressure. Since $2/3$ of the average velocity gradient in silt-clays and turbidites is caused by a decrease of porosity with increasing depth, areas where the sedimentation rate is high have the smallest velocity gradients. Hamilton [24, pg. 1354] reports upper sediments (0–100 meters) for 5 shelf basins to have gradients between .3 to $.9 \text{ sec}^{-1}$, with an average gradient of $.7 \text{ sec}^{-1}$.

3.2.2 Velocity anisotropy

Media having velocities parallel to layers that are different from velocities perpendicular to layers are called anisotropic. If the cardhouse structure were to collapse (under sufficient pressure) to form a parallel-oriented section, velocity anisotropy may be induced. Hamilton claims there should be little anisotropy from this effect to about 200 meters, and a 5 to 10% increase in velocity parallel to the sea floor at 400 to 600 meters depth [16, pg. 4442-4443]. Another cause of anisotropy that may be more significant in regions of high deposition (such as deep-sea fans), is alternating parallel layers of different materials.

3.2.3 Velocity at the water-sediment interface

Several authors have indicated that the velocity in the upper layer of some sediments is slightly lower than that in the water column. Hamilton reports a ratio of sediment to bottom water velocity of .984 for pelagic clay and a value of .993 for turbidites [22, pg. 920]. The turbidite samples included silts and clays.

The velocity ratio at $36^{\circ} 31' \text{ N}$, $123^{\circ} 17' \text{ W}$ [12] was reported to be .988. This is very close to the site of the Monterey fan refraction experiment (which was at $36^{\circ} 37.31' \text{ N}$, $122^{\circ} 41.76' \text{ W}$) and the value of .988 will be used in the subsequent analysis. The mean depth of the sea floor will be taken to be 2853 meters. The velocity of sound in the water at 2853 meters is 1502.8 meters/sec, so the velocity of sound in the upper layer of sediment (interface) is

$$(1502.8 \text{ meters/second}) \times .988 = 1484.8 \text{ meters/second.}$$

Velocities in the water column are based on results contained in Section 3.3.2.

3.3 Converting array time series data to traveltimes

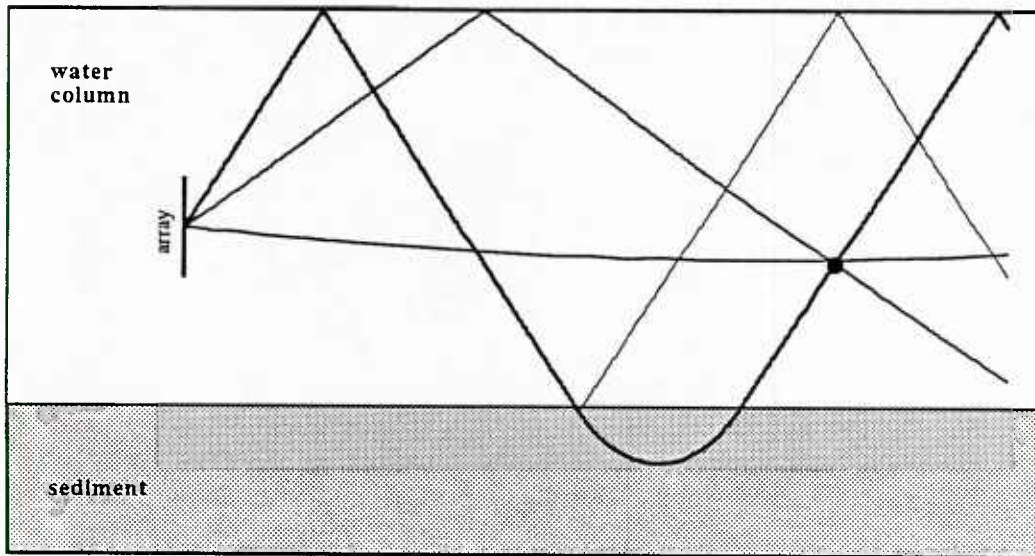
3.3.1 Identifying the arrivals

Examples of the data that were received at the hydrophone array were given in Figures 2.5a, 2.5b and 2.5c. Each of the arrivals represent acoustic energy that has traveled along a different path. Figure 2.4 illustrates a few of the paths that sound may take in traveling from the shot to the array. In order to utilize these data, it is necessary to identify the raypath associated with each arrival on the array time series.

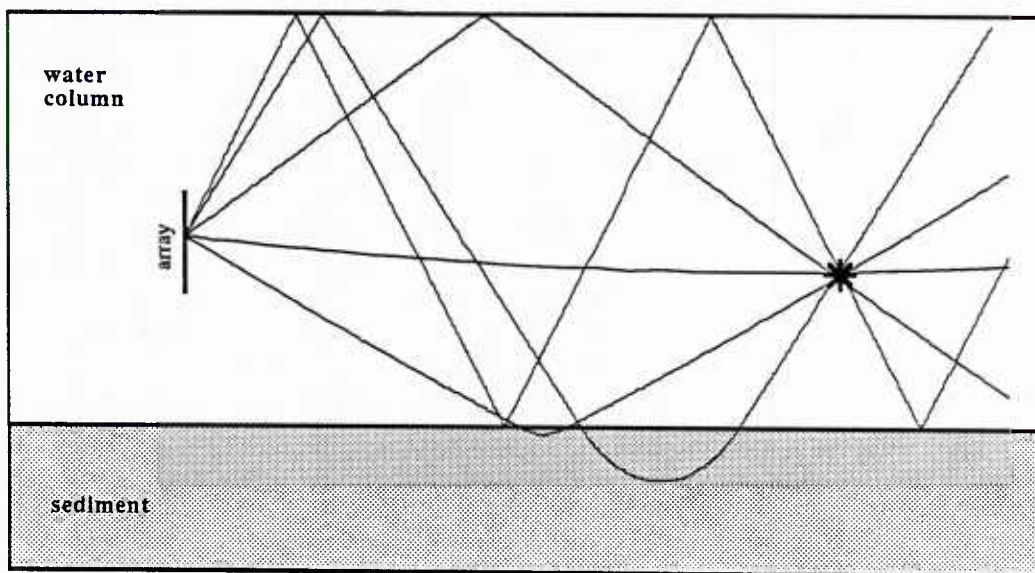
To associate an arrival with a raypath, time domain beamforming is used to estimate the angle of arrival for each arrival at the array. Once this is known, a ray leaving the array at its angle of arrival may be traced. A velocity profile for the water column was derived from XBT data (to 1800 meters) taken during the experiment. Archival data was used to extend this profile from 1800 meters to the sea floor. By appending a model sedimentary velocity profile [24] to the velocity profile of the water column, bottom interacting rays may be traced as both bottom reflections and bottom refractions. This is illustrated in Figure 3.1a. Here it is assumed that the intersection of the direct path (D) and surface reflection (S) gives the approximate location of the shot. The ray that is traced as a bottom reflection (B) misses the shot point by a wide margin while the ray traced as a bottom refraction - surface reflection (BR-S) comes very close. The conclusion is that this particular arrival refracted in the sediment and was reflected by the surface before reaching the array. Figure 3.1b shows all of the raypaths associated with arrivals at the array for this shot. It should be mentioned at this point that the true velocity profile in the sediment is unknown - it is what we are after. If all of the raytraces of bottom interacting arrivals had come as close as shown in Figure 3.1b, then the model velocity profile used for the raytracing would be an excellent estimate and there would have been no need to continue. This shot was particularly good and was chosen to illustrate the procedure for identifying the arrivals. Although most of the other shots were less ideal, there was enough of a difference in the raypaths to clearly identify the paths they had taken. Angles for all arrivals are given in Table 3.1. Angles are measured from the horizontal; arrivals coming from below the array have positive angles, those coming from above have negative angles.

3.3.2 Shot locations

A constant gradient raytrace program was used to estimate shot locations. Rays were traced from the array at the angle of arrival for the direct water path (D) until range along the ray matched the radar range recorded when the charge was launched. The depth at this range is assumed to be the shot depth. Times to that range and depth were also obtained from the raytrace.



(a)



(b)

Figure 3.1 Associating an arrival at the array with a raypath.

(a) A ray leaving the array at its angle of arrival is traced as both a bottom reflection and as a bottom refraction. The reflection misses the shot point (assumed to be the intersection of the direct and surface reflected paths) while the refraction comes very close. The conclusion is that this particular arrival refracted in the sediment and was reflected by the surface before reaching the array. (b) All raypaths for a medium-range shot.

Angle of Arrival							
Shot	Radar Range (meters)	D	BR	S	BR-S	S-BR	S-BR-S
38	3704	4.089	34.166*	-42.647	-56.923*	58.844*	-
13	3778	1.022	34.786*	-40.822	-57.871*	58.517*	-
39	5741	3.407	29.751	-30.934	-44.527*	-	-
15	5834	3.919	29.164	-31.532	-44.289*	-	-
40	7408	2.900	21.620	-24.769	-37.958*	-	-
17	7871	2.900	19.981	-23.278	-36.250*	37.742*	-51.670*
41	9075	2.896	17.286	-20.526	-42.416	-	-45.979*
19	9816	3.066	16.219	-19.258	-37.527	35.410	-43.580*
37	11575	3.066	13.949	-16.601	-28.387	31.731	-40.822*
21	11631	3.237	13.576	-16.397	-28.194	29.359	-
43	12594	3.407	13.052	-15.511	-27.424	29.751	-44.527
23	13890	3.237	12.179	-13.401	-24.582	26.089	-39.706
36	14075	3.407	11.483	-13.576	-23.835	25.333	-38.391
44	14168	3.578	11.657	-13.752	-24.022	25.711	-38.391
45	15742	3.919	10.963	-12.353	-21.987	23.278	-31.133
25	16112	4.089	10.789	-11.831	-20.890	22.539	-32.536
46	16946	4.260	10.443	-11.483	-20.526	21.255	-31.332
27	18057	4.602	**	-10.270	-18.538	19.439	-28.775
47	18520	4.943	**	-10.616	-18.538	19.078	-29.359
29	20187	5.456	**	-9.233	-16.574	17.822	-26.089
48	20650	5.542	**	-9.406	-16.752	17.464	-26.469
31	22039	5.798	**	-8.544	-15.511	16.574	-24.208
49	22594	6.141	**	-8.716	-15.688	16.042	-24.208
33	23706	6.483	**	-7.684	-14.806	15.865	-22.908
50	24817	7.000	**	-8.028	-14.454	14.982	-22.723
51	26576	7.513	**	-7.684	-14.102	13.567	-21.072
52	28613	7.856	**	-7.341	-13.401	12.179	-19.439
53	30002	8.028	**	-6.655	-12.702	11.310	-18.001
54	32410	8.028	**	-6.141	-12.528	10.616	-16.930
55	34355	-	**	-5.970	-12.005	10.443	-16.042
56	36299	-	**	-5.627	-12.353	9.751	-15.865

* indicates the bottom interaction was a reflection (not a refraction)

** indicates path does not exist

Table 3.1 Angle of arrival at the hydrophone array. Angles are measured from the horizontal; arrivals coming from below the array have positive angles, those coming from above have negative angles.

Initially, a water column velocity profile derived from 1800 meter XBT data taken during the experiment, and archival data below 1800 meters was used to trace the rays. It soon became evident that this profile was inadequate. Many of the rays ended up far from the assumed shot depth of 1820 meters. At short ranges, rays refracted too much. As shot range increased, rays tended to refract too little, giving greater shot depths with increasing range. The steps involved in finding velocity and attenuation profiles in the sediment critically depend upon having an accurate velocity profile in the water column. When using the direct water arrival to locate the shot, the ray is nearly horizontal and is very sensitive to gradients in the water column. A slight increase or decrease in bending of the ray translates to a large decrease or increase in the final range. An accurate velocity profile in the water column is also needed when finding sediment traveltimes. To determine the range and time that a ray spends in the sediment, the range and time that the ray spends in the water column must be subtracted out. Sediment refracted arrivals that are received at the array spend a much larger amount of their time in the water column than in the sediment. The water path contribution is such a large portion of the total traveltime, that even small errors in removing the water path may be of the same order as the traveltime in the sediment.

In order to come up with a better estimate, the direct water path data were inverted to find a velocity profile in the lower portion of the water column (from the array at 1500 meters, to the sea floor). As the shot range increases, the direct path rays refract deeper as shown in Figure 3.2. The data set provided by these arrivals is of the same form as that which is used to find the velocity profile in the sediment (i.e. $T(X)$ or one of its parameterizations, $X(p)$, $T(p)$, or $\tau(p)$). Inversion of the data is a straight-forward problem since the velocity profile in this part of the water column increases monotonically to the floor. The least squares method used to invert the data is described in detail in Sections 3.4 and 3.6.1, and in Appendix A1.

XBT data must be used to obtain a velocity profile in the upper portion of the water column (from the surface to the array). When looking up from the array toward the surface, the sound channel provides a low velocity zone which makes an inversion of surface reflected data a difficult problem. Since there is much scatter in the XBT data, the accuracy of the velocity profile in the upper water column is likely to be poor. Also, since the experiment was carried out over a two day period with shot runs being conducted between noon and midnight, the velocity profile in the upper part of the water column varied as a function of time. At best, only an average velocity profile for this region could be obtained.

Although a few shots still missed the nominal depth of 1820 meters by a large margin, overall the results were improved using the velocity profile obtained from the above method. The sound speed profile in the water column used to reduce the data is listed in Table 3.2 and illustrated in Figure 3.3. Shot locations are given in Table 3.3.

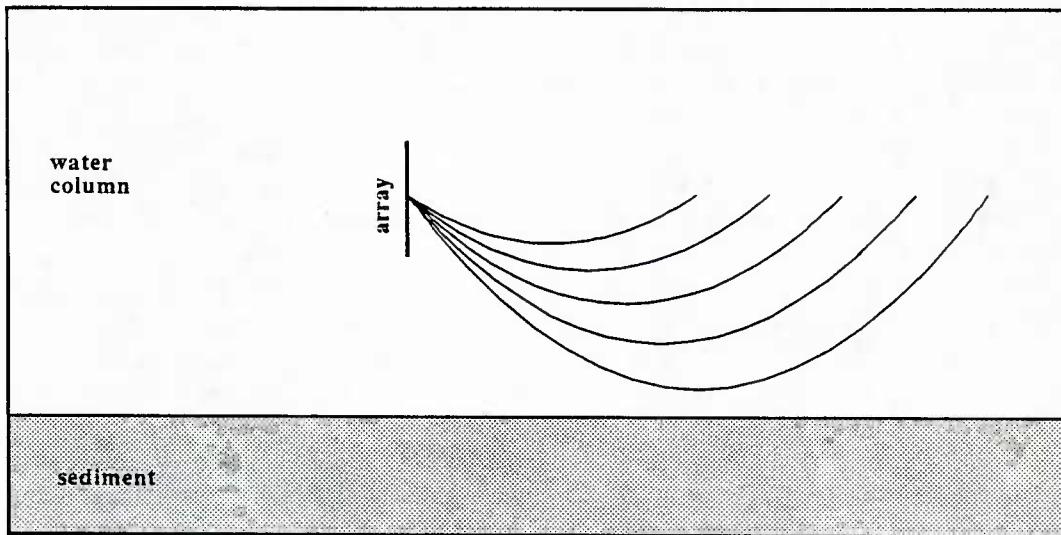


Figure 3.2 Raypaths in the water column. Direct paths sample deeper parts of the water column as shot range increases. The data set provided by these arrivals can be used to obtain the velocity profile in the lower portion of the water column.

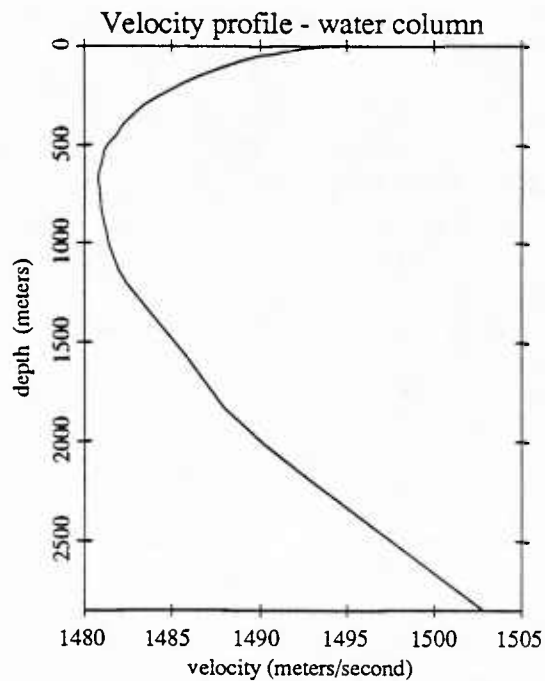


Figure 3.3 Velocity profile in the water column. Lower portion of the velocity profile was obtained from inversion of direct water path data (illustrated in Figure 3.2). Upper portion of the profile was obtained from XBT data.

Velocity Profile - Water Column			
depth (meters)	velocity (meters/sec)	depth (meters)	velocity (meters/sec)
0.	1494.0	712.5	1480.9
16.1	1492.4	819.8	1481.0
37.5	1490.8	870.8	1481.1
53.9	1489.9	900.0	1481.2
75.0	1489.0	937.5	1481.3
109.2	1487.8	975.0	1481.4
150.0	1486.6	1016.3	1481.5
185.0	1485.7	1050.0	1481.6
225.0	1484.8	1136.3	1482.0
259.8	1484.1	1200.0	1482.4
300.0	1483.4	1358.9	1483.8
333.7	1482.9	1500.0	1485.2
375.0	1482.4	1555.0	1485.7
409.8	1482.1	1831.0	1488.0
450.0	1481.8	2013.0	1490.2
483.6	1481.5	2172.0	1492.5
525.0	1481.2	2461.7	1496.9
600.0	1481.0	2800.0	1502.0
628.6	1480.9	2853.0	1502.8
675.0	1480.8		

Table 3.2 Velocity profile in the water column

3.3.3 Sea Floor Depth

Two sources of information for estimating the sea floor depth were used. An iterative method that uses data collected from the streamer hydrophone was used to estimate both shot and sea floor depths. Not all shots had streamer data that could be used, so the number of estimates using this method is limited.

A second estimate of sea floor depth was obtained from an oceanographic map of the Monterey fan ('Oceanographic Data of the Monterey Deep Sea Fan', 1st Edition, June 1975 by T.E. Chase, W.R. Normark, and P. Wilde. Prepared at the Geologic Data Center, Scripps Institution of Oceanography, IMR Tech Rept. Series TR-58). Both sources indicate a slope of about .4 degrees out to a range of 20 km, and a slope of 1.4 degrees beyond that range. Sea floor depth as a function of range from FLIP is given below.

Shot Location					
Shot	Radar Range	Arrival Angle (D)	Raytrace along direct path		
			Range	Depth	Time
39	5741	3.407	5744	1799	3.867
15	5834	3.919	5826	1853	3.923
40	7408	2.900	7424	1771	4.996
17	7871	2.900	7880	1775	5.303
41	9075	2.896	9080	1778	6.109
19	9816	3.066	9868	1805	6.639
37	11575	3.066	11534	1794	7.759
21	11631	3.237	11657	1820	7.841
43	12594	3.407	12581	1817	8.462
23	13890	3.237	13876	1778	9.333
36	14075	3.407	14075	1776	9.467
44	14168	3.578	14164	1795	9.526
45	15742	3.919	15741	1794	10.585
25	16112	4.089	16119	1813	10.839
46	16946	4.260	16955	1812	11.400
27	18057	4.602	18054	1797	12.138
47	18520	4.943	18533	1820	12.458
29	20187	5.456	20182	1819	13.564
48	20650	5.542	20649	1794	13.878
31	22039	5.798	22038	1729	14.812
49	22594	6.141	22592	1768	15.180
33	23706	6.483	23709	1760	15.928
50	24817	7.000	24817	1817	16.665
51	26576	7.513	26572	1818	17.836
52	28613	7.856	28610	1706	19.205

Table 3.3 Shot locations. Rays were traced from the array at the angle of arrival along the direct water path (D) until range along the ray matched the radar range recorded when the shot was launched. The depth at this range is assumed to be the shot depth. Ranges and depths are reported in meters.

3.3.4 Removing the water path contribution

Having identified the arrivals and found the shot locations, rays may be traced from the shot and from the array down to the sea floor. A time origin was not available so times in the sediment were found from the time difference between the direct and refracted paths.

Sea Floor Depth			
range from FLIP (meters)	depth (meters)	range from FLIP (meters)	depth (meters)
0	2800	9700	2861
2100	2813	11400	2871
3100	2819	11630	2873
3900	2824	20190	2932
4900	2831	22040	2973
5300	2833	24820	3009
6900	2843	26580	3086
8000	2850	32410	3232
9100	2857		

Table 3.4 Sea floor depth

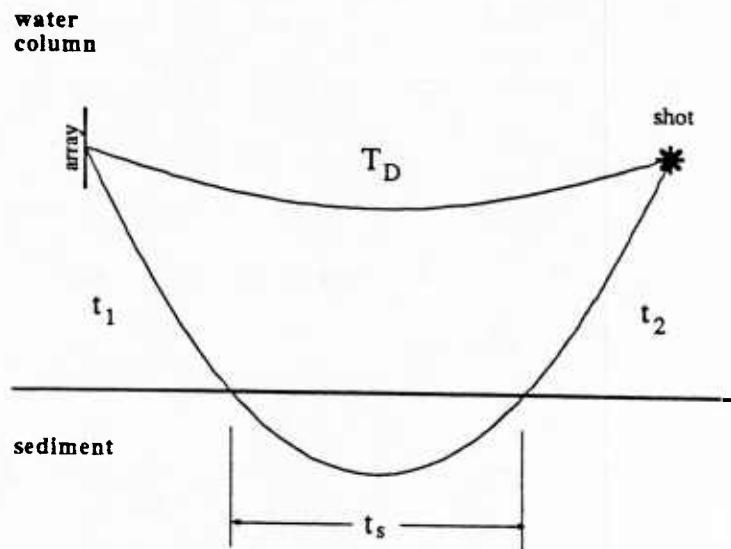


Figure 3.4 Removing the water path contribution.

With reference to Figure 3.4, define:

T_R	Total time for sediment refracted raypath (including time spent in the water column)
T_D	Total time for the direct path (water column)
t_1	Time from the array to the floor
t_2	Time from the shot to the floor
t_S	Time in the sediment

The total time for the sediment refracted raypath is

$$T_R = t_1 + t_2 + t_S$$

The time difference between the sediment and direct path is

$$\begin{aligned} \Delta t &\equiv T_R - T_D \\ &= t_1 + t_2 + t_S - T_D \end{aligned}$$

Therefore the time that the ray spends in the sediment is given by

$$t_S = \Delta t + T_D - t_1 - t_2 \quad (3.1)$$

All of the variables on the right side of (3.1) may be found.

- Δt is found from the array time series (time difference between the direct and sediment refracted paths).
- T_D is obtained by raytracing (or streamer data if available).
- t_1, t_2 are obtained by raytracing.

Ranges in the sediment corresponding to times t_S are found by raytracing. The ranges associated with times t_1 and t_2 are subtracted from the shot range (from FLIP to the shot). Angles used to trace rays from the array are listed in Table 3.1. Shot ranges are given in Table 3.3. Time differences between the direct and refracted paths (Δt) are listed in Table 3.5.

Data from longer range shots contain a considerable amount of error. So much of the ray's total range and time is spent in the water column that errors can be larger than the range and time spent in the sediment. For this reason, shots beyond a range of 20 km are not used.

Arrival Time Differences				
difference in time (ms) between direct and refracted paths				
Shot	BR	BR-S	S-BR	S-BR-S
39	335			
15	321			
40	242			
17	221			
41	184	1246		
19	158	1102	1260	
37	127	922	1054	
21	123	891	1042	
43	109	832	974	2537
23	98	769	845	2007
36	90	740	831	1992
44	89	745	845	1940
45	76	680	757	1793
25	63	645	745	1744
46	61	627	708	1675
27	50	582	652	1532
47		569	656	1530
29		520	600	1404
48		519	591	1389
31		479	549	1291
49		467	547	1281
33		450	515	1211
50		439	508	1184
51		421	477	1117
52		405	464	1056

Table 3.5 Arrival time differences between direct and refracted paths. Differences in arrival times were found from hydrophone 15 of the array time series. This is roughly the middle of the upper half (high gain portion) of the array. Arrival angles given in Table 3.1 were found for this section of the array.

3.4 Re-parameterization of the data

$T(X)$ is not a particularly good form for the data when trying to infer velocity structure. Small changes in the travelttime curve cause large changes in the model. It is common to parameterize range and time as functions of ray parameter p . While this results in a more stable form of the data, $X(p)$ and $T(p)$ are sensitive to errors made in estimating p , and to lateral inhomogeneities.

A linear combination of $X(p)$ and $T(p)$, called the delay time, is defined as: $\tau(p) = T(p) - pX(p)$. Unlike $X(p)$ and $T(p)$, the delay time is a monotonically decreasing function and is sensitive only to second order, to errors in p [10].

Suppose there is an (X, T) pair which corresponds to a true ray parameter of p_0 . If an incorrect ray parameter p_1 is estimated for this data pair, errors will be introduced into the $X(p)$ and $T(p)$ data since the point $(X(p_1), T(p_1))$ is off the correct traveltime curve. $\tau(p)$ is somewhat insensitive to these errors; even though an incorrect value of $p = p_1$ is used, $\tau(p_1)$ will still be correct to first order.

The price that is paid for this insensitivity to errors is a loss of some detail in the velocity profile. The smoothness of the $\tau(p)$ curve can make it difficult to recover details in the velocity profile. Orcutt, MacKenzie and McClain clearly illustrate this [53, Fig. 2]. $\tau(p)$ and $X(p)$ data are generated for two distinctly different velocity profiles. While the two $X(p)$ curves are quite different, the two $\tau(p)$ curves are very similar. Given noise in the data, it would be difficult to recover the two velocity profiles from the $\tau(p)$ data. Although the two velocity profiles could be recovered from the $X(p)$ data, this data is sensitive to errors in estimating p and to lateral inhomogeneities.

Expressing X as a function of p is often a difficult step. By definition, the ray parameter is given by $p = (dT/dX)$, the slope of the traveltime curve at a particular (X, T) pair. This seldom produces acceptable results however, since numerical differentiation of noisy data is an unstable procedure.

A standard technique for estimating p is to fit a polynomial through $T(X)$ and then differentiate the polynomial. This is better than trying to find the slope from discrete points along the traveltime curve, but fitting a polynomial to the data can smooth over small variations in the traveltime curve which provide detail in the velocity profile. Although methods exist for obtaining suitable bounds on $\tau(p)$ without actually estimating p [34, 35, 52, 53], converting the data into a function of p is a difficult and error-prone step in most seismic studies.

The problem of having to estimate p from the traveltime data is essentially side-stepped in this study. Since an array was used to receive the acoustic energy, the ray parameter can be calculated from Snell's law. If a medium is laterally homogeneous and horizontally layered, then p is constant along the entire raypath and $p = u \sin(\theta)$. $u(z)$, the reciprocal of velocity, is called slowness: $u(z) = 1/v(z)$. θ is the angle the ray forms with the vertical. The angle of arrival may be found by beamforming and thus p can be calculated. (Note: angle of arrival values reported in Table 3.1 were measured with respect to the horizontal, so $\theta = 90^\circ - \text{angle of arrival}$.)

$X(p)$ will be used in the least squares inversion in order to gain the detail available from this form. Having an good estimate of p associated with each X eliminates the necessity of fitting a polynomial through the traveltime data, or using $\tau(p)$. Details that might otherwise be lost will thus be preserved. $\tau(p)$ will be used in the linear programming inversion to obtain extremal bounds. Here the intent is to produce bounds, the smoothing that occurs from using $\tau(p)$ is perfectly acceptable. $X(p)$ data will be incorporated into this method as additional constraints.

The traveltime data and its various parameterizations are listed in Table 3.6 and illustrated in Figures 3.5a-d.

Sediment traveltime data			
$p \times 10^3$	X	T	$\tau(p)$
.49692	3116	1.933	.38460
.51783	3033	1.860	.28942
.52756	2713	1.708	.27673
.52756	2778	1.694	.22844
.53380	2896	1.807	.26112
.56745	1918	1.253	.16463
.57248	1997	1.285	.14176
.57493	2059	1.345	.16122
.58436	1665	1.074	.10104
.58436	2209	1.417	.12615
.58664	2387	1.529	.12869
.58776	1742	1.131	.10712
.58997	1549	1.006	.09214
.59215	1366	.927	.11812
.59322	1447	.958	.09961
.59744	2019	1.309	.10277
.60450	1590	1.047	.08585
.60450	1820	1.168	.06781
.60644	1865	1.208	.07699
.60836	1604	1.037	.06119
.61208	1753	1.157	.08402
.61479	1739	1.145	.07588
.61568	1496	.979	.05794
.61829	1945	1.261	.05843
.62167	1751	1.143	.05446
.62413	1967	1.300	.07234
.62573	1320	.867	.04104
.62730	1606	1.054	.04656
.62884	1547	1.021	.04819
.63035	2072	1.367	.06092
.63257	1176	.775	.03110
.63472	1111	.733	.02783
.63611	1166	.782	.04030
.63816	1264	.842	.03537
.63816	1813	1.199	.04202
.64078	1426	.943	.02925
.64268	1092	.725	.02319
.64512	1140	.762	.02656
.64630	1289	.852	.01892
.65323	1048	.697	.01242
.65428	880	.588	.01223
.65569	1205	.802	.01189
.65793	1078	.722	.01275
.65920	572	.384	.00694
.66080	704	.476	.01080
.66119	745	.495	.00241
.66193	598	.403	.00717

Table 3.6 X, T, and τ data

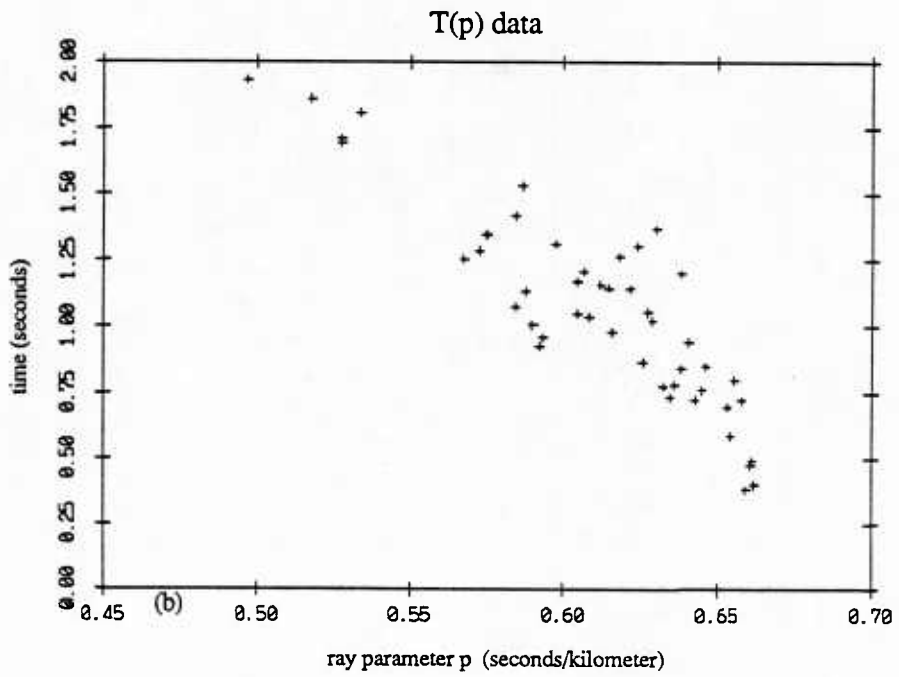
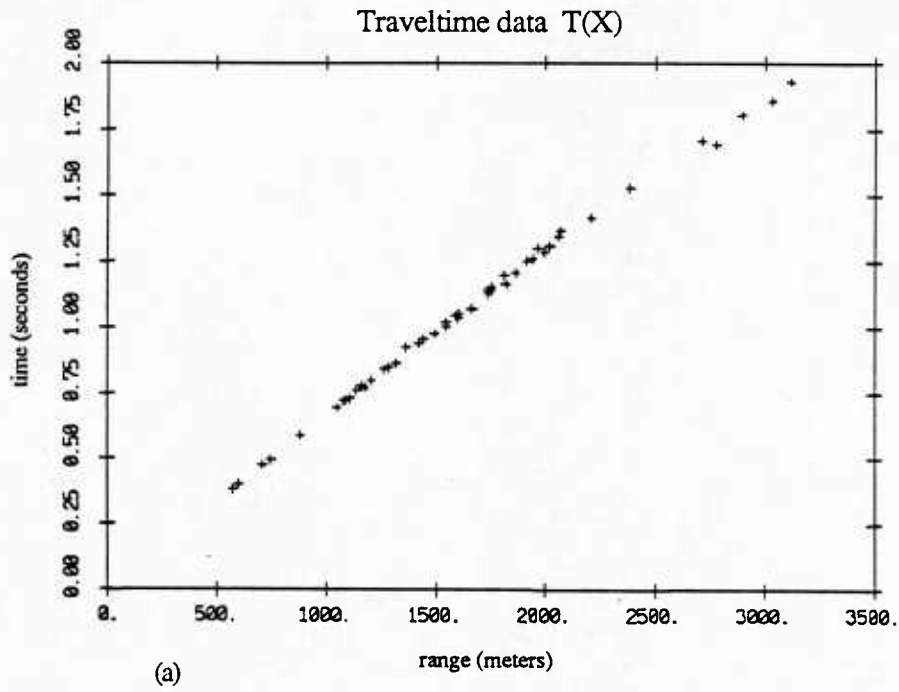


Figure 3.5 (a) $T(X)$ data, (b) $T(p)$ data.

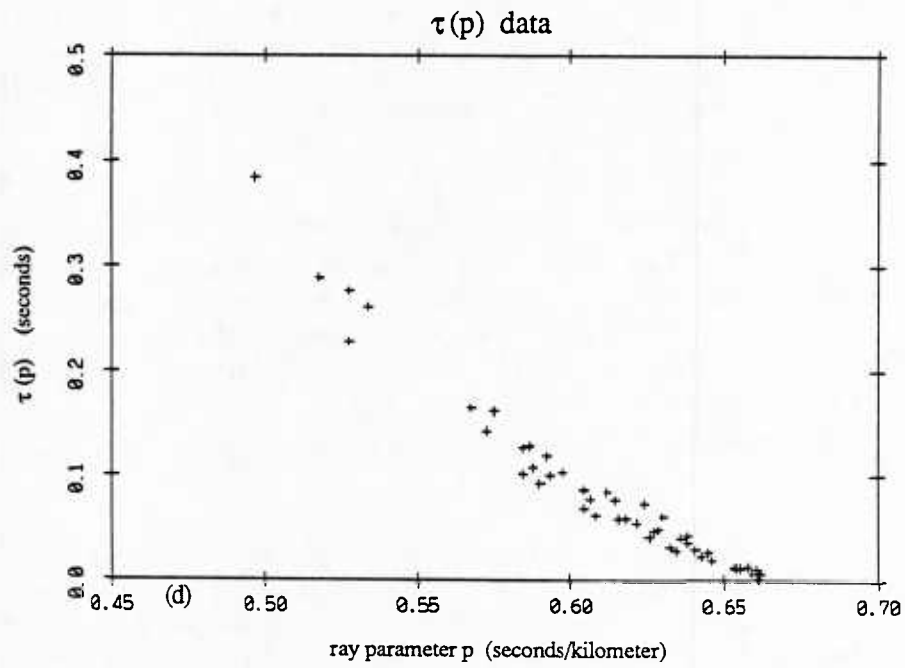
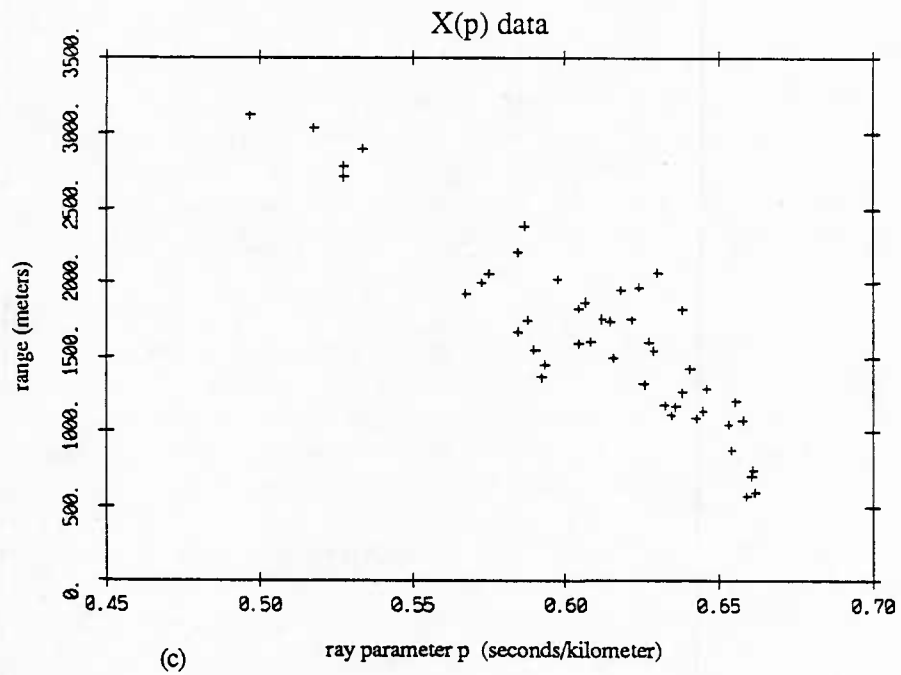


Figure 3.5 (c) X(p) data, (d) $\tau(p)$ data.

3.5 Sources of error

There are several sources of error responsible for scatter in the travel-time data. These are present from uncertainties occurring during the experiment and also errors introduced during processing of the data. Each source of error will be discussed and, when possible, an estimate made of its effect on the data. In most cases, only an order of magnitude estimate can be made.

The water column and sediment are assumed to consist of horizontal, laterally homogeneous layers. Velocity is assumed to increase with depth. Variations in topography (such as sloping interfaces or lateral inhomogeneities) and velocity anisotropy violate the model assumptions and introduce errors. The region in which the experiment was conducted is relatively flat, but in an area of rapid deposition and turbidity currents, lateral inhomogeneities and velocity anisotropy are to be expected. Alternating layers of high and low velocity material where lithification begins to occur can also cause scatter in the travel-time data. Without more information about subsurface layering it is difficult to assess the magnitude of the errors introduced by these effects.

Arrival time errors.

Arrival time errors occur when arrival times are picked from the array time series. These errors are relatively small, typically on the order of a few milliseconds. Even for the deeply refracted rays whose onset time is less distinct, uncertainties in arrival time picks are at most about 20 milliseconds. For a sound speed of 1500 meters/sec this corresponds to an error in range of at most 30 meters (usually much less).

Errors in X and T that show up from errors in estimating p .

Dorman [10] has shown that errors in estimating p can have a significant effect on uncertainties in X . In parameterizing the data as $X(p)$, ray parameter p is the independent variable and range X is the dependent variable. The independent variable is usually considered to be free of error; all errors show up in the dependent variable.

The total error in X is made up of two terms.

$$E_T = E_X + E_p$$

There are measurement errors in X (denoted E_X). These would arise from errors affecting range estimates, such as incorrect shot depth or radar ranges, a less than perfect water column velocity profile, lateral inhomogeneities, etc. There are also errors in X that show up due to incorrect estimates of the ray parameter p (denoted E_p).

Assume there is a traveltime pair (X, T) that corresponds to ray parameter $p = p_0$, but an incorrect estimate of $p = p_1$ is made. The estimate $X(p_1)$ does not lie on the true traveltime curve (the correct value is $X(p_0)$). The error in X due to the incorrect value of p is

$$E_p = X(p_1) - X(p_0) \tag{3.2}$$

Let the error in estimating p be defined as $\delta p = p_1 - p_0$, and express $X(p_1)$ by a Taylor series expansion about $X(p_0)$.

$$X(p_1) = X(p_0) + \left(\frac{dX}{dp}\right)_{p_0} \delta p + O(\delta p^2) + \dots$$

Dropping the higher order terms and substituting into (3.2) gives

$$E_p = \left(\frac{dX}{dp}\right)_{p_0} \delta p \quad (3.3)$$

Since $p = \frac{dT}{dX}$; $\frac{dp}{dX} = \frac{d^2T}{dX^2}$ and we have that

$$\frac{dX}{dp} = \left(\frac{dp}{dX}\right)^{-1} = \left(\frac{d^2T}{dX^2}\right)^{-1} \quad (3.4)$$

Using equation (3.4) in (3.3) gives

$$E_p = \left(\frac{d^2T}{dX^2}\right)^{-1} \delta p \quad (3.5)$$

Note that $\frac{d^2T}{dX^2}$ is the curvature of the traveltime curve. As the traveltime curve approaches a straight line, the reciprocal of the curvature becomes infinite (a straight line has $\frac{d^2T}{dX^2} = 0$). Equation 3.5 shows that errors in estimating p can be greatly magnified. It is possible that errors due to uncertainties in estimating p (E_p) could dominate errors due to uncertainties in range measurements (E_X).

To examine the effect of uncertainties in p in the context of this data set, the curvature of the traveltime data will be estimated and used with a reasonable value of δp to find the resulting error in range. Fitting a quadratic through the traveltime data (Table 3.6) yields the equation

$$T = .0012 + 7.5 \times 10^{-4} X - 8.5 \times 10^{-8} X^2$$

so that

$$\left(\frac{d^2T}{dX^2}\right)^{-1} \approx 6 \times 10^6 \text{ meters}^2/\text{sec}$$

From equation 3.5 the error in X due to errors in estimating p is

$$E_p = \left(\frac{d^2T}{dX^2}\right)^{-1} \delta p = (6 \times 10^6) \delta p \quad (3.6)$$

Since the data were received at an array, p is calculated from Snell's law: $p = u \sin(\theta)$. Given the high signal to noise ratio of the data, most of the error in p should be due to the finite number of look directions that were available (the beamformer used for angle of arrival estimation only allowed an

integer number of sample delays). This error in p for the steepest ray (where the effect is most severe) amounts to 2×10^{-6} sec/meter. This results in an error E_p on the order of 10 meters. Having an array and high signal to noise ratio data has kept this type of error small.

Errors in removing the water path contribution.

The largest errors occur when the range and time spent in the water column are subtracted from the ray's total range and time. The time spent in the water column is much greater than the time spent in the sediment, so even small errors in subtracting the water path are a large percentage of the sediment travelttime. These errors are primarily due to having an inexact velocity profile for the water column. This affects both the actual tracing of rays to the sea floor as well as the determination of shot locations (see Section 3.3.2). An additional error in shot location occurs if the explosive charge does not descend vertically (it may drift horizontally due to currents). Other errors include those due to a finite number of look directions (about 25 meters) and uncertainties in radar ranges, which should be accurate to within 30 meters. Since the correct velocity profile is not available, it is difficult to know the error introduced by using an estimate.

Total error

An examination of scatter in the data indicates a total uncertainty in range of about one kilometer, and in time of about .6 seconds. Most of this occurs in removing the water path. The biggest reduction in scatter of the data would result from an improved estimate of the velocity profile in the water column.

3.6 Inverting the data

Two methods will be used to invert the data. The problem will first be solved using a least squares approach. This solution yields velocity as a function of depth. A second inversion, using a linear programming method, produces bounds on the velocity profile. All models that are consistent with the data lie within these bounds. These bounds indicate in an unambiguous way, what can be inferred from a finite set of data with errors. A single velocity profile is needed for acoustic modeling; the least squares solution provides this. The linear programming solution provides a way to assess the quality of the solution.

3.6.1 Least squares solution

In this approach the sediment is modeled as a horizontally layered, laterally homogeneous medium. Velocity is assumed to increase with depth. Layers in the model are defined by specifying a slowness value for each interface (depths to the interfaces are not known). Each layer is described by a constant slowness gradient. The least squares solution yields the unknown slowness gradients. Layer thicknesses may be found from the gradients and the interface slowness values ($dz/du \times du = dz$). Velocity as a function of depth is then found by integrating the layer thicknesses. The matrix equation that is inverted to obtain the unknown gradients is derived in Appendix A1. Details of the model are also described in this appendix.

A singular value decomposition [15, 39, 41, 66] was used to invert the matrix equation (A1.12). No zero singular values were obtained for any of the models that were examined. The largest difference in eigenvalues, occurring for a five layer model, was $\lambda_{\max}/\lambda_{\min} = 6.34$, indicating a well conditioned matrix. In all cases that will be presented, solutions were constructed using the maximum number of eigenvectors. The maximum number of eigenvectors is equal to the number of layers in the model (the number of columns).

The velocity profile in the upper sediments is usually represented by a monotonically decreasing function that changes smoothly with depth [22, 23, 24]. Defining constant gradients in each layer of the model allows representation of such a function by only a few layers. At best, it is unnecessary to use many more layers, and at worst, is likely to cause problems in the least squares inversion. If the number of layers in the model approaches or exceeds the number of data, then gradients are found for layers in which few, if any rays turn. This often leads to physically unreasonable solutions.

To examine the effect of model selection on the solution, $X(p)$ data are inverted for models ranging from one to five layers (Figures 3.6-3.10). Three plots for each inversion will be presented. The first plot (*a*) shows the velocity profile obtained from the inversion. The profile suggested by Hamilton is included for comparison. In (*b*) and (*c*), theoretical $X(p)$ and $\tau(p)$ curves are generated from the velocity profile and plotted along with the experimental data.

Figure 3.6 shows the result for a one layer model. Velocity gradients in the upper sediments change with depth (overall, they decrease as depth increases) so a single layer would not be expected to provide a good fit. As seen in Figure 3.6b, the the $X(p)$ data generated from the velocity profile does not fit the experimental data very well for values of p less than .55. Most of the data is from values of p greater than .55, so the emphasis in the solution is focused more on this region. The remaining models fit the data more closely. As suggested in Section 3.4, there is not much difference in the $\tau(p)$ curves generated from velocity profiles that clearly differ. Figure 3.11 shows the 3 and 4 layer solutions with their 90% confidence bounds. Details of these velocity profiles are summarized in Tables 3.7 and 3.8.

With a finite data set there are an infinite number of models that will fit the data, and a single model must be (often somewhat arbitrarily) selected. A four layer model adequately describes the velocity profile without running into problems with data density, and will be used in the subsequent analysis.

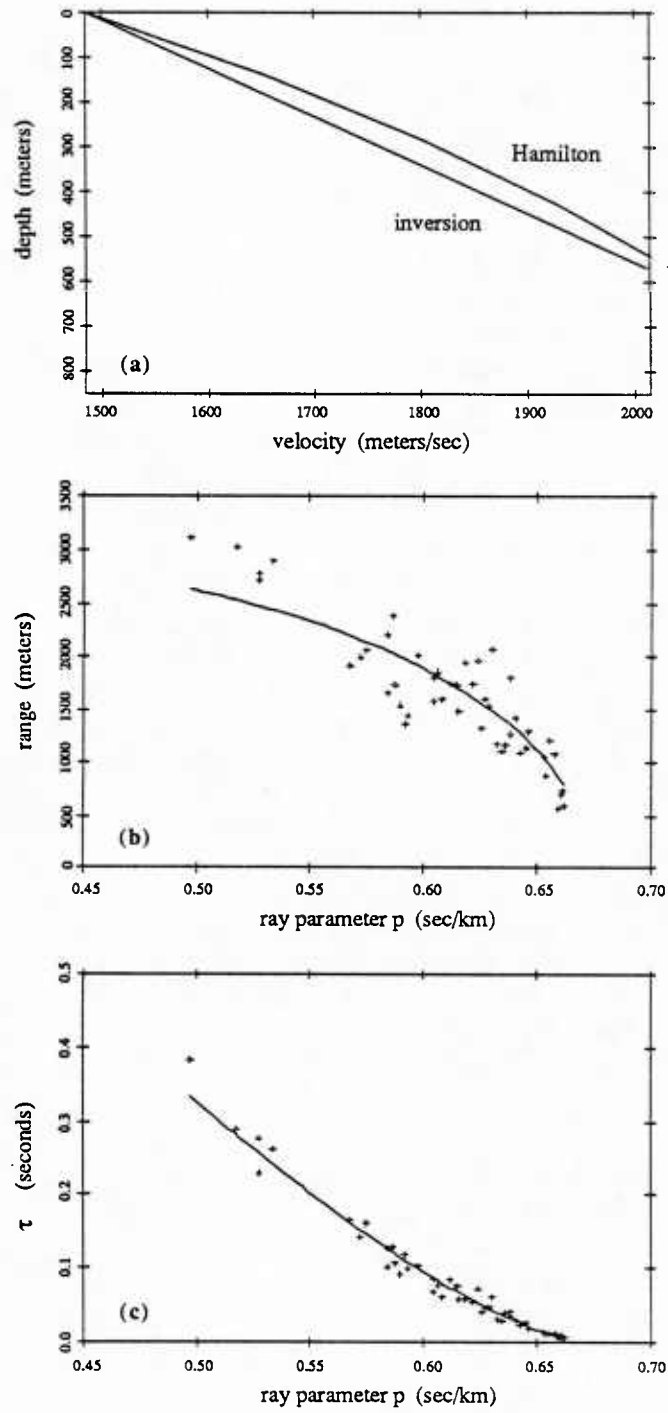


Figure 3.6 Inversion using a one layer model. (a) velocity profile obtained from inversion. (b) and (c) show data generated from the velocity profile in part (a) (solid line) along with the experimental data.

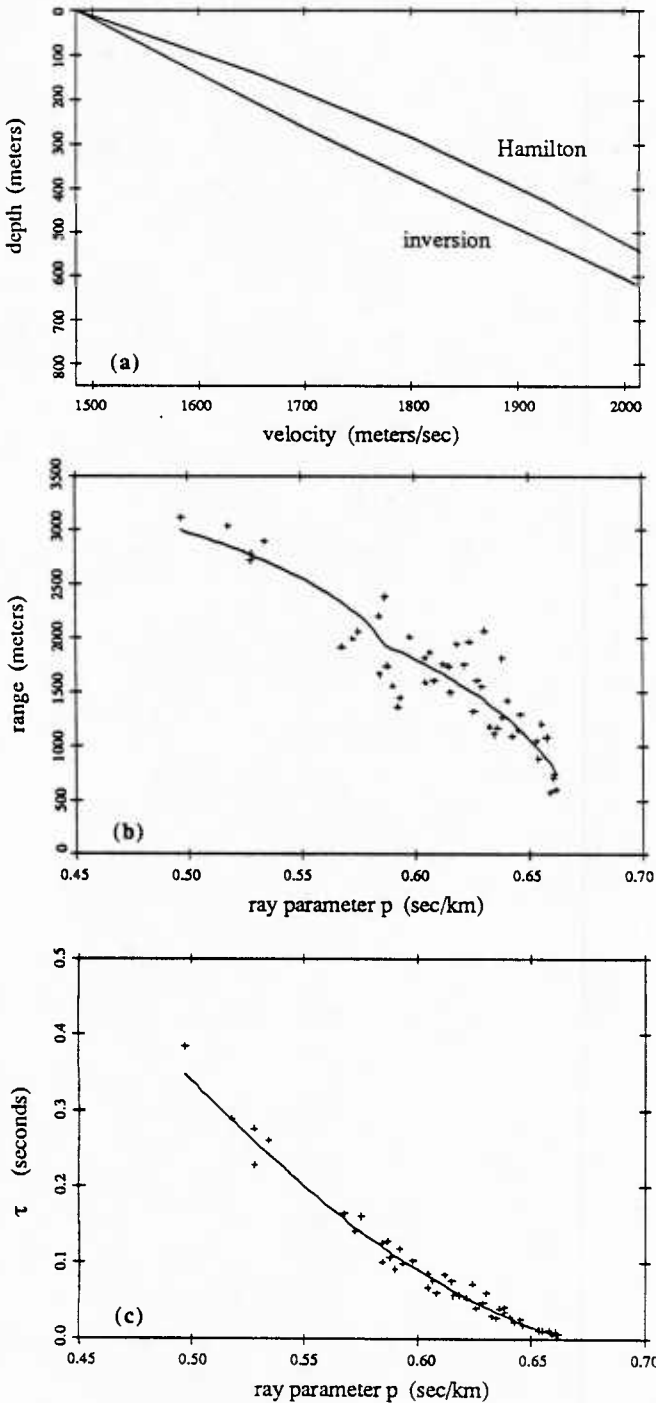


Figure 3.7 Inversion using a two layer model.
(a) velocity profile obtained from inversion. (b) and (c) show data generated from the velocity profile in part (a) (solid line) along with the experimental data.

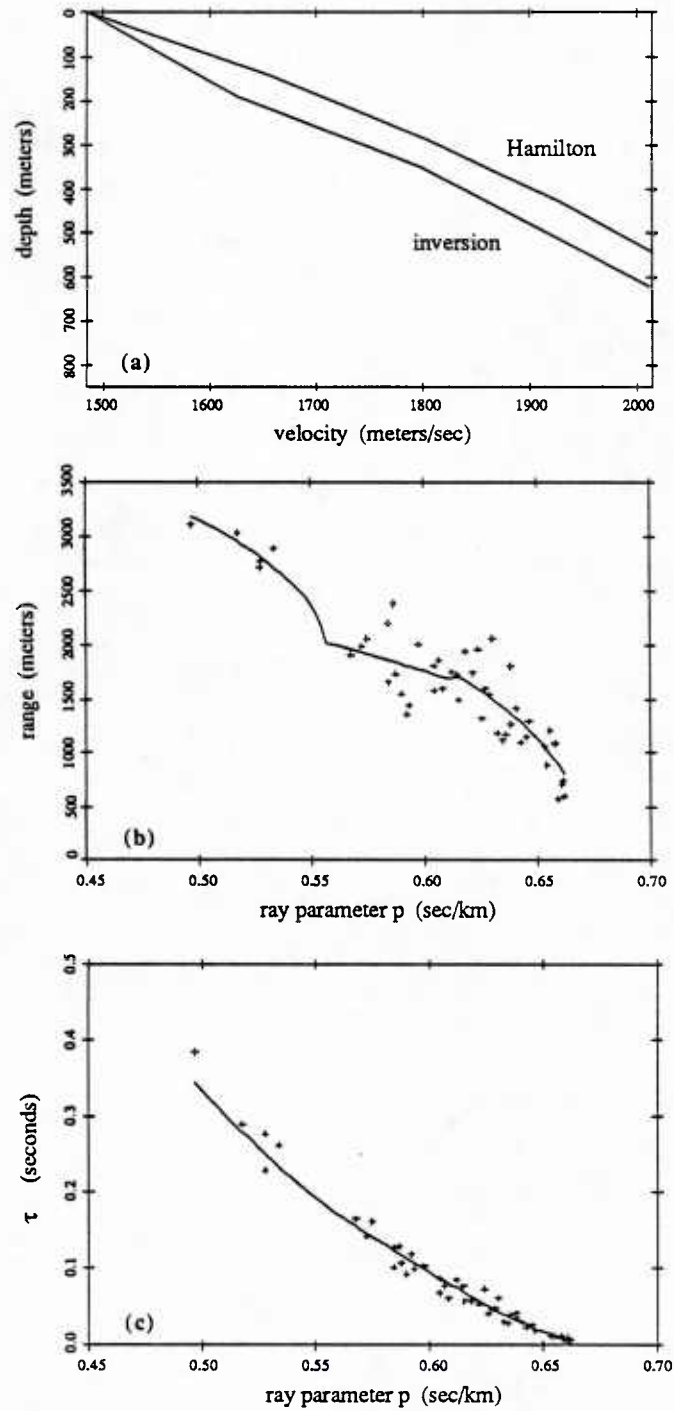


Figure 3.8 Inversion using a three layer model.

(a) velocity profile obtained from inversion. (b) and (c) show data generated from the velocity profile in part (a) (solid line) along with the experimental data.

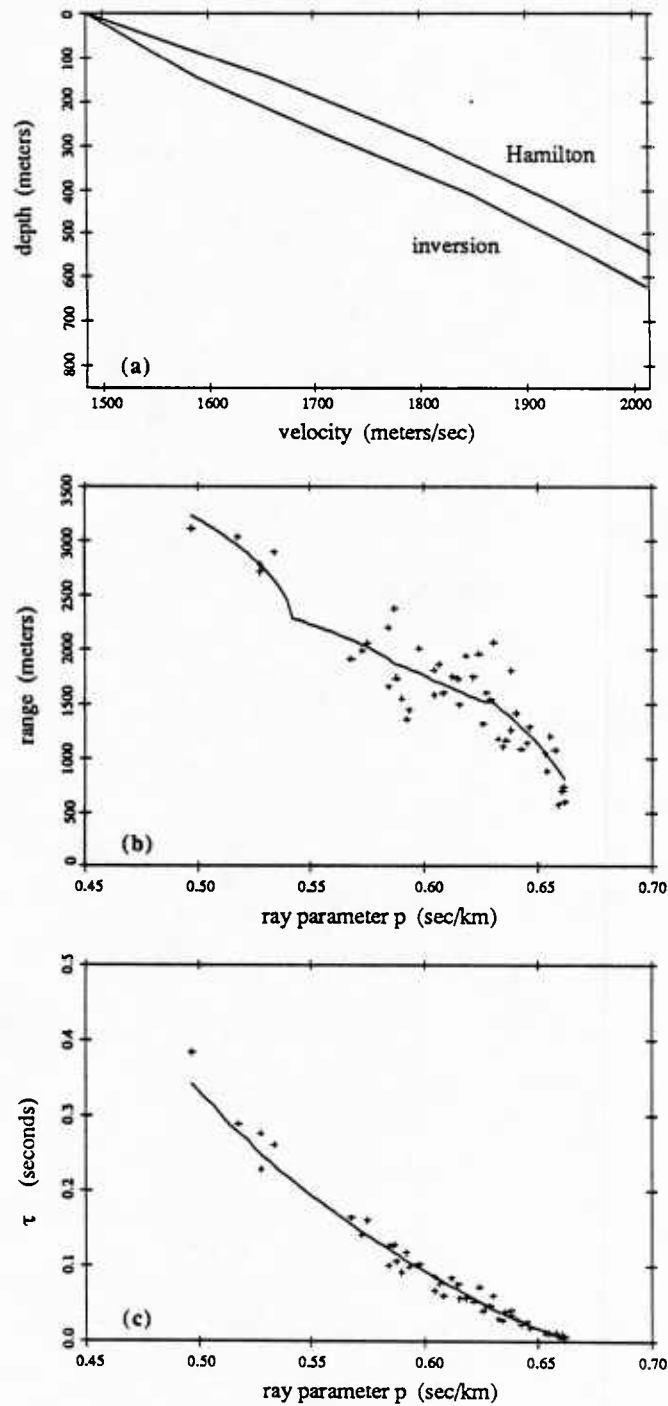


Figure 3.9 Inversion using a four layer model.

(a) velocity profile obtained from inversion. (b) and (c) show data generated from the velocity profile in part (a) (solid line) along with the experimental data.

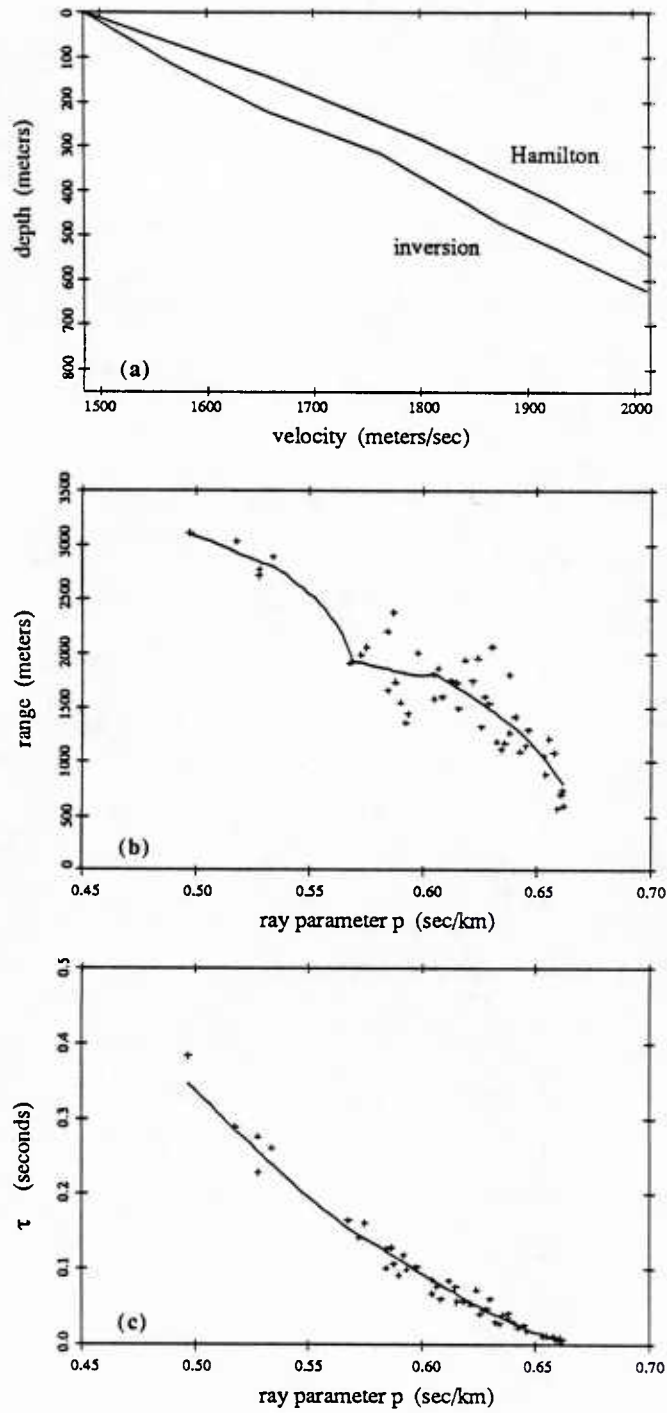


Figure 3.10 Inversion using a five layer model.

(a) velocity profile obtained from inversion. (b) and (c) show data generated from the velocity profile in part (a) (solid line) along with the experimental data.

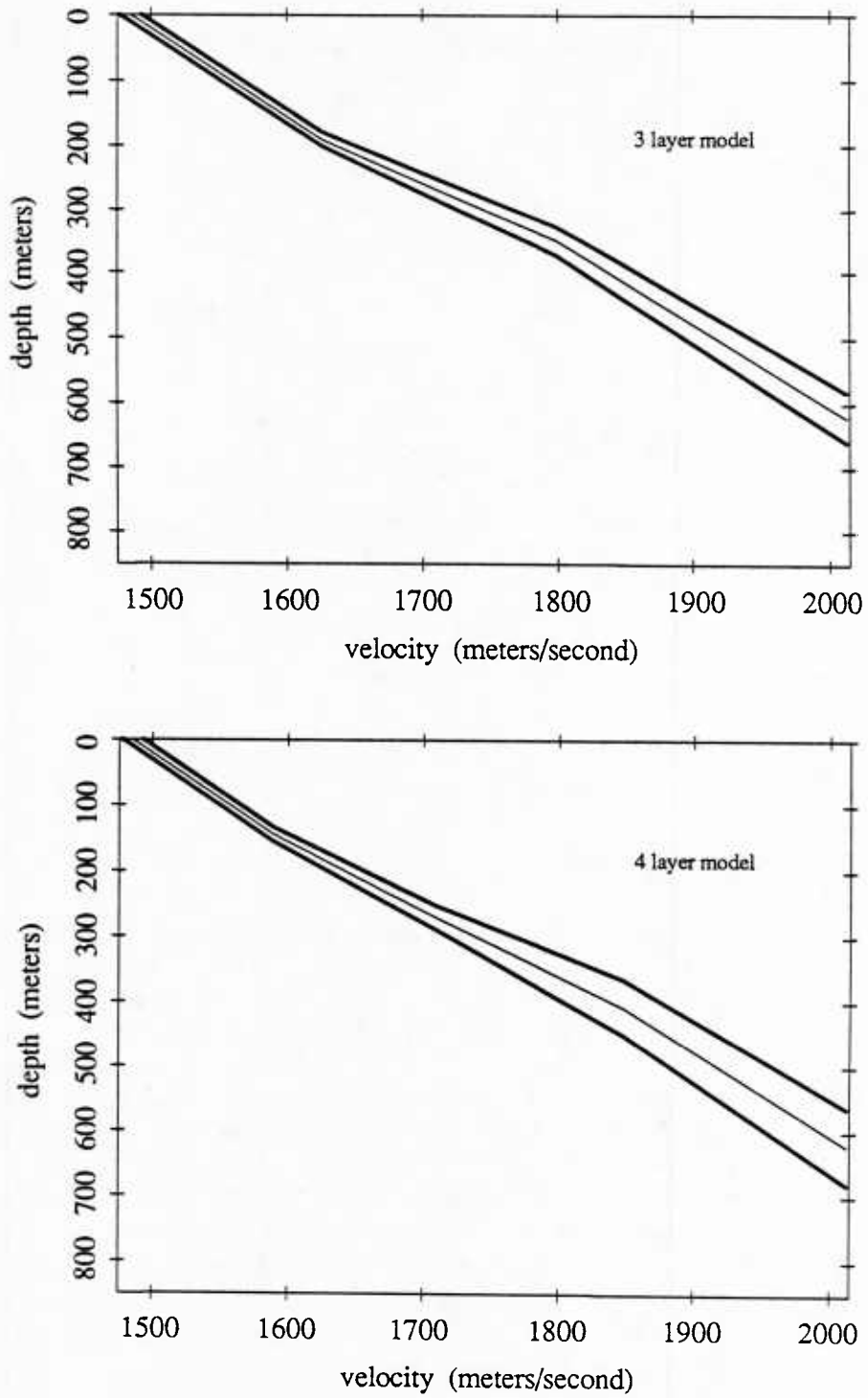


Figure 3.11 90% confidence bounds for the 3 and 4 layer models.

Velocity Profile - 3 layer model			
interface	depth (meters)	velocity (meters/sec)	gradient (sec ⁻¹)
1	0.	1484.8	
2	190.8	1627.0	.745
3	349.9	1799.3	1.083
4	620.7	2012.4	.787

Table 3.7 Velocity profile in the sediment for a three layer model.

Velocity Profile - 4 layer model			
interface	depth (meters)	velocity (meters/sec)	gradient (sec ⁻¹)
1	0.	1484.8	
2	144.1	1588.9	.722
3	269.7	1708.8	.955
4	408.3	1848.2	1.006
5	621.6	2012.4	.770

Table 3.8 Velocity profile in the sediment for a four layer model.

3.6.2 Linear programming solution

The solution to a linear programming problem minimizes or maximizes an objective function subject to a set of constraints. In this case, bounds on the input data ($\tau(p)$, $X(p)$, etc.) form the set of constraints. The objective function is depth to a particular velocity. Extremal bounds on the velocity profile are found by selecting a number of velocities to evaluate. At each velocity two linear programming problems are solved. The minimum depth at that velocity that satisfies the constraints is found. Next, the maximum depth at that velocity, subject to the constraints, is found. When this procedure is performed at a number of different velocities, extremal bounds are swept out. These bounds define the minimum and maximum depths possible at each velocity that are consistent with the constraints (bounds) on the input data [14].

One advantage of this method is that additional information or constraints may be easily incorporated into the problem. Adding constraints on $X(p)$ data restricts the slope variations possible for the $\tau(p)$ data and can tighten the extremal bounds considerably.

Input bounds on the $\tau(p)$ and $X(p)$ data are shown in Figure 3.12. Extremal bounds found using only $\tau(p)$ data are given in Figure 3.13a. Much tighter bounds result (Figure 3.13b) when the $X(p)$ constraints of Figure 3.12b are included.

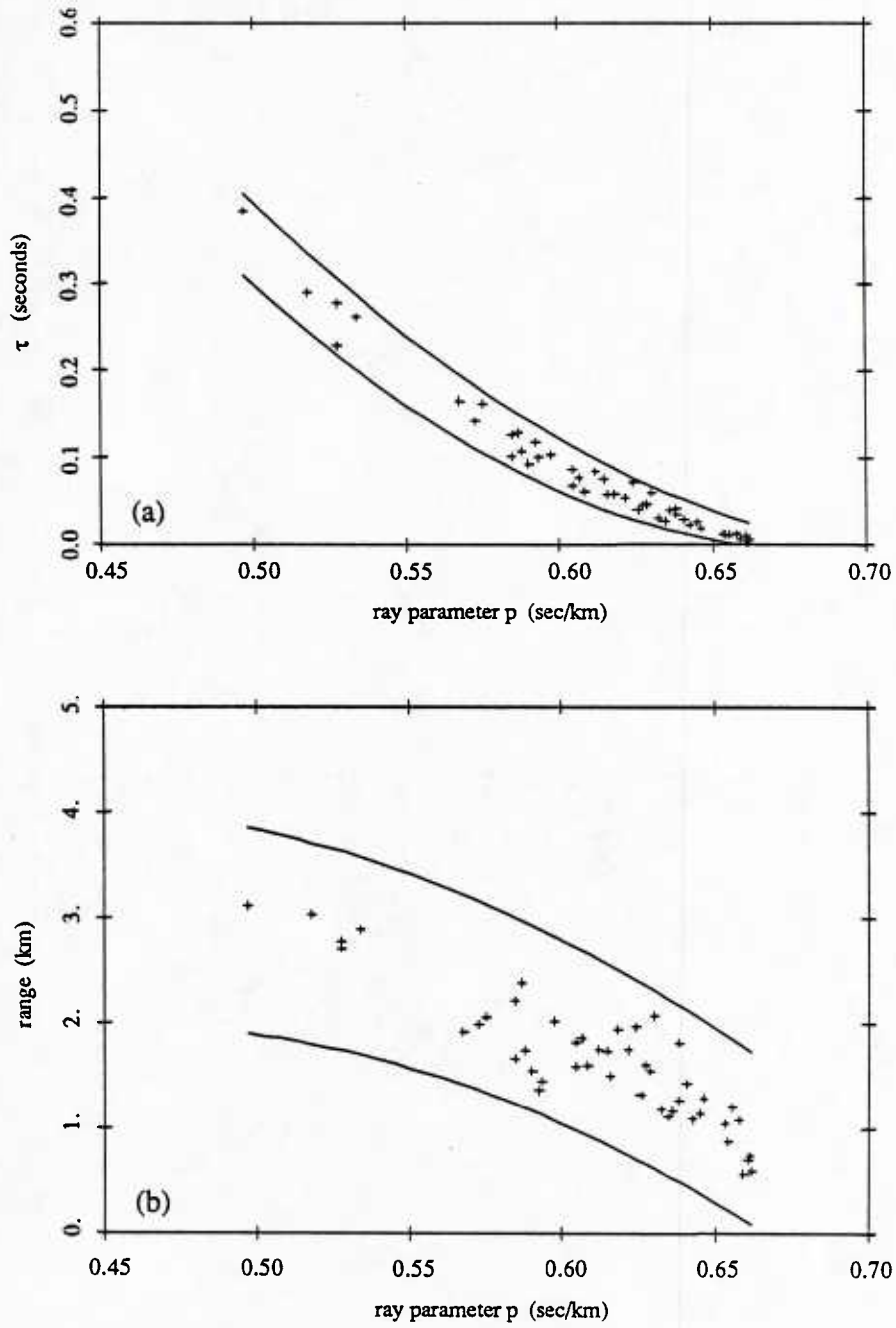


Figure 3.12 Input bounds on $\tau(p)$ and $X(p)$ data.

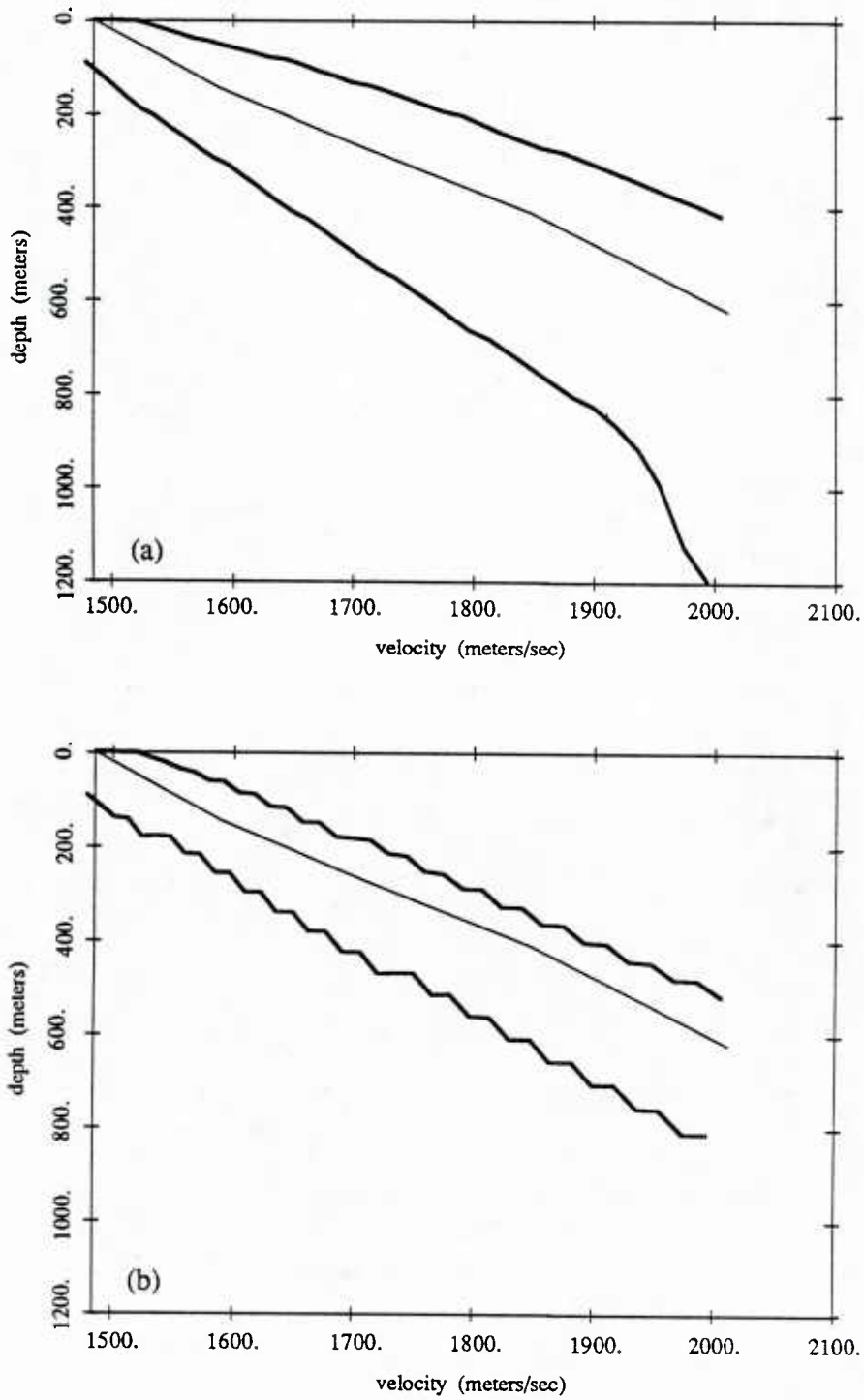


Figure 3.13 Linear programming solution.
 Extremal bounds (bold lines) are plotted along with the least squares solution.
 (a) inversion of $\tau(p)$ data only. (b) inversion of both $\tau(p)$ and $X(p)$ data.

3.7 Forward modeling

To provide a qualitative check on the results of Section 3.6.1, theoretical curves generated from the velocity profile (Table 3.8) will be compared with the experimental data. These are illustrated in Figures 3.14a-d.

The theoretical curves fit the data reasonably well except for the few data at the largest values of p . Large values of p correspond to the shallowest rays. They spend nearly all of their time in the water and merely graze the sediment. These data are most prone to error since such a large portion of their traveltime is subtracted off. If the initial velocity used in the inversion is increased from 1484.8 to 1494 m/sec, the resulting velocity profile has a shallower gradient in the first layer. The theoretical curves from this velocity profile fit the large p data better, but result in a poorer overall fit to the experimental data.

3.8 Discussion

Values of the velocity gradients presented in Tables 3.7 and 3.8 are consistent with previously published values for this type of sediment [11, 22, 24, 29]. The way these gradients change with depth - initially shallow, increasing to about one, and then decreasing - differs from the monotonically decreasing gradients usually reported. This feature appeared in all models that were examined, and velocity profiles which do not exhibit a steeper gradient between 150 and 400 meters do not fit the experimental data very well. In some cases this difference may be due to the way in which the data were analyzed. Two examples are given below.

Velocity profiles obtained from reflection data are found by averaging interval velocities. A second or third order regression through these points is used to describe velocity as a function of depth. A smooth profile is a natural result of this method.

In most refraction studies it has been necessary to fit the traveltime curve with a polynomial, and differentiate the polynomial to convert the data into a function of p . If a low order polynomial is fit through the traveltime data, small details which give structure to the velocity profile may be lost. Use of $\tau(p)$ data has a similar smoothing effect. These would both lead to smoother velocity profiles. In this study, beamforming at the array allowed the direct calculation of p and permitted the use of $X(p)$ data. Details contained in the traveltime data were preserved.

An increase in the gradient at around 150 meters, and the subsequent decrease at 400 meters indicates that a change in some physical property occurs near those depths. There are several physical processes that might account for this velocity structure.

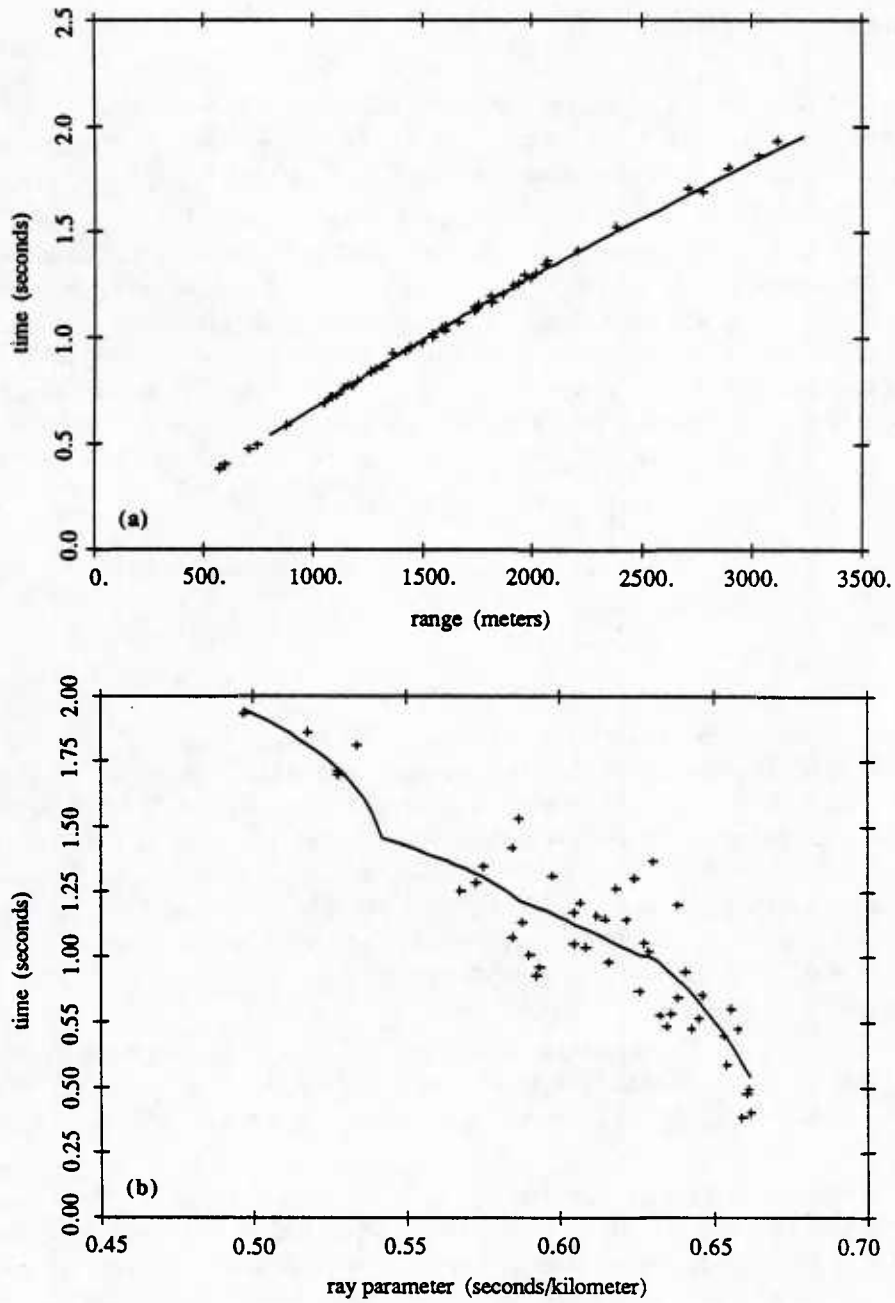


Figure 3.14 Forward modeling.

A theoretical curve generated from the velocity profile of Table 3.8 is plotted along with the experimental data. (a) T(X) data, (b) T(p) data.

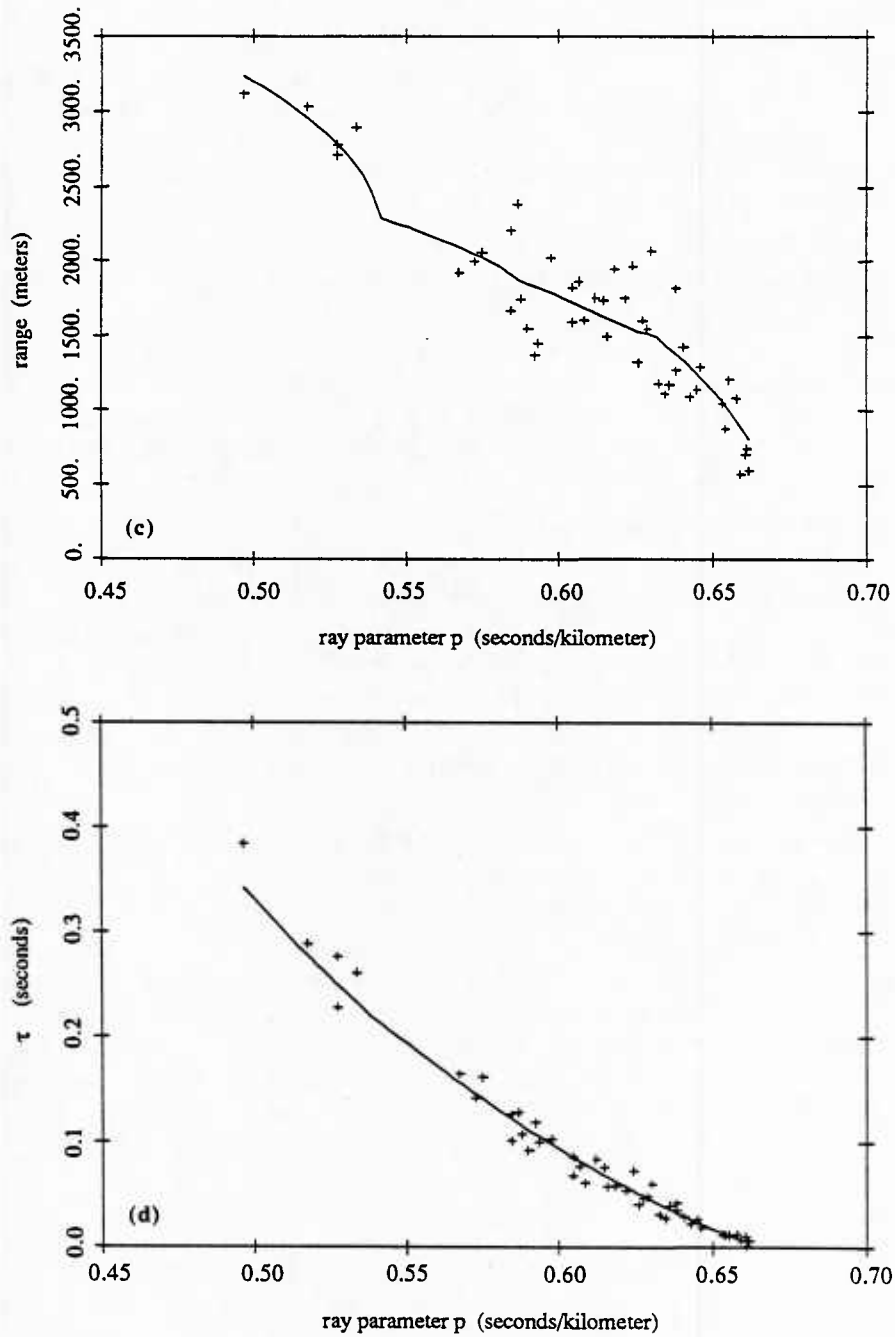


Figure 3.14 Forward modeling.

A theoretical curve generated from the velocity profile of Table 3.8 is plotted along with the experimental data. (c) $X(p)$ data, (d) $\tau(p)$ data.

Subsurface topography of deep sea fans can be very complex. Major events (rise or fall of sea level, turbidite flows, etc.), and changes in channel direction or activity can create irregular structures or cause primary areas of deposition to shift with time. The upper portion of the Monterey fan has a complicated history of development [27, 47, 48]. An irregular change in the velocity gradients with depth could be related to changes in sedimentation history. Velocity would be expected to change as age and sediment type vary.

Mineralogical changes that occur with depth could also produce a higher gradient at mid-depth. Lithification of the unconsolidated sediments is thought to begin between 200-400 meters depth. Cementation of the mineral particles increases frame rigidity. This higher velocity material would cause a steeper gradient. After lithification, there is little further increase in frame rigidity, or further decrease in porosity. Velocity increases more slowly with depth, resulting in smaller gradients.

Another mechanism that would account for these velocities involves the reduction of porosity. In regions with a high rate of deposition sediments may accumulate so rapidly that porosity does not have time to be fully reduced under overburden pressure. The lowest values of gradients in surficial sediments occur in such areas [22, pg. 920]. When porosity finally is reduced, there would be a rapid increase in velocity, causing a larger gradient. A collapse of the cardhouse structure and the resulting rapid increase of intergranular contacts could also play a role. After this occurs, gradients decrease with increasing depth, eventually reaching a nominal value.

Numerous reflection profiles on the Monterey fan exist, but correlating reflection profiles with refraction profiles can be misleading. Reflection data indicate changes in acoustic properties while refraction data give velocity information. A relatively thin layer of a different material may give a strong reflection, but would not necessarily affect the velocity gradients obtained by refraction data. A gradual change in velocity over a relatively large distance will produce a significant change in the gradient from the refraction data, but would show up weakly, if at all, on a reflection profile. Given the complex evolution of deep sea fans, subsurface topography is bound to play some role, but without a deep core from this area it is difficult to know which of the above is the more likely explanation.

4. Attenuation Estimation

4.1 Introduction

An estimate of the attenuation profile will be made using a method of spectral ratios (see Appendix A-2). The attenuation coefficient is proportional to the slope of the spectral ratio (spectrum of the sediment refracted arrival divided by the spectrum of the direct path arrival). The sediment will again be modeled as a horizontally layered medium, with each layer having a separate attenuation coefficient. Solving for each of the attenuation coefficients gives attenuation as a function of depth.

An attenuation peak in the sediment has been predicted but few single-experiment studies have been able to confirm this peak [19, 29, 30, 45, 63]. The results presented here show an attenuation peak at around 400-500 meters depth that is related to a change in sediment properties at that depth.

Hamilton has compiled data from a number of sources which indicate an approximate linear dependence of the attenuation coefficient k on frequency [19], and that velocity dispersion is negligible. Recent work has indicated that this may not be the case [28, 62]. The issue of frequency dependence is not addressed here, and it will be assumed that k is a linear function of frequency (Q^{-1} is independent of frequency).

Several mechanisms that can affect wave amplitude are discussed in the next section.

4.2 Attenuation in marine sediments

4.2.1 Factors affecting wave amplitude

Frictional losses [18, 19]

Frictional losses arise because of movement between the sediment particles. Internal friction varies with grain size, the number and kind of grain contacts, cohesion, and friction between silt and clay particles. The loss for this type of attenuation is linearly related to frequency. It is considered to be the dominant loss mechanism for sound propagation through the sediment. Porosity correlates well with attenuation in sediments since it is a good measure of the number of interparticle contacts.

Viscoelastic losses [61]

Viscoelastic losses occur when the pore water moves with respect to the mineral frame. Permeability of the sediment and viscosity of the interstitial

water are important factors for this type of attenuation. Attenuation is proportional to f^2 for low frequencies (less than 10 Hz) and \sqrt{f} for high frequencies (greater than 100KHz).

Scattering [61]

Rayleigh scattering occurs as wavelengths approach grain size. Attenuation due to Rayleigh scattering is proportional to f^4 . This should not be a factor in refraction studies because of the long wavelengths associated with the low frequencies that are used (at 100 Hz, the wavelength is about 15 meters).

Geometrical spreading [8, 50]

Spreading losses are not losses that result in an irreversible of conversion to heat, but cause wave amplitude to decrease by redistributing the energy over a larger area. In general, a spherical spreading loss model does not apply in sediments since the velocity changes as a function of depth (although in principle, if the velocity profile is known the spreading loss can be calculated). Losses due to geometrical spreading are not frequency dependent.

Reflection or transmission coefficients [50]

Layering of the sediment will cause a fraction of the energy to be reflected. The more energy that is reflected, the smaller the amplitude of the waveform becomes. Thus, the magnitude of reflection or transmission coefficients has an effect on the amplitude of the arrival. This effect is independent of frequency, but may be dependent on the angle of incidence as it crosses each layer. It is not always clear whether the sediment should be interpreted as consisting of many fine layers, a few thick layers, or something in between. Energy reflected at an interface is not lost through conversion to heat, and is not frequency dependent, but in the presence of many layers there may appear to be a frequency dependent loss due to the effect of intrabed multiples.

Intrabed multiples [50, 54, 55, 56, 58, 59]

Intrabed multiples refer to multiple reflections off layers that occur as the wavefront propagates through the medium. When an initially downgoing pulse encounters a change in acoustic impedance, part of its energy is reflected back off of the interface. This reflected (upgoing) energy encounters a previous layer, and a portion of it is reflected back downward. Since it has now been reflected twice, its phase is the same as that of the original downgoing wave. In the presence of many layers, each of the multiple reflections will arrive slightly later in time than the original pulse. This has the effect of broadening the received arrival. The more layering, the more the energy is delayed, and the more the pulse is spread out in time. This smoothing and broadening of the

pulse tends to tilt the spectrum, shifting energy at higher frequencies to the lower end of the spectrum. In this sense, the effect of intrabed multiples appears to be frequency selective. While there is no energy loss from conversion to heat, the apparent attenuation from intrabed multiples is indistinguishable from other loss mechanisms, such as frictional or viscous losses, which attenuate higher frequencies more than lower ones. O'Doherty and Anstey [50], and Schoenberger and Levin [55, 56] show that intrabed multiples may account for as much as 1/3 to 1/2 of the total attenuation. Other references [54, 58, 59] also discuss this important phenomenon.

4.2.2 Intrinsic and effective attenuation

The previous section underscores the need for defining just what is being measured. Attenuation is often defined as the decay in wave amplitude caused by friction that results in an irreversible conversion of energy to heat. This is also referred to as "intrinsic attenuation." Other effects (scattering, intrabed multiples), which result in a re-distribution rather than a loss of energy also cause a decrease in wave amplitude. This type of loss is called "apparent attenuation." The loss due to both of these effects is called "effective attenuation." Although intrinsic attenuation is a more fundamental parameter, it is effective attenuation that is used in modeling sound propagation.

The combination of effects that make up effective attenuation complicates the spectrum. Intrinsic attenuation is primarily due to frictional losses and has a f^1 dependence. The effect of intrabed multiples is to tilt the spectrum, raising the lower end and decreasing the upper end. This tilt is not necessarily linear with frequency, so the spectrum of the combination may or may not show a linear dependence on frequency. Separation of intrinsic from effective attenuation is a research topic currently receiving attention [40, 43, 44].

4.2.3 Previous studies

Previously reported attenuation values [19] have been obtained from a variety of experiments. These include laboratory studies, in situ measurements made using probes in the upper two meters of sediment, and reflection and refraction experiments. Results from laboratory experiments give attenuation for frequencies in the KHz to MHz range. At the velocities of natural marine sediments (greater than 1500 m/s) wavelengths would be on the order of 15 meters at 100 Hz - very long for a laboratory experiment. Since small, homogeneous samples of sediment are used, these studies give a measure of intrinsic attenuation. Attenuation at high frequencies is found from reflection studies, but depths to as much as a kilometer are sampled, so effective attenuation is found. Refraction studies provide information about attenuation at low frequency. Large distances and vertically inhomogeneous sections of sediment are covered, so these studies measure effective attenuation. A summary of the types of studies is given in Table 4.1.

Attenuation Studies			
Type of Study	Frequencies Used ¹	Type of Attenuation Measured	Region of Sediment ²
in situ (probes)	high frequency	intrinsic	surface
reflection	high frequency	effective	shallow to moderately deep
refraction	low frequency	effective	moderately deep to deep

1 low frequency <300 Hz, high frequency >1 kHz

2 shallow <2 meters, deep >500 meters

Table 4.1 Attenuation studies.

Studies of attenuation generally yield attenuation as a function of frequency, or attenuation as a function of depth.

4.2.4 Attenuation as a function of frequency

Frictional losses are thought to be the dominant attenuative mechanism. Hamilton [19] has compiled data from a number of sources and concludes that k is approximately linearly dependent on frequency. An important factor which would result in a nonlinear dependence on frequency is the movement of pore water with respect to the mineral frame. Movement of the pore water results in viscous losses and velocity dispersion. Velocity dispersion would be largest in sands since permeability is high and there would be a higher amount of movement of pore water. In reviewing studies of dispersion in sands, Hamilton concluded that dispersion is negligible from a few KHz to 1 MHz in sands and less than 1 KHz to 2 MHz in silt-clays, although he points out that the tests were made over an order of magnitude of frequency or less, which may not be enough of a range to show dispersion. Recent reports suggest that a strict linear dependence on frequency is not correct [28, 62].

4.2.5 Attenuation as a function of depth

There is little experimental data on attenuation as a function of depth in the sediments. Hamilton [19] predicted an initial increase in attenuation to around 200 meters in depth followed by a decrease in attenuation with increasing depth. His prediction is based on two opposing effects: (1) *Attenuation increases as porosity decreases*. Porosity is defined as the volume of water-filled pore space per volume of sediment. As porosity decreases, sediment grains come into closer contact, which increases the number of intergranular contacts and the friction between them. This increase in friction causes an increase in attenuation. (2) *Attenuation is decreased as overburden pressure increases*. As

depth (pressure) increases, the sediment grains are forced together and begin to form a more rigid structure. There is less movement of the grains and thus less frictional loss. Attenuation therefore decreases with increasing overburden pressure.

Silt-clays are the dominant part of surficial sediments on deep sea fans. The porosity of these sediments is between 70 and 90%. There is a large initial decrease in porosity with increasing depth, and that effect dominates, causing an increase in attenuation. By 100 to 200 meters, there is little further reduction in porosity and the effect of increasing overburden pressure begins to dominate. Past this point, there is a decrease in attenuation with increasing depth. Hamilton reports a value for k at the surface between .05 to .1 $dB/(km \cdot Hz)$, followed by an increase to .2 $dB/(km \cdot Hz)$ at 100-200 meters, and a decrease in k past 200 meters. (Attenuation coefficient k is defined by equation A2.5a or A2.5c in Appendix A2. It has units of $dB/(meter \cdot kHz)$, or equivalently, $dB/(km \cdot Hz)$.)

Jacobson, Shor, and Dorman [30] offer a different explanation for the shape of the attenuation curve. They found a peak of attenuation at 600 meters, and feel that the observed peak is a consequence of sediment lithification. 600 meters is approximately the depth at which the unlithified sediment becomes a mudstone. The collapse of the cardhouse structure occurring at that depth increases intergranular contacts and aids in cementation of the mineral grains. This reduces sliding friction, which is the dominant mechanism for attenuation in the sediment.

They also point out that the decrease of k with increasing depth that Hamilton reports is more likely due to the units of k than to overburden pressure. The attenuation coefficient k gives a measure of the loss per distance. As the velocity increases with depth, there is a concomitant increase in the wavelength. The pathlength over one cycle therefore becomes longer and longer. A unit of length becomes a smaller and smaller portion of a wavelength, and k decreases. The quality factor Q^{-1} measures attenuation as loss per cycle, and is thus independent of frequency and velocity. For this reason, they feel Q^{-1} is preferable to k as a measure of attenuation.

4.2.6 Interpretation of results

The data that have been compiled appear to have a somewhat remarkable linear relationship over a wide range of frequencies [19, Fig. 1]. These results were obtained from different types of experiments as well as different geographical areas. A compilation of data from different regions and sediment types, and obtained using different techniques, must contain a large amount of scatter. Scatter results from the estimation of different quantities (intrinsic or effective), and because attenuation is depth dependent. Given the wide variety of sources for data, and the amount of scatter, inferences drawn from them need to be interpreted carefully.

4.3 Methods of estimating attenuation

Several methods have been used to estimate attenuation in a medium. These can be grouped into time domain and frequency domain methods. Frequency domain methods consider some aspect of the source and attenuated spectra. Time domain methods use a measure, such as the change in the peak amplitude of the waveform, to relate changes in the time series with attenuation. Without considering the frequency domain characteristics of the signals (source and received waveforms), time domain methods generally produce misleading or incorrect results. An example will show why this is so.

Consider a refraction experiment that uses two different sources. If the first source is broadband (an input spike, which has a flat spectrum, or an explosion, which has a relatively broadband spectrum), much of the energy in the signal is carried in the higher frequencies. Since high frequencies are highly attenuated, much of the high frequency energy will be lost and the waveform will appear to decay fairly rapidly. If a second source which produces a low frequency narrow-band signal is then used, the energy that was previously transmitted at higher frequencies is now carried at lower frequencies. In this case, since there is relatively low attenuation at the lower frequencies, the waveform will show less attenuation than when the broadband source was used. Although the acoustic energy travels the same distance through the same medium, the amplitude of the received waveform is different depending upon the source. This example shows that the frequency characteristics of the source must be considered in these types of experiments.

A method of spectral ratios is used in the present study. Spectral ratios are formed by dividing the spectrum of the refracted path by that of the direct path, thus taking the source (direct path) spectrum into account. Attenuation is proportional to the slope of the spectral ratio. The method is derived in Appendix A2.

4.4 Data

Figures 4.1a through 4.1d give examples of the spectral ratio data. The top plots in these figures are the hydrophone time series, the middle plots show the spectra of the two time series, and the bottom plots give the spectral ratios. A linear least squares fit to each spectral ratio is also shown. Spectral ratio slopes, needed in equation A2.13 (Appendix A2), are obtained from the least squares fits.

The effect of increasing path length can be seen in these figures. Each figure in the sequence presents data from a deeper ray, or equivalently, from a ray which has a longer path length. Arrivals which have longer path lengths suffer more attenuation, and the refracted spectra have substantially lower levels than their respective source spectra. The result is that spectral ratio slopes are steeper for arrivals that penetrate deeper in the sediment.

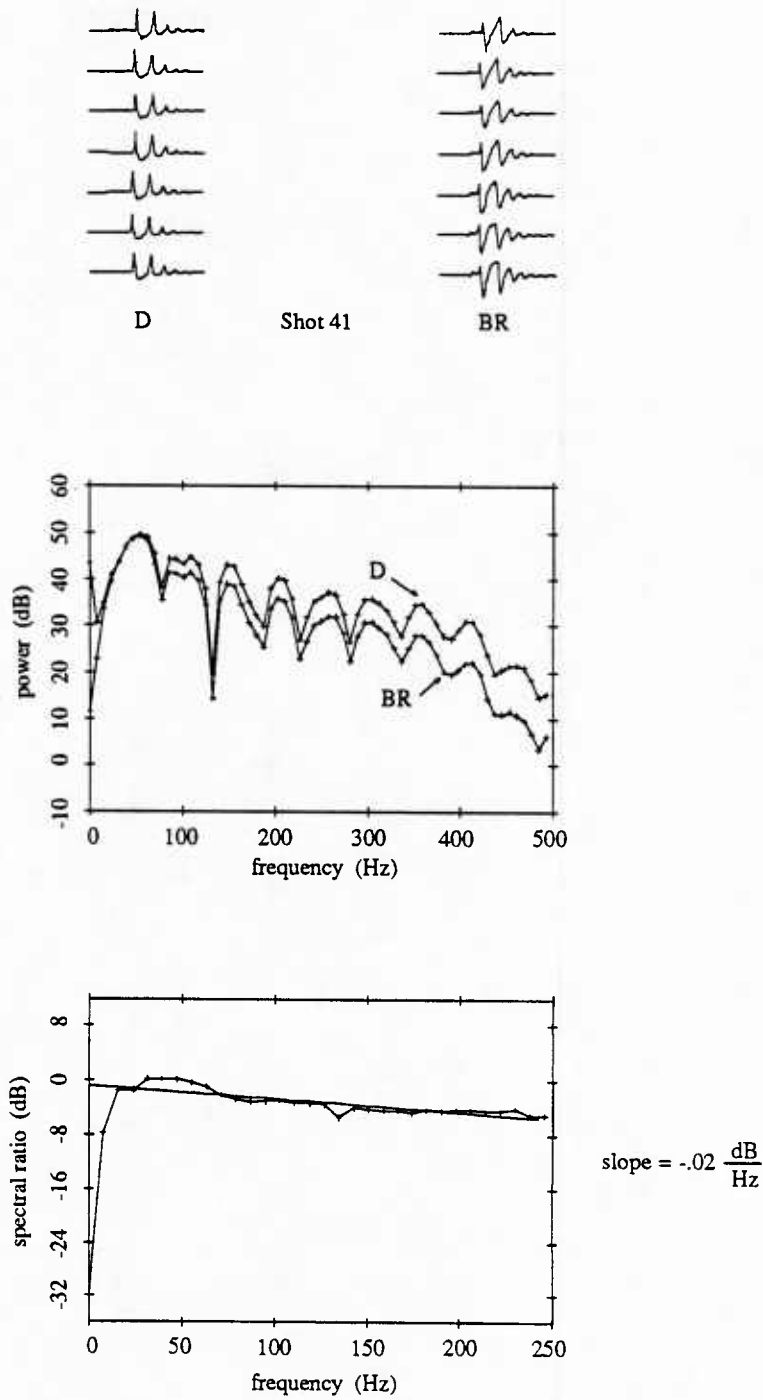


Figure 4.1a Spectral ratio data, Shot 41 BR.
 Time series at top are scaled to have same maximum amplitude.
 Data is from a shallow refraction (100 meters depth in sediment).

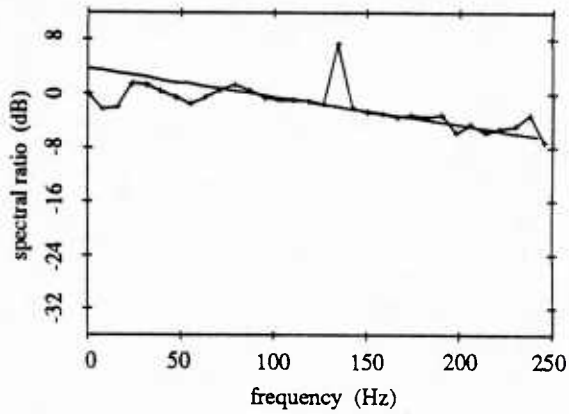
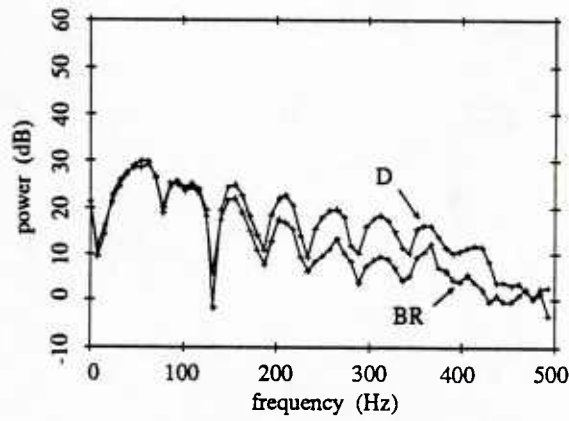
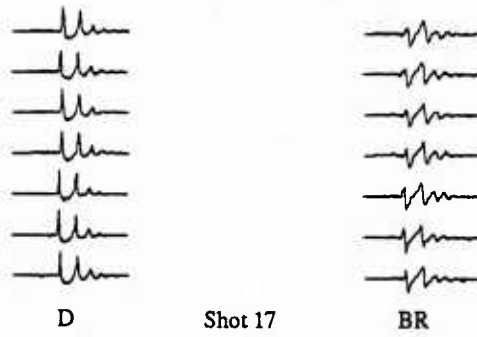


Figure 4.1b Spectral ratio data, Shot 17 BR.
Time series at top are scaled to have same maximum amplitude.
Data is from a moderately shallow refraction (133 meters depth in sediment).

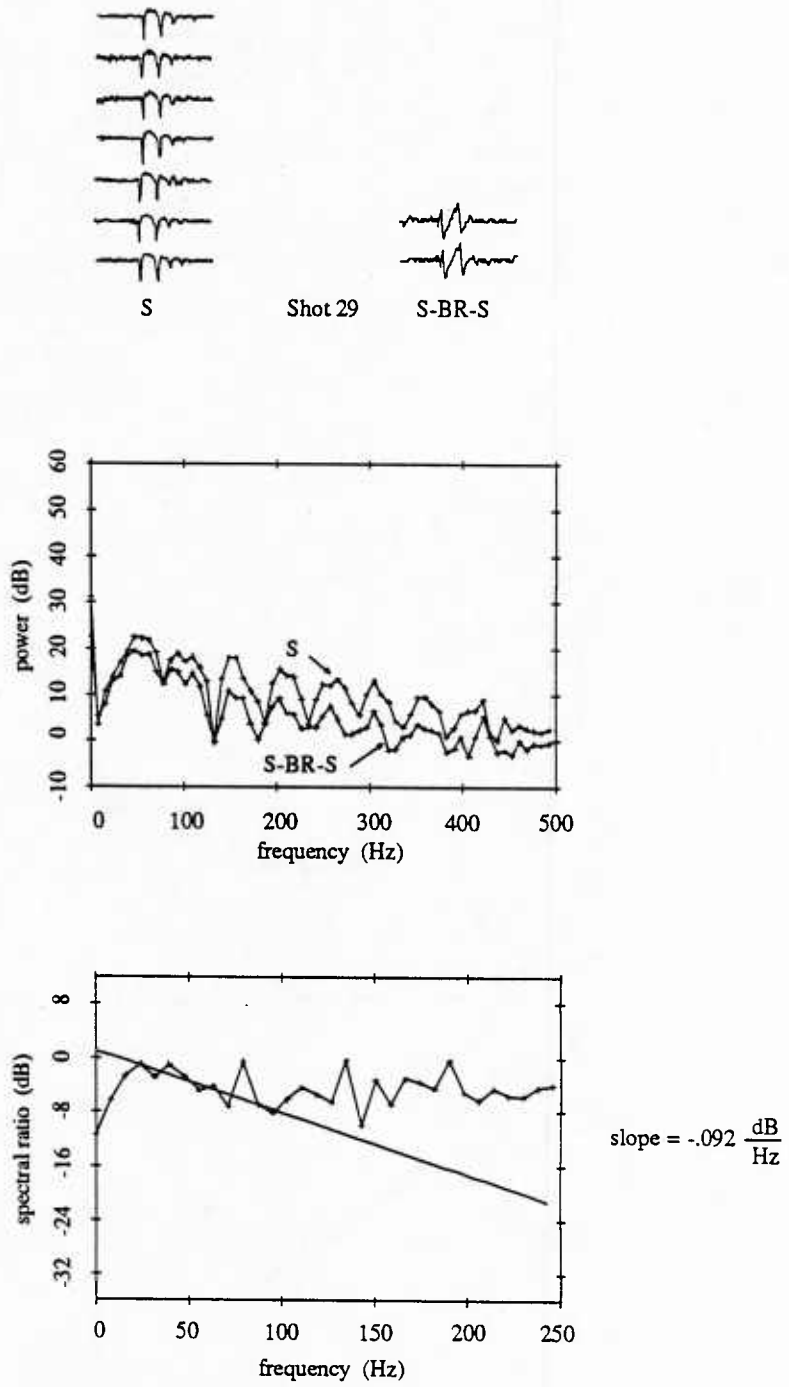


Figure 4.1c Spectral ratio data, Shot 29 S-BR-S.
 Time series at top are scaled to have same maximum amplitude.
 Data is from a medium-depth refraction (213 meters depth in sediment).

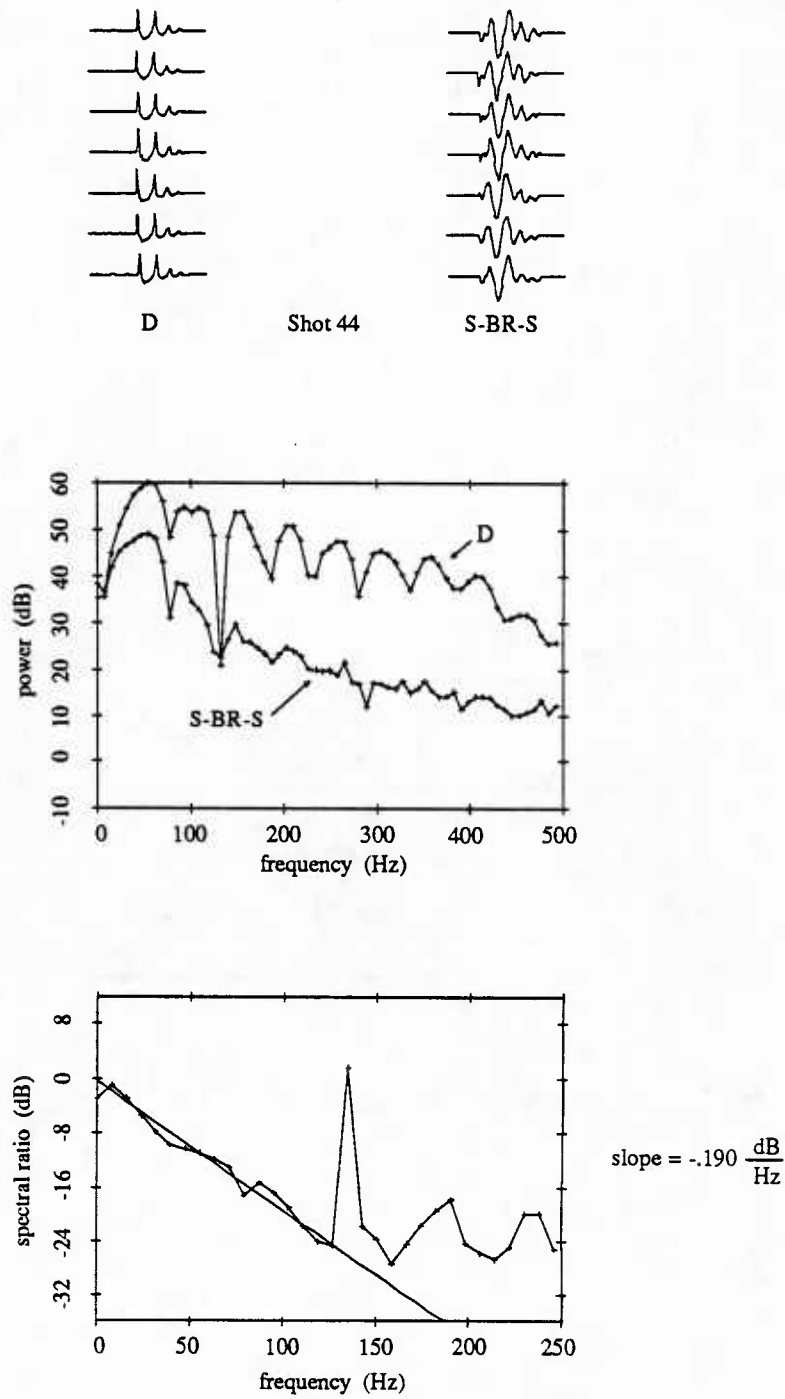


Figure 4.1d Spectral ratio data, Shot 44 S-BR-S.
 Time series at top are scaled to have same maximum amplitude.
 Data is from a deep refraction (470 meters depth in sediment).

Spectral ratio data						
Arrival	Floor Depth	Depth in Sediment	Path Length	Total Time	-slope of SR_k	-slope of SR_Q
17a br	2822	133	1510	.9760	.042194	.004858
19a br	2830	88	1216	.7971	.029922	.003445
19b brs	2835	455	2876	1.6553	.156992	.018074
21b brs	2850	246	1912	1.1887	.076800	.008842
23b brs	2860	191	1682	1.0667	.028160	.003242
23b sbrs	2833	516	3186	1.7896	.203408	.023418
25a sbr	2820	165	1578	1.0106	.099072	.011406
25a brs	2875	145	1547	.9970	.065424	.007532
25b sbrs	2843	323	2196	1.3279	.130222	.014992
27a sbr	2823	126	1466	.9498	.056320	.006484
27a brs	2887	115	1394	.9066	.044800	.005158
29a sbrs	2856	213	1772	1.1152	.091622	.010548
31a sbrs	2862	186	1661	1.0554	.054918	.006323
33a sbrs	2865	169	1595	1.0195	.055712	.006414
36a br	2848	47	877	.5829	.026532	.003055
36a sbr	2817	202	1725	1.0903	.026338	.003032
36a brs	2863	181	1641	1.0445	.033556	.003863
36a sbrs	2835	470	2951	1.6904	.163328	.018804
40a br	2821	154	1546	.9939	.024320	.002800
41a br	2827	100	1297	.8471	.020000	.002303
41a brs	2830	622	3611	1.9807	.196820	.022660
43a sbr	2814	272	2014	1.2406	.040872	.004706
43a brs	2851	233	1859	1.1612	.092058	.010599
44a sbr	2816	207	1748	1.1026	.045708	.005262
44a brs	2861	184	1651	1.0499	.055792	.006423
44a sbrs	2835	470	2951	1.6904	.190280	.021907
45a br	2850	43	842	.5605	.018530	.002133
45a sbr	2819	174	1612	1.0290	.035788	.004120
45a brs	2868	158	1557	.9994	.039040	.00495
46a brs	2875	141	1554	1.0024	.025600	.002947
47a sbr	2823	122	1437	.9324	.027686	.003187
47a brs	2885	115	1394	.9066	.018022	.002075
47a sbrs	2850	265	1995	1.2315	.076800	.008842
48a sbrs	2855	218	1796	1.1280	.051200	.005895

Table 4.2 Spectral ratio data. Floor depth is the depth at which the ray intersects the sea floor. Path length is total path length in the sediment. SR_k refers to the definition of the spectral ratio given in equation A2.6. SR_Q refers to the definition of the spectral ratio given in equation A2.9.

Figure 4.1a is data from a ray which penetrated to a depth of 100 meters and had a path length of 1297 meters. In Figure 4.1b the ray turned at a depth of 133 meters and had a path length of 1510 meters. The increase in path length of 213 meters has doubled the spectral ratio slope. Figure 4.1d is data from a ray which had a depth of 470 meters and a path length of 2951 meters. The spectral ratio slope is nearly ten times that of the slope in Figure 4.1a. In general, spectral ratios of shallow refractions have a linear region at higher frequencies, and are linear over a larger frequency interval, than highly attenuated deeper refractions. Deep refractions lose most of their high frequency energy and show linearity over smaller intervals since the signal at high frequencies is down in the noise floor, and the spectrum flattens out. Spectral ratio slopes (δSR) along with the total time and path length for each ray are given in Table 4.2.

The spectra used to calculate the spectral ratios are found by separating individual arrivals from the time series using a rectangular window. A fast Fourier transform (FFT) of each channel for a particular ray type (i.e. D, BR, etc.) is calculated, and the spectra are incoherently averaged (magnitude squared). The square root of the average is then taken to obtain the magnitude spectrum.

The seven good channels from the low gain half of the array are used when possible. In many instances the BR-S and S-BR arrivals cross in time and only two or three of the channels can be used. For example, in Figure 2.5c, these two arrivals converge near hydrophone 11. There is complete overlap by hydrophone 8 (not shown in this figure) and the arrivals separate again lower in the array. In these cases, only channels in which arrivals are separated in time are used. As shot range increases, the direct (D) and BR paths run together. When these two arrivals begin to overlap, the surface reflected path (S) is used to find the source spectrum.

Solutions presented in Figure 4.2			
Figure	number of layers	eigenvectors retained	SSR $\times 10^{-4}$
4.2a	3	3	1.85
4.2b	4	4	1.61
4.2c	7	5	1.53
4.2d	13	5	2.09
4.2e	13	7	1.60

Table 4.3 Solutions presented in Figure 4.2.

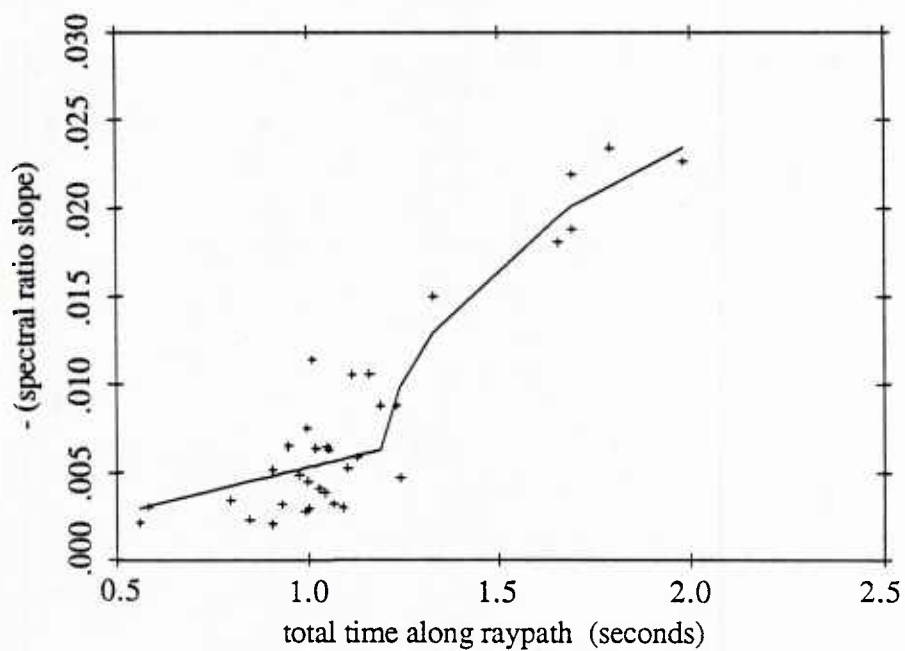
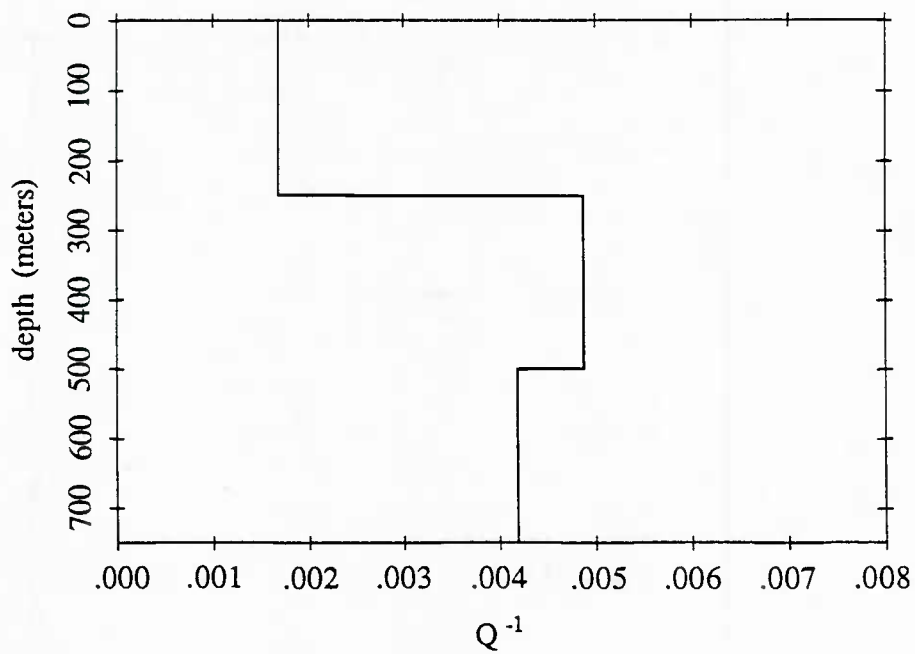


Figure 4.2a Attenuation profile: 3 layer model, 3 eigenvectors retained. A theoretical curve generated from the attenuation profile is plotted along with the experimental data.

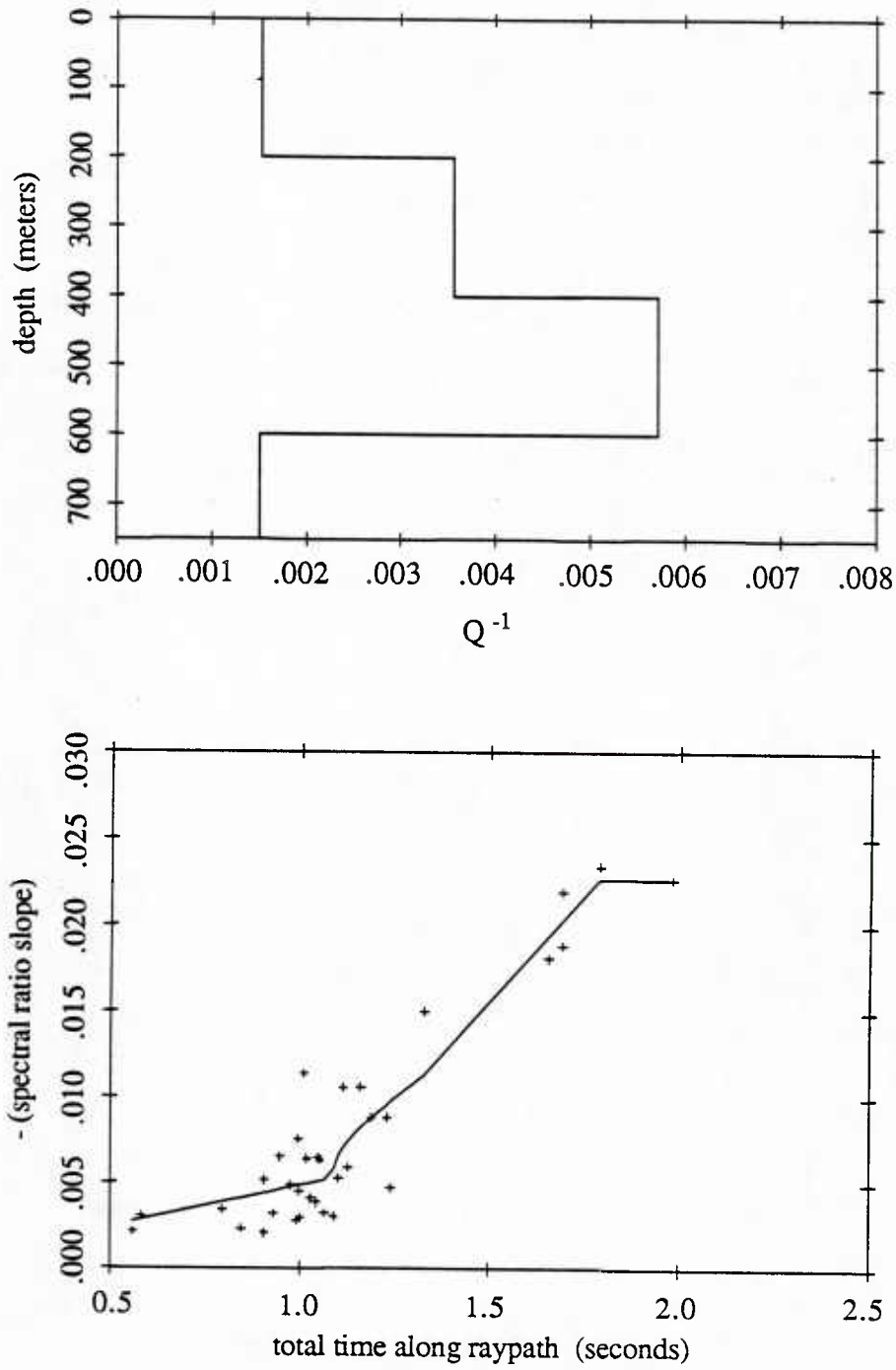


Figure 4.2b Attenuation profile: 4 layer model, 4 eigenvectors retained. A theoretical curve generated from the attenuation profile is plotted along with the experimental data.

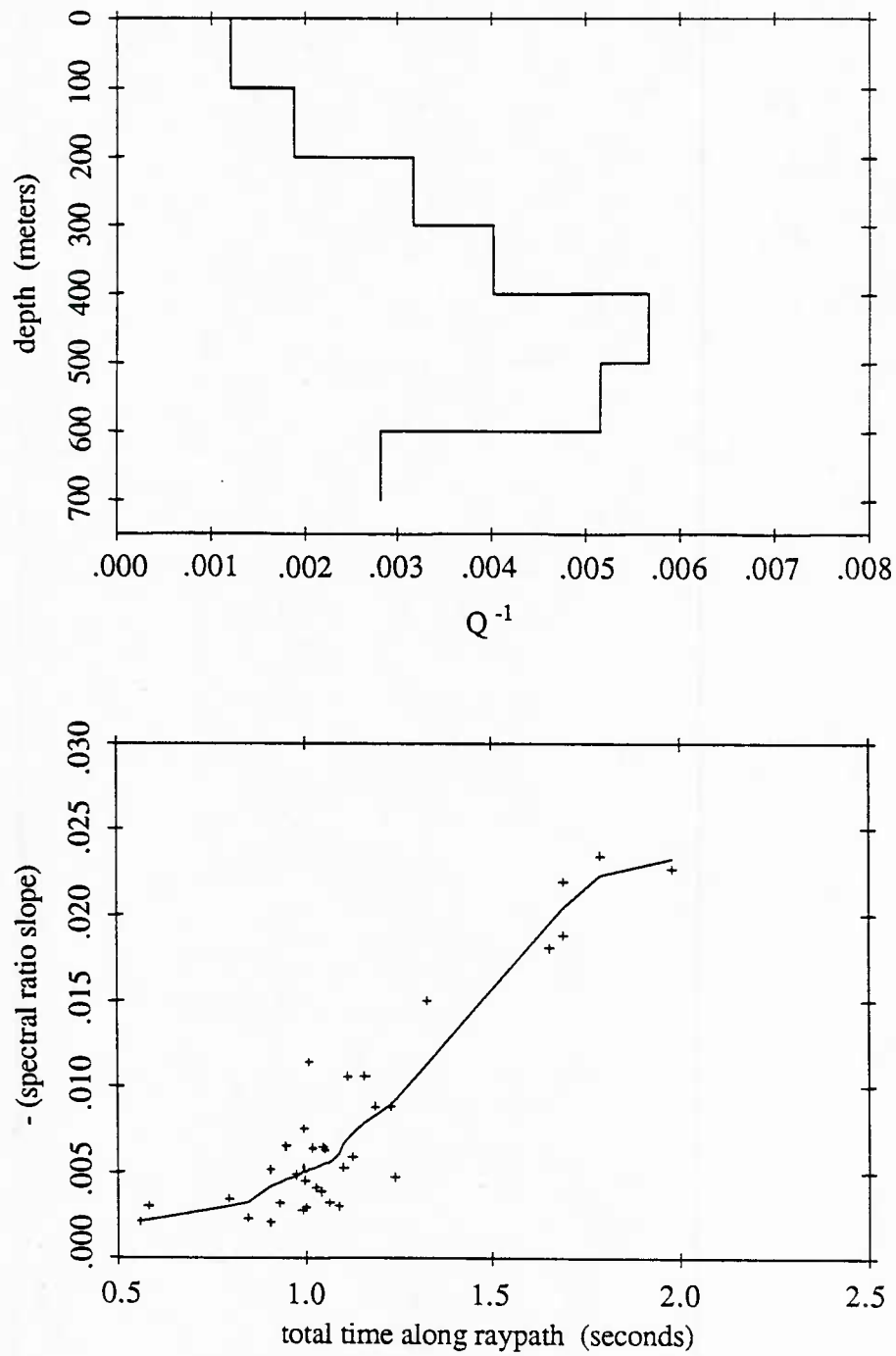


Figure 4.2c Attenuation profile: 7 layer model, 5 eigenvectors retained. A theoretical curve generated from the attenuation profile is plotted along with the experimental data.

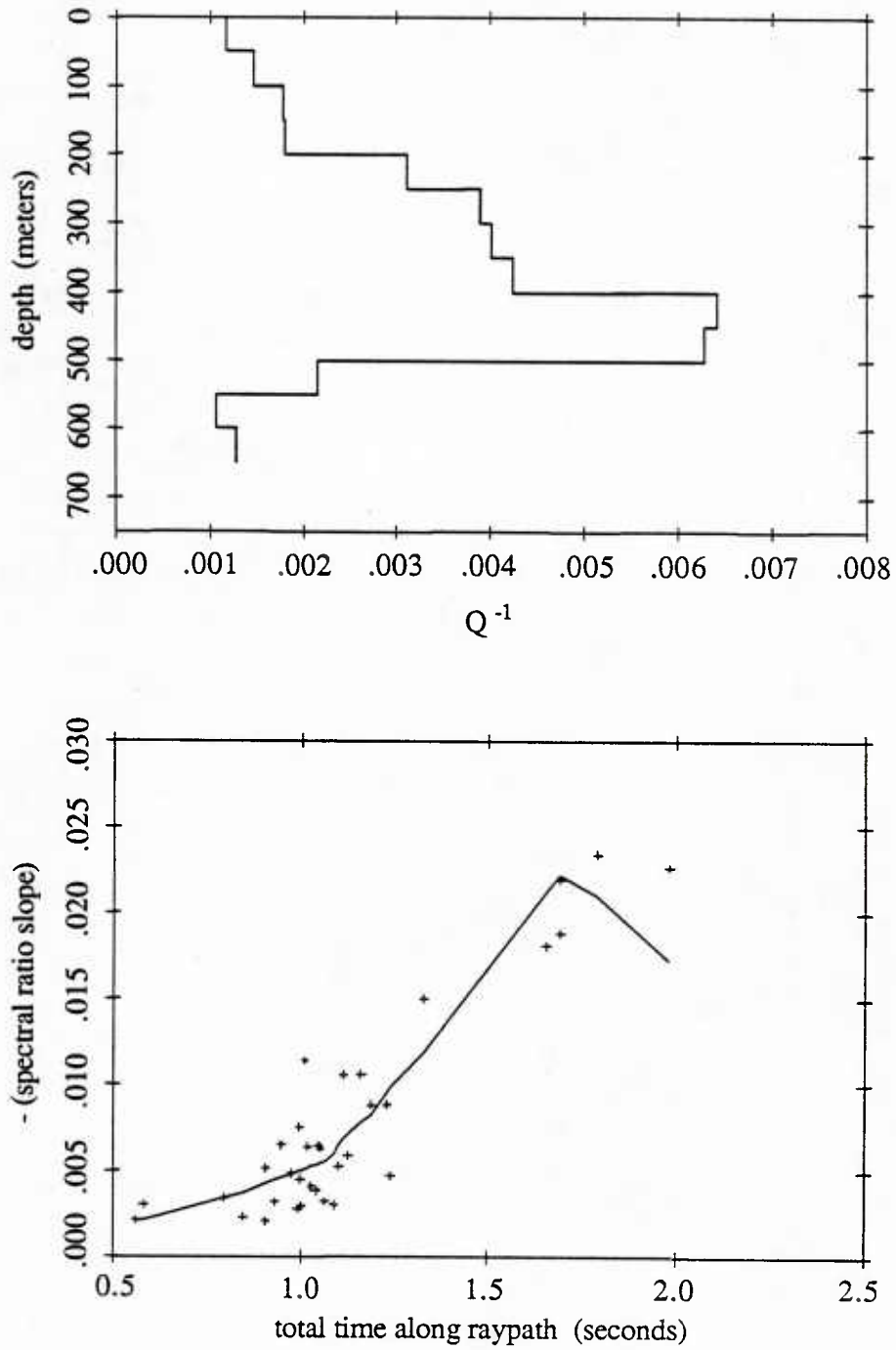


Figure 4.2d Attenuation profile: 13 layer model, 5 eigenvectors retained. A theoretical curve generated from the attenuation profile is plotted along with the experimental data.

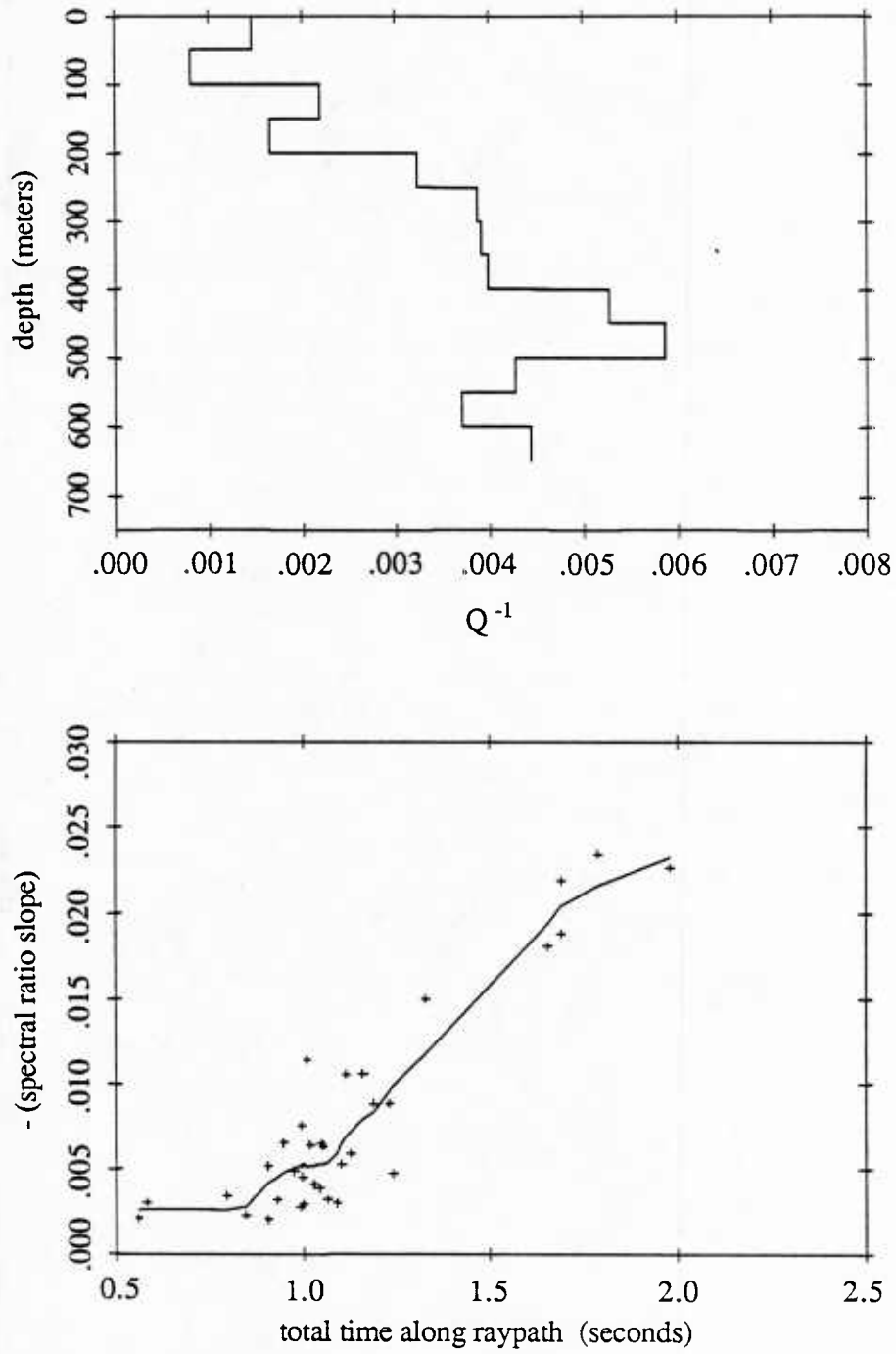


Figure 4.2e Attenuation profile: 13 layer model, 7 eigenvectors retained. A theoretical curve generated from the attenuation profile is plotted along with the experimental data.

4.5 Results

The spectral ratio slopes from Table 4.2 were used in equation A2.13 and inverted using a singular value decomposition (SVD) [15, 39, 41, 66]. Four models, with 3, 4, 7, and 13 layers are presented, and are summarized in Table 4.3. Results are illustrated in Figures 4.2a through 4.2e. The top plot in these figures gives Q^{-1} as a function of depth in the sediment. In the bottom plot, a theoretical curve (solid line) generated from equation A2.15 is compared with the experimental data.

The 3 and 4 layer models had well conditioned matrices and all eigenvectors were incorporated into the solution. Solutions became unstable, producing negative attenuation coefficients, when all eigenvectors for the 7 layer model and more than 8 eigenvectors for the 13 layer model were included in the solution. The sum of squared residuals ($SSR = \sum(\delta SR_i - \delta SR_i)^2$) gives an indication of the quality of fit. The 7 layer model (Figure 4.2c) has the lowest SSR (last column in Table 4.3), suggesting that we are able to obtain better resolution than is given by a 3 or 4 layer model. Beyond this, however, the values increase because of data resolution problems. This effect is seen in the 13 layer model. Retaining 5 eigenvectors produces a smooth attenuation profile, but does not adequately represent the data (Figure 4.2d). Retaining 8 eigenvectors results in a better fit to the experimental data, but produces an attenuation profile with a large amount of variance (Figure 4.2e).

In selecting a solution, we can reject the 3 layer model in favor of the 4 layer model based on an F-test. Although the sum of squared residuals (SSR) is less for the 7 layer model than for the 4 layer model, there are fewer degrees of freedom; the reduction in SSR is not large enough to warrant rejection of the 4 layer model using an F-test. The 4 layer model along with 90% confidence bounds (bold lines) is shown in Figure 4.3.

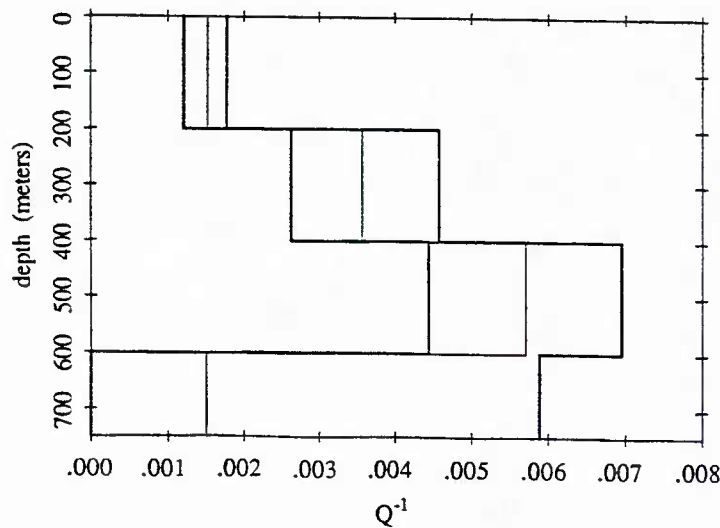


Figure 4.3 Four layer attenuation model with 90% confidence bounds. Model is given by the light line, confidence bounds are given by bold lines.

Although the 4 layer model cannot be rejected in favor of the 7 layer model, this does not mean that the 7 layer model must be rejected. It can be shown (also by use of an F-test) that the variances of these two models are not significantly different. The 7 layer model is somewhat more appealing, as it provides better resolution while still yielding a smooth solution. For these reasons, both the 4 and 7 layer solutions are considered acceptable. Details of these two solutions are given in Tables 4.4 and 4.5.

Attenuation profile - 4 layer model		
Depth (meters)	k (dB/m/kHz)	Q^{-1} (nepers/radian)
0-200	.027	.0015
200-400	.057	.0036
400-600	.081	.0057
600-800	.018	.0015

Table 4.4 Attenuation profile for a 4 layer model
Attenuation profile shown in Figure 4.2b (4 eigenvectors retained).

Attenuation profile - 7 layer model		
Depth (meters)	k (dB/m/kHz)	Q^{-1} (nepers/radian)
0-100	.022	.0012
100-200	.033	.0019
200-300	.052	.0032
300-400	.057	.0040
400-500	.085	.0057
500-600	.071	.0052
600-700	.040	.0028

Table 4.5 Attenuation profile for a 7 layer model
Attenuation profile shown in Figure 4.2c (5 eigenvectors retained).

4.6 Discussion

The most notable feature in all solutions is an attenuation peak at about 400-500 meters depth. Hamilton predicted an attenuation peak due to the opposing effects of porosity reduction and the increase in overburden

pressure as depth increases, while Jacobson, Shor, and Dorman [30], and Jacobson, Shor, and Bee [29] felt that the peak they found was a result of sediment lithification (see the discussion in Section 4.2.5). Without a deep core, it is difficult to know which of the two effects is responsible.

The relationship between the attenuation profile and the velocity gradient is shown in Figure 4.4. A four layer velocity profile for the sediment was presented in Table 3.8. The gradients from this result are plotted along with the attenuation profile for a four layer model. In this figure, it is seen that there are peaks in both the velocity gradient and attenuation profiles. Possible causes for a peak in the velocity gradient have been discussed in Section 3.8. The velocity gradient and attenuation are affected similarly by physical changes occurring in the sediment; the discussion in that section also applies to the attenuation profile. A difference between these two profiles is that the attenuation peaks at a greater depth than the velocity gradient. The attenuation peak also occurs below the velocity gradient peak in Jacobson, Shor, and Dorman [30, Figs. 4 and 9], and in Jacobson, Shor, and Bee [29, Figs. 9 and 16].

Changes in velocity and attenuation in the upper sediments (before lithification begins) are primarily due to changes in porosity [19, 22]. The high porosity (70-90%) silts and clays present at the surface of deep sea fans are rapidly reduced with increasing depth in the sediment. The largest amount of reduction in porosity is thought to occur by 200-300 meters [19, 20].

Velocity increases monotonically as porosity decreases [25, Fig. 6]. As the rate of change in porosity begins to slow, the velocity gradients would begin to approach a constant. In the data presented in Figure 4.4 this occurs around 400 meters.

Attenuation is not a monotonic function of porosity [19, Fig. 2]. Attenuation increases as porosity decreases, reaching a peak between 50-55%. As porosity decreases below 50%, attenuation decreases. If the porosity were still greater than 55 or 60 % at 400 meters, then a further reduction in porosity (as depth increases) would result in an increase in attenuation. If changes in porosity were the only effect, then a peak in the velocity gradient gives an indication of where the most rapid reduction in porosity occurs; the attenuation peak would indicate the depth where porosity values are around 50% (or the place where effects of overburden pressure counterbalance the reduction in porosity). Other factors are most likely present, with lithification, no doubt, playing an important role. As sediments lithify, the mineral frame becomes rigid, and the attenuation and velocity gradient will approach a constant value.

Finally, in Figures 4.5 and 4.6, the results of this study are added to the attenuation data compiled by Hamilton [19]. Attenuation data as a function of frequency in Figure 4.5 is plotted as a band of values. This band corresponds to the smallest and largest values found (Table 4.5). Attenuation as a function of depth is shown in Figure 4.6.

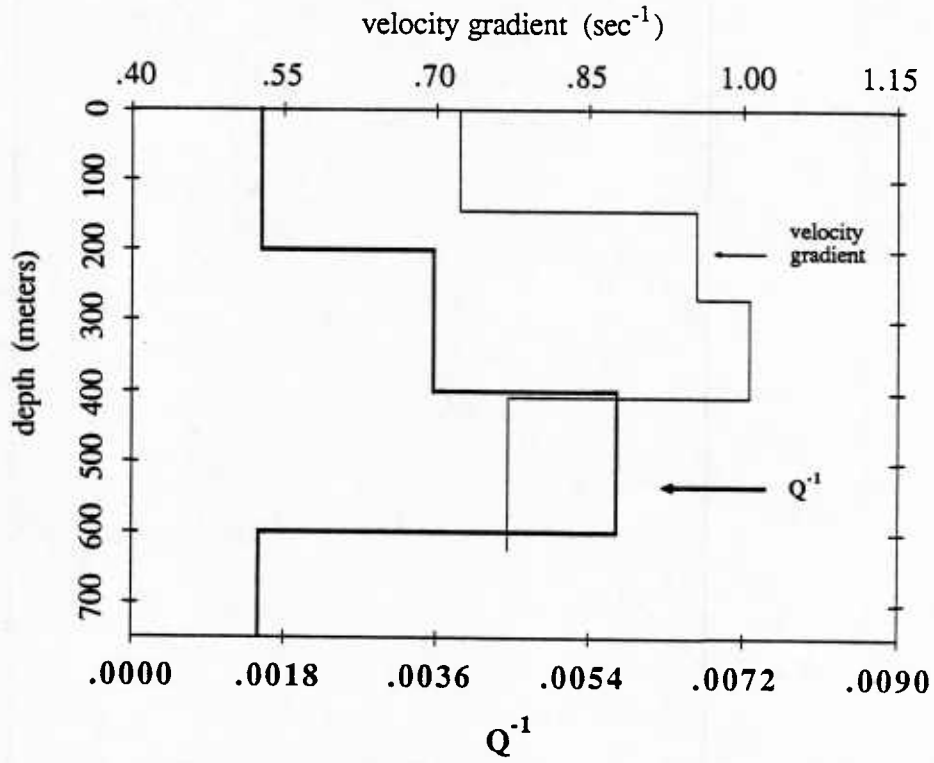


Figure 4.4 Relationship between the velocity gradient and 1/Q as a function of depth.

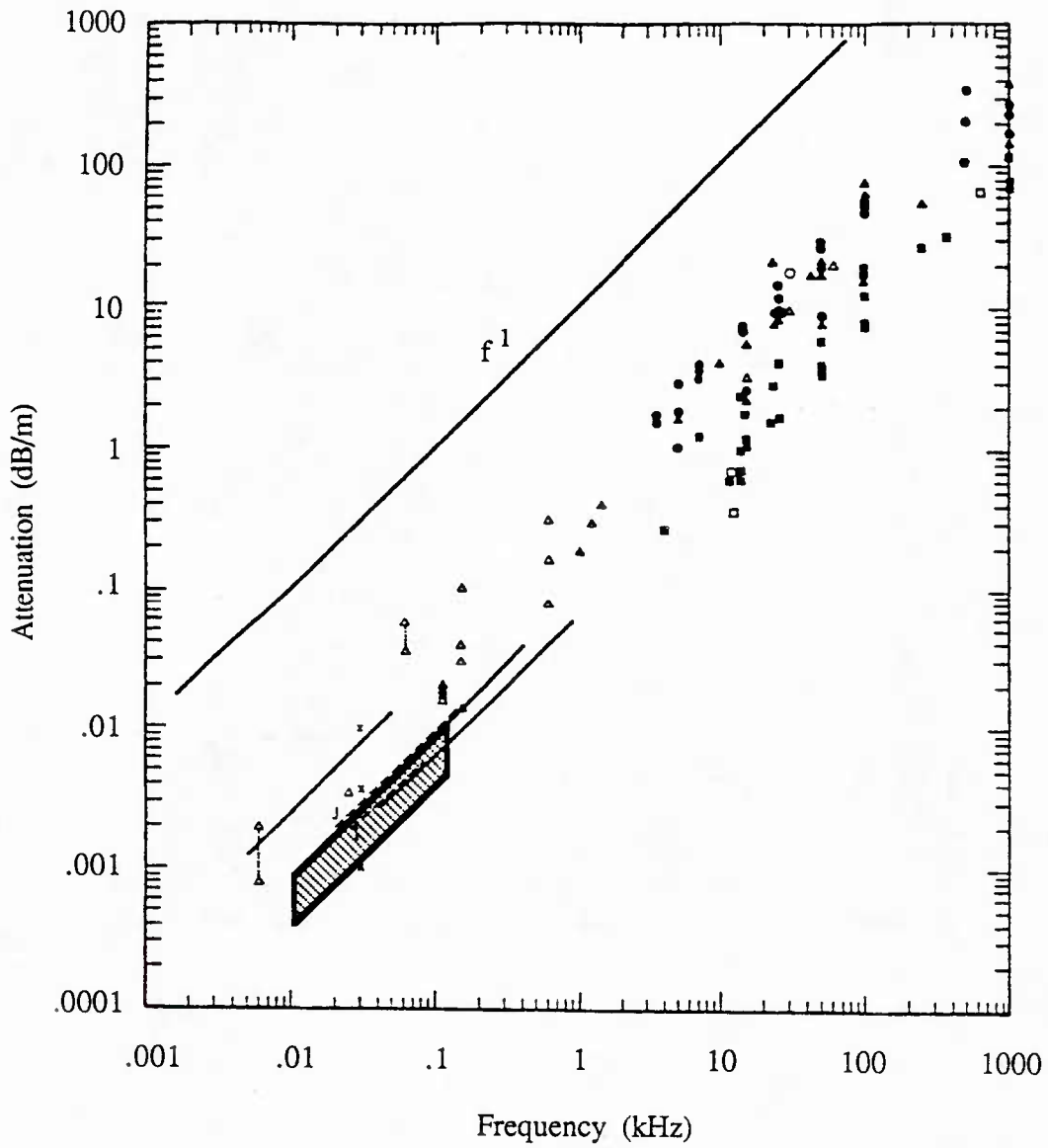


Figure 4.5 Attenuation as a function of frequency.
Shaded rectangle shows results of this study.
(Reprinted from reference [19])

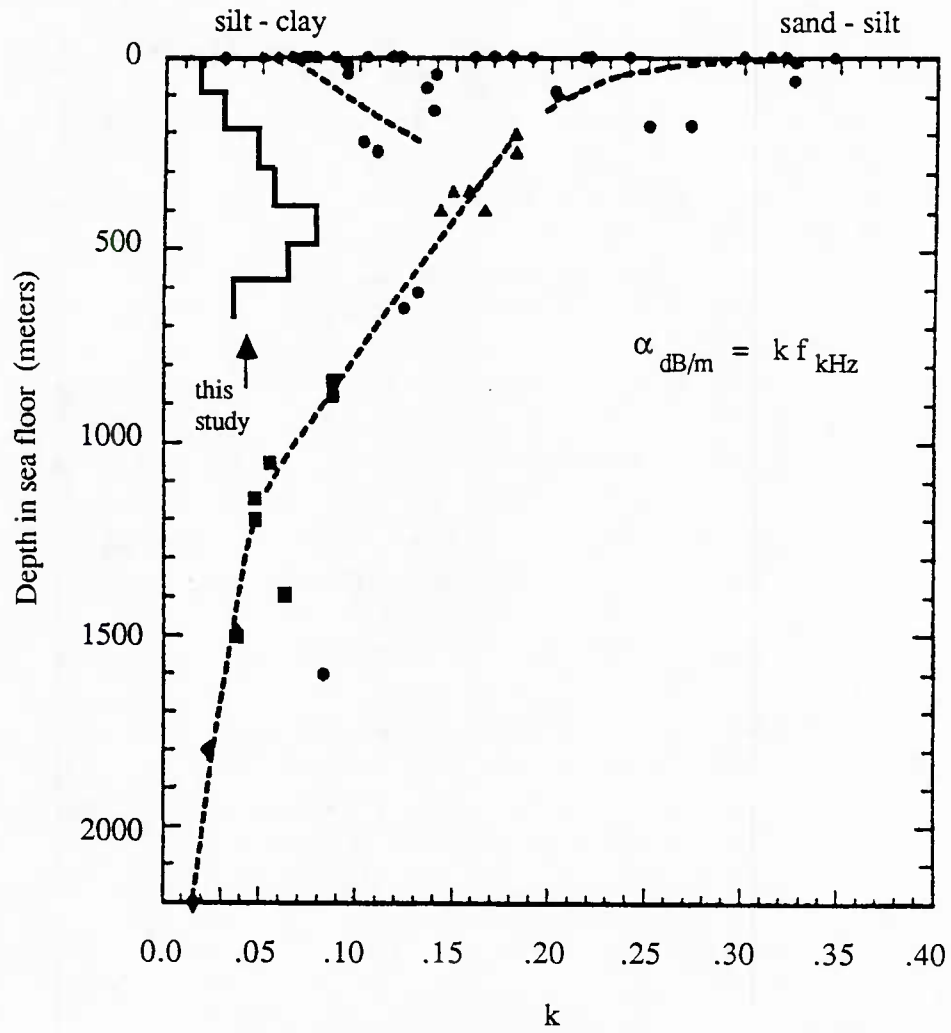


Figure 4.6 Attenuation as a function of depth.
(Reprinted from reference [19])

References

- [1] Aki, K., Richards, P.G., *Quantitative Seismology: Theory and Methods*, Volume II, W.H. Freeman and Company, San Francisco (1980).
- [2] Bachman, R.T., "Acoustic and physical property relationships in marine sediment", *J. Acoust. Soc. Am.* 78(2), 616-621 (1985).
- [3] Bendat, J.S., Piersol, A.G., *Random Data: Analysis and Measurement Procedures*, Wiley, New York (1986).
- [4] Bee, M., Jacobson, R.S., "Linear inversion of body-wave data - Part III Model parameterization", *Geophysics* 49(12), 2088-2093 (1984).
- [5] Chapman, N.R., "Measurement of the waveform parameters of shallow explosive charges", *J. Acoust. Soc. Am.* 78(2), 672-681 (1985).
- [6] Chapman, N.R., Levy, S., Stinson, K., Jones, I.F., Prager, B.T., Oldenburg, D.W., "Inversion of sound-speed and density profiles in deep ocean sediments", *J. Acoust. Soc. Am.* 79(5), 1441-1456 (1986).
- [7] Christensen, R.E., Frank, J.A., Geddes, W.H., "Low-frequency propagation via shallow refracted paths through deep ocean unconsolidated sediments", *J. Acoust. Soc. Am.* 57(6), 1421-1426 (1975).
- [8] Clay, C.S., Medwin, H., *Acoustical Oceanography*, Wiley, New York (1977).
- [9] Dorman, L.M., "A linear relationship between earth models and seismic body wave data", *Geophys. Res. Lett.* 6(3), 132-134 (1979).
- [10] Dorman, L.M., "Modelling and parameterization errors in body wave seismology", *Geophys. J. R. astr. Soc.* 72, 571-576 (1983).
- [11] Dorman, L.M., Jacobson, R.S., "Linear inversion of body wave data - Part I: Velocity structure from traveltimes and ranges", *Geophysics* 46, 138-151 (1981).
- [12] Fry, J.C., Raitt, R.W., "Sound Velocities at the Surface of Deep Sea Sediments", *J. Geophys. Res.* 66(2), 589-597 (1961).
- [13] Ganley, D.C., Kanasewich, E.R., "Measurement of Absorption and Dispersion From Check Shot Surveys", *J. Geophys. Res.* 85(B10), 5219-5226 (1980).
- [14] Garmany, J., Orcutt, J.A., Parker, R.L., "Travel Time Inversion: A Geometrical Approach", *J. Geophys. Res.* 84(B7), 3615-3622 (1979).
- [15] Golub, G.H., Reinsch, C., "Singular Value Decomposition and Least Squares Solutions", in *Handbook for Automatic Computation II, Linear Algebra*, Wilkinson, J.H. and Reinsch, C (eds.), Springer-Verlag, New York, 134-151 (1971).
- [16] Hamilton, E.L., "Sound Velocity and Related Properties of Marine Sediments, North Pacific", *J. Geophys. Res.* 75(23), 4423-4446 (1970).

- [17] Hamilton, E.L., "Prediction of in-situ acoustic and elastic properties of marine sediments", *Geophysics* 36(2), 266-284 (1971).
- [18] Hamilton, E.L., "Compressional-wave attenuation in marine sediments", *Geophysics* 37(4), 620-646 (1972).
- [19] Hamilton, E.L., "Sound attenuation as a function of depth in the sea floor", *J. Acoust. Soc. Am.* 59(3), 528-535 (1976).
- [20] Hamilton, E.L., "Variations of density and porosity with depth in deep-sea sediments", *J. of Sedimentary Petrology* 46(2), 280-300 (1976).
- [21] Hamilton, E.L., "Sound velocity-density relations in sea-floor sediments and rocks", *J. Acoust. Soc. Am.* 63(2), 366-377 (1978).
- [22] Hamilton, E.L., "Sound velocity gradients in marine sediments", *J. Acoust. Soc. Am.* 65(4), 909-922 (1979).
- [23] Hamilton, E.L., "Geoacoustic modeling of the sea floor", *J. Acoust. Soc. Am.* 68(5), 1313-1340 (1980).
- [24] Hamilton, E.L., "Sound velocity as a function of depth in marine sediments", *J. Acoust. Soc. Am.* 78(4), 1348-1355 (1985).
- [25] Hamilton, E.L., Bachman, R.T., "Sound velocity and related properties of marine sediments", *J. Acoust. Soc. Am.* 72(6), 1891-1904 (1982).
- [26] Hamilton, E.L., Moore, D.G., Buffington, E.C., Sherrer, P.L., "Sediment velocities from sonobuoys: Bay of Bengal, Bering Sea, Japan Sea, and North Pacific", *J. Geophys. Res.* 79(17), 2653-2668 (1974).
- [27] Hess, G.R., Normark, W.R., "Holocene sedimentation history of the major fan valleys of Monterey fan", *Marine Geology* 22, 233-251 (1976).
- [28] Jacobson, R.S., "An investigation into the fundamental relationships between attenuation, phase dispersion, and frequency using seismic refraction profiles over sedimentary structures", *Geophysics* 52(1), 72-87 (1987).
- [29] Jacobson, R.S., Shor, G.G., Jr., Bee, M., "A comparison of velocity and attenuation between the Nicobar and Bengal deep sea fans", *J. Geophys. Res.* 89(B7), 6181-6196 (1984).
- [30] Jacobson, R.S., Shor, G.G., Jr., Dorman, L.M., "Linear inversion of body wave data - Part II: Attenuation versus depth using spectral ratios", *Geophysics* 46(2), 152-162 (1981).
- [31] Johnston, D.H., Toksoz, M.N., *Seismic Wave Attenuation*, Chapter 1: Definitions and Terminology, *Geophysics reprint series, No. 2*, Society of Exploration Geophysicists, 1-5 (1981).
- [32] Jones, T.D., "Pore fluids and frequency-dependent wave propagation in rocks", *Geophysics*, 51(10), 1939-1953 (1986).
- [33] Kanamori, H., Anderson, D.L., "Importance of Physical Dispersion in Surface Wave and Free Oscillation Problems: Review", *Rev. Geophys. Space Physics* 15(1), 105-112 (1977).

- [34] Kennett, B.L.N., "A Comparison of Travel-Time Inversions", *Geophys. J. R. Astr. Soc.* 44, 517-536 (1976).
- [35] Kennett, B.L.N, Orcutt, J.A., "A Comparison of Travel Time Inversions for Marine Refraction Profiles", *J. Geophys. Res.* 81(23), 4061-4070 (1976).
- [36] Kibblewhite, A.C., Hampton, L.D., "A review of deep ocean sound attenuation at very low frequencies", *J. Acoust. Soc. Am.* 67(1), 147-157 (1980).
- [37] Kjartansson, E., "Constant Q-Wave Propagation and Attenuation", *J. Geophys. Res.* 84(B9), 4737-4748 (1979).
- [38] Lavergne, M., "Emission by underwater explosions", *Geophysics* 35(3), 419-435 (1970).
- [39] Lawson, C.L., Hanson, R.J., *Solving least squares problems*, Prentice-Hall, New Jersey (1974).
- [40] Lerche, I., Menke, W., "An inversion method for separating apparent and intrinsic attenuation in layered media", *Geophys. J. R. Astr. Soc.* 87, 333-347 (1986).
- [41] Lines, L.R., Treitel, S., "Tutorial: A review of least-squares inversion and its application to geophysical problems", *Geophys. Prospect.* 32, 159-186 (1984).
- [42] McCann, C., McCann, D.M., "The attenuation of compressional waves in marine sediments", *Geophysics* 34(6), 882-892 (1969).
- [43] Menke, W., "A formula for the apparent attenuation of acoustic waves in randomly layered media", *Geophys. J. Royal Astr. Soc.* 75, 541-544 (1983).
- [44] Menke, W., Dubendorff, B., "Discriminating intrinsic and apparent attenuation in layered rock", *Geophysical Research Letters* 12(10), 721-724 (1985).
- [45] Mitchell, S.K, Focke, K.C., "New measurements of compressional wave attenuation in deep ocean sediments", *J. Acoust. Soc. Am.* 67(5), 1582-1589 (1980).
- [46] Mitchell, S.K., Lemmon, J.J., "A ray theory model of acoustic interaction with the ocean bottom", *J. Acoust. Soc. Am.* 66(3), 855-861 (1979).
- [47] Normark, W.R., "Channel piracy on Monterey Deep-Sea Fan", *Deep-Sea Research* 17, 837-846 (1970).
- [48] Normark, W.R., Gutmacher, T.E., Chase, T.E., Wilde, P., "Monterey Fan, Pacific Ocean", Chapter 13 in *Submarine Fans and Related Turbidite Systems*, Bouma, A.H., Normark, W.R. and Barnes, N.E. (eds.), Springer-Verlag, New York, 79-86, (1985).
- [49] Normark, W.R., Hess, G.R., Stow, D.A.V., Bowen, A.J., "Sediment waves on the Monterey fan levee: A preliminary physical interpretation", *Marine Geology* 37, 1-18 (1980).
- [50] O'Doherty, R.F., Anstey, N.A., "Reflections on amplitudes", *Geophys. Prosp.* 19, 430-458 (1971).

- [51] Orcutt, J.A., "Joint linear, extremal inversion of seismic kinematic data", *J. Geophys. Res.* 85(B5), 2649-2660 (1980).
- [52] Orcutt, J.A., Dorman, L.M., Spudich, P.K.P., "Inversion of seismic refraction data", in *The Earth's Crust*, Geophys. Monograph vol. 20, J.G. Heacock (ed.), 371-384, AGU, Washington, D.C. (1977).
- [53] Orcutt, J.A., MacKenzie, K., McClain, J., "The role of $X(p)$ constraints in linear, extremal inversion of explosion profile data", *Bull. Seism. Soc. Am.* 70(6) 2103-2116 (1980).
- [54] Richards, P.G., Menke, W., "The apparent attenuation of a scattering medium", *Bull. Seism. Soc. Am.* 73(4), 1005-1021 (1983).
- [55] Schoenberger, M., Levin, F.K., "Apparent attenuation due to intrabed multiples", *Geophysics* 39(3), 278-291 (1974).
- [56] Schoenberger, M., Levin, F.K., "Apparent attenuation due to intrabed multiples, II", *Geophysics* 43(4), 730-737 (1978).
- [57] Sorenson, H.W., *Parameter Estimation*, Marcel Dekker, New York (1980).
- [58] Spencer, T.W., Edwards, C.M., Sonnad, J.R., "Seismic wave attenuation in nonresolvable cyclic stratification", *Geophysics* 42(5), 939-949 (1977).
- [59] Spencer, T.W., Sonnad, J.R., Butler, T.M., "Seismic Q - Stratigraphy or dissipation", *Geophysics* 47(1), 16-24 (1982).
- [60] Stacey, F.D., Gladwin, M.T., McKavanagh, B., Linde, A.T., Hastie, L.M., "Anelastic damping of acoustic and seismic pulses", *Geophysical Surveys* 2, 133-151 (1975).
- [61] Stoll, R.D., "Acoustic waves in ocean sediments", *Geophysics* 42(4), 715-725 (1977).
- [62] Stoll, R.D., "Marine sediment acoustics", *J. Acoust. Soc. Am.* 77(5), 1789-1799 (1985).
- [63] Tullis, F.N., Reid, A.C., "Seismic attenuation of Gulf Coast sediments", *Geophysics* 34(4), 516-528 (1969).
- [64] Twomey, S., *Introduction to the Mathematics of Inversion in Remote Sensing and Indirect Measurements*, Developments in Geomathematics 3, Elsevier, Amsterdam (1977).
- [65] Urlick, R.J., *Principles of Underwater Sound*, McGraw-Hill, New York (1983).
- [66] Wiggins, R.A., "General linear inverse problem - Implication of surface waves and free oscillations for earth structure", *Rev. Geophys. Space Physics* 10, 251-285 (1972).
- [67] Wilde, P., "Recent sediments of the Monterey deep-sea fan", Univ. of California Hydraulic Eng. Lab. Tech Report Hel-2-13, 153 pp. (1965).
- [68] Wingham, D.J., "The dispersion of sound in sediment", *J. Acoust. Soc. Am.* 78(5), 1757-1760 (1985).

- [69] Wonnacott, T.H., Wonnacott, R.J., *Regression: A Second Course in Statistics*, Wiley, New York (1981).
- [70] Wrolstad, K., "Interval velocity and attenuation measurements in sediments from marine seismic reflection data", *J. Acoust. Soc. Am.* 68(5), 1415-1435 (1980).

Appendix A1

Inverting $X(p)$, $T(p)$, and $\tau(p)$ data to obtain velocity as a function of depth

Introduction

In this appendix equations for inferring the velocity structure of a medium from $T(p)$, $X(p)$, or $\tau(p)$ data are developed. The end result will be a system of linear equations which, when inverted, will yield information about the velocity as a function of depth.

A general linear inverse problem

A general way of posing a linear inverse problem [64] is

$$d_i = \int_{u_0}^{u_j} K_i(u) m(u) du \quad i=1,2,\dots,N \quad (\text{A1.1})$$

d_i is the i^{th} data point, K_i is the data kernel for the i^{th} datum, and $m(u)$ is the model. The kernel represents what is known from the physics of the problem. Given a set of data d_i , the goal is to find the model $m(u)$ which generates that data.

One way of proceeding is to define the model as a linear combination

$$m(u) = \sum_{j=1}^M a_j F_j(u) \quad (\text{A1.2})$$

where the a_j are unknown parameters, and the $F_j(u)$ are specified in such a way as to construct the desired model. Substituting this expression for the model into the general form (A1.1) gives

$$d_i = \int_{u_0}^{u_j} \left[K_i(u) \sum_{j=1}^M a_j F_j(u) \right] du$$

$$= \sum_{j=1}^M a_j \int_{u_0}^{u_j} K_i(u) F_j(u) du \quad i=1,2,\dots,N \quad (\text{A1.3})$$

The kernel K_i is known and the F_j have been specified, so the integral may be

evaluated (either analytically or numerically) for each i and j . Let

$$g_{ij} = \int_{u_0}^{u_j} K_i(u) F_j(u) du$$

then (A1.3) may be written as

$$d_i = \sum_{j=1}^M a_j g_{ij} \quad i=1,2,\dots,N \quad (\text{A1.4})$$

which represents a set of N linear equations in M unknowns. In matrix notation this is $\mathbf{d} = \mathbf{G}\mathbf{a}$. There are N data and M unknown model parameters. \mathbf{d} is the data vector, \mathbf{G} is a known matrix, and \mathbf{a} is the unknown vector of model parameters. There are usually many more data than model parameters, producing a non-square, overdetermined system of linear equations. An extensive literature exists for solving this type of problem [1 (Sect. 12.3), 15, 39, 41, 57, 64, 66].

Ray propagation as an inverse problem

Consider a ray propagating through a medium whose velocity structure is laterally homogeneous, but vertically inhomogeneous (figure A1.1). $u(z)$, the reciprocal of velocity, is called slowness: $u(z) = 1/v(z)$. If the velocity increases (slowness decreases) with depth, then a ray leaving the surface $z = 0$ at angle θ_0 will refract as it travels through the layers, returning to the surface at a horizontal range of X from where it started. The time it takes to travel that distance is T seconds. The range X and time T for such a raypath is given by [8]

$$X_i(p) = 2p \int_0^{z_{TP}} \frac{dz}{[u^2(z) - p^2]^{1/2}} \quad (\text{A1.5})$$

$$T_i(p) = 2 \int_0^{z_{TP}} \frac{u^2(z)}{[u^2(z) - p^2]^{1/2}} dz \quad (\text{A1.6})$$

Subscripts on X and T indicate the i^{th} ray ($i=1,2,\dots,N$). Subscripts on X and T indicate the i^{th} ray ($i=1,2,\dots,N$). A commonly used linear combination of $X(p)$ and $T(p)$, called the delay time, is defined by

$$\begin{aligned} \tau_i(p) &= T_i(p) - pX_i(p) \\ &= 2 \int_0^{z_{TP}} \left[\frac{u^2(z)}{[u^2(z) - p^2]^{1/2}} - \frac{p^2}{[u^2(z) - p^2]^{1/2}} \right] dz \end{aligned}$$

$$= 2 \int_0^{z_{TP}} [u^2(z) - p^2]^{1/2} dz \quad (\text{A1.7})$$

In the above equations p is the ray parameter, defined as $p = u(0) \sin(\theta_0)$, where $u(0)$ is the slowness at the surface $z=0$, and θ_0 is the takeoff angle (the angle the ray makes with the vertical at the surface). If the medium is laterally homogeneous and horizontally layered, then p is constant along the entire raypath: $p = u \sin(\theta)$. In this case the ray parameter uniquely defines a ray. z_{TP} is the depth at which the ray turns (see figure A1.1). Due to symmetry, the total range and time is twice the range and time at the turning point (midpoint of the ray path). The limits of the integrals go from $z=0$ to $z=z_{TP}$, so multiplication by a factor of two is required to obtain values for the entire raypath.

Equations A1.5, A1.6, and A1.7 define the forward problem. Given a slowness profile $u(z)$ and a ray parameter p , the time T , horizontal range X , and delay time τ for the raypath may be found by evaluating the integrals. The inverse problem is: given a set of range or time data, what can be inferred about the slowness (velocity) profile.

A model which has received considerable use is one having constant velocity layers. A model that has layers of constant velocity is not very realistic and often produces physically unreasonable results. A more realistic model may be constructed if each layer is assumed to have a constant velocity (slowness) gradient rather than a constant velocity (see figure A1.2). Thus, the 0_j^{th} layer would have a constant slowness gradient of $(du/dz)_j$. Use of this model will first be considered for $X(p)$.

Before proceeding, a change of notation will be made to make the discrete nature of the data more explicit. Given the assumption of a laterally homogeneous, horizontally layered medium, each arrival is uniquely specified by a ray parameter p . In view of this, let the i^{th} datum be given by $X(p_i)$. Then, changing the variable of integration from depth z to slowness u in (A1.5) results in

$$X(p_i) = 2p_i \int_{u_0}^{u_{TP}} \frac{\left(\frac{dz}{du}\right)}{(u^2 - p_i^2)^{1/2}} du \quad (\text{A1.8})$$

In the notation of equation A1.1 the kernel is $\frac{2p_i}{(u^2 - p_i^2)^{1/2}}$ and the model is $\left(\frac{dz}{du}\right)$, the inverse of the slowness gradient. The limits now go from slowness at the surface (u_0) to slowness at the turning point (u_{TP}). Next, as in equation A1.2, define the model to be

$$\frac{dz}{du} = \sum_{j=1}^M \omega_j F_j(u) \quad \text{with } F_j(u) = \begin{cases} 1 & \text{if } u_j \leq u \leq u_{j-1} \\ 0 & \text{otherwise} \end{cases} \quad (\text{A1.9})$$

and $\omega_j = \left(\frac{dz}{du}\right)_j$, the inverse slowness gradient in the j^{th} layer. This essentially breaks the medium up into M layers, modeling each layer with a constant, ω_j . There are $M+1$ interfaces (specified by u_0, u_1, \dots, u_M) to define the M layers. Slowness is assumed to decrease with depth (or, equivalently, velocity increases with depth). Substitution of the model (A1.9) into (A1.8) yields a form similar to (A1.3)

$$\begin{aligned} X(p_i) &= \int_{u_0}^{u_{TP}} \left[\frac{2p_i}{(u^2 - p_i^2)^{1/2}} \sum_{j=1}^M \omega_j F_j(u) \right] du \\ &= \sum_{j=1}^M \omega_j \left[2p_i \int_{u_{j-1}}^{u_j} \frac{du}{(u^2 - p_i^2)^{1/2}} \right] \end{aligned} \quad (\text{A1.10})$$

The limits on the integral extend only over the j^{th} layer since $F_j(u) = 0$ unless $u \in [u_j, u_{j-1}]$. The integral may now be evaluated.

$$\begin{aligned} \int_{u_{j-1}}^{u_j} \frac{du}{(u^2 - p_i^2)^{1/2}} &= \ln \left[u + (u^2 - p_i^2)^{1/2} \right] \Big|_{u_{j-1}}^{u_j} \\ &= \ln \left[u_j + (u_j^2 - p_i^2)^{1/2} \right] - \ln \left[u_{j-1} + (u_{j-1}^2 - p_i^2)^{1/2} \right] \\ &= \ln \left[\frac{u_j + (u_j^2 - p_i^2)^{1/2}}{u_{j-1} + (u_{j-1}^2 - p_i^2)^{1/2}} \right] \end{aligned}$$

The limits are correct if the ray crosses the j^{th} interface. If the ray turns before the j^{th} interface (i.e. if $p_i > u_j$) then the upper limit should be p_i instead of u_j , otherwise the quantity $(u_j^2 - p_i^2)^{1/2}$ becomes negative. At the turning point, the ray is horizontal and $\theta_{TP} = \pi$. Since $p = u \sin(\theta)$ everywhere along the raypath, at the turning point $u = p$. Define $u_{\max} = \max(p_i, u_j)$ so that the upper limit is either u_j , the slowness at the j^{th} interface if the ray crosses it, or p , the slowness at the turning point if the ray turns before the j^{th} interface. Define g_{ij} to be the quantity in brackets from equation A1.10 and we have

$$\begin{aligned} g_{ij} &= 2p_i \int_{u_{j-1}}^{u_j} \frac{du}{(u^2 - p_i^2)^{1/2}} \\ &= 2p_i \ln \left[\frac{u_{\max} + (u_{\max}^2 - p_i^2)^{1/2}}{u_{j-1} + (u_{j-1}^2 - p_i^2)^{1/2}} \right] \quad u_{\max} = \max(p_i, u_j) \end{aligned} \quad (\text{A1.11})$$

Substitution of this result into (A1.10) gives the system of linear equations A1.4.

$$X(p_i) = \sum_{j=1}^M \omega_j g_{ij}$$

In matrix form this is

$$\begin{bmatrix} X(p_1) \\ X(p_2) \\ X(p_3) \\ \cdot \\ \cdot \\ \cdot \\ X(p_N) \end{bmatrix} = \begin{bmatrix} g_{11} & g_{12} & g_{13} & \cdot & \cdot & \cdot & g_{1M} \\ g_{21} & g_{22} & g_{23} & \cdot & \cdot & \cdot & g_{2M} \\ g_{31} & g_{32} & g_{33} & \cdot & \cdot & \cdot & g_{3M} \\ \cdot & \cdot & \cdot & & & & \cdot \\ \cdot & \cdot & \cdot & & & & \cdot \\ \cdot & \cdot & \cdot & & & & \cdot \\ g_{N1} & g_{N2} & g_{N3} & \cdot & \cdot & \cdot & g_{NM} \end{bmatrix} \begin{bmatrix} \omega_1 \\ \omega_2 \\ \omega_3 \\ \cdot \\ \cdot \\ \cdot \\ \omega_M \end{bmatrix}$$

which may be written more compactly as

$$\mathbf{x} = \mathbf{G} \mathbf{w} \tag{A1.12}$$

Vector \mathbf{w} contains the reciprocals of the unknown slowness gradients $(\frac{du}{dz})_j$, \mathbf{x} contains the data, and matrix \mathbf{G} is a known matrix whose elements (for the i^{th} datum and the j^{th} layer) are given by (A1.11). The model generally has a few layers, while there are many more X , T , or τ data. This results in an overdetermined system of equations.

An expression for $\tau(p_i)$ is found in a similar manner. Changing variables in (A1.7) and using the model parameterization in (A1.9) gives

$$\begin{aligned} \tau(p_i) &= 2 \int_{u_0}^{u_{TP}} (u^2 - p_i^2)^{1/2} \left(\frac{dz}{du} \right) du \\ &= 2 \int_{u_0}^{u_{TP}} (u^2 - p_i^2)^{1/2} \left[\sum_{j=1}^M \omega_j F_j(u) \right] du \end{aligned}$$

$$= \sum_{j=1}^M \omega_j \left[2 \int_{u_{j-1}}^{u_j} (u^2 - p_i^2)^{1/2} du \right] \quad (\text{A1.13})$$

The integral is evaluated as

$$\begin{aligned} 2 \int_{u_{j-1}}^{u_j} (u^2 - p_i^2)^{1/2} du &= \left[u (u^2 - p_i^2)^{1/2} - p_i^2 \ln[u + (u^2 - p_i^2)^{1/2}] \right]_{u_{j-1}}^{u_j} \\ &= u_j (u_j^2 - p_i^2)^{1/2} - u_{j-1} (u_{j-1}^2 - p_i^2)^{1/2} \\ &\quad - p_i^2 \left[\ln[u_j + (u_j^2 - p_i^2)^{1/2}] - \ln[u_{j-1} + (u_{j-1}^2 - p_i^2)^{1/2}] \right] \end{aligned}$$

With u_{\max} defined as before in case the ray turns prior to the j^{th} interface.

$$\begin{aligned} g_{ij} &= 2 \int_{u_{j-1}}^{u_j} (u^2 - p_i^2)^{1/2} du \\ &= u_{\max} (u_{\max}^2 - p_i^2)^{1/2} - u_{j-1} (u_{j-1}^2 - p_i^2)^{1/2} \\ &\quad - p_i^2 \ln \left[\frac{u_{\max} + (u_{\max}^2 - p_i^2)^{1/2}}{u_{j-1} + (u_{j-1}^2 - p_i^2)^{1/2}} \right] \end{aligned} \quad (\text{A1.14})$$

Equation A1.13 is the matrix equation for $\tau(p)$ data, $\tau = \mathbf{G}\mathbf{w}$, with elements of \mathbf{G} given by (A1.14).

$T(p)$ may be found by re-arranging the top equation of (A1.7).

$$T(p_i) = p_i X(p_i) + \tau(p_i)$$

Using (A1.11) for $X(p_i)$ and (A1.14) for $\tau(p_i)$ results in

$$T(p_i) = \sum_{j=1}^M \omega_j \left[u_{\max} (u_{\max}^2 - p_i^2)^{1/2} - u_{j-1} (u_{j-1}^2 - p_i^2)^{1/2} + p_i^2 \ln \left[\frac{u_{\max} + (u_{\max}^2 - p_i^2)^{1/2}}{u_{j-1} + (u_{j-1}^2 - p_i^2)^{1/2}} \right] \right] \quad (\text{A1.15})$$

The matrix equation is $\mathbf{T} = \mathbf{G}\mathbf{w}$. In this case the data vector consists of times $T(p_i)$, and g_{ij} is defined by the quantity in the outer brackets.

In each case (equations A1.10, A1.13, and A1.15) the medium is broken up into M layers. The model is constructed by picking values of slowness (u_j) to specify the $M+1$ interfaces. Slowness at the surface sets the first interface ($j=0$). The last interface ($j=M$) should be set slightly below the turning point of the deepest ray (i.e. u_M should be less than the smallest ray parameter p) so that the ray turns in the last layer.

The solution contains reciprocals of the slowness gradients for each of the M layers. Velocity as a function of depth is recovered by first finding the layer thicknesses from slowness values at the interfaces and the slowness gradients. The thickness of the j^{th} layer may be found as

$$(dz)_j = \frac{(du)_j}{(du/dz)_j} = (u_j - u_{j-1}) \omega_j$$

Depth from the surface to any interface is then found by integrating the layer thicknesses to that interface, yielding velocity as a function of depth.

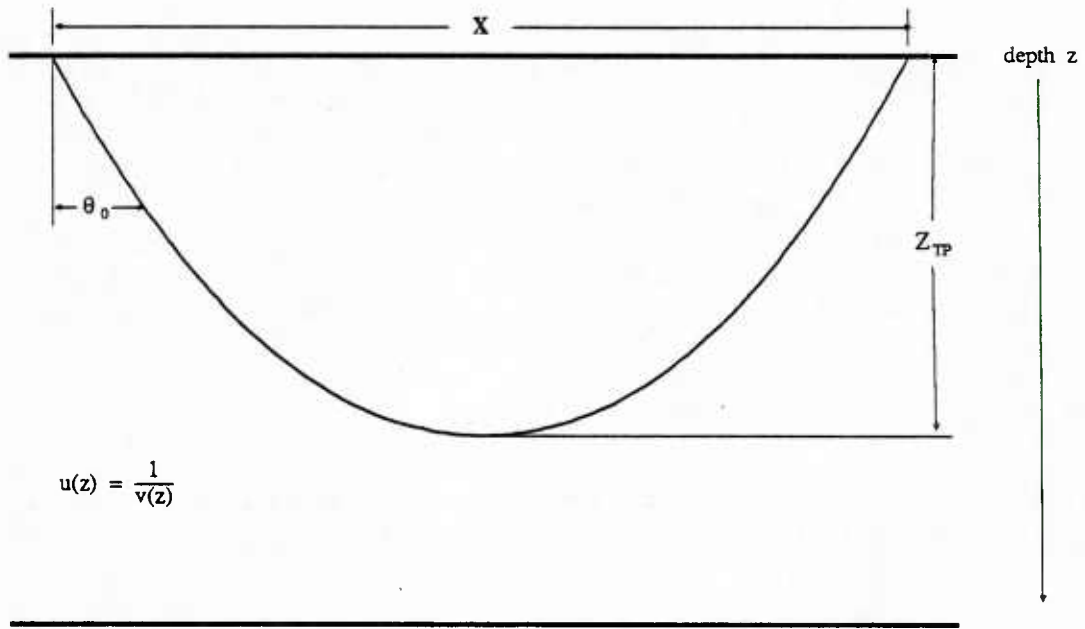


Figure A1.1 Raypath through a laterally homogeneous but vertically inhomogeneous medium. Slowness is assumed to decrease with depth (or equivalently, velocity increases with depth). Shows the ray's turning point, take-off angle, and range. Depth at the surface is $z=0$, slowness is $u(0)$.

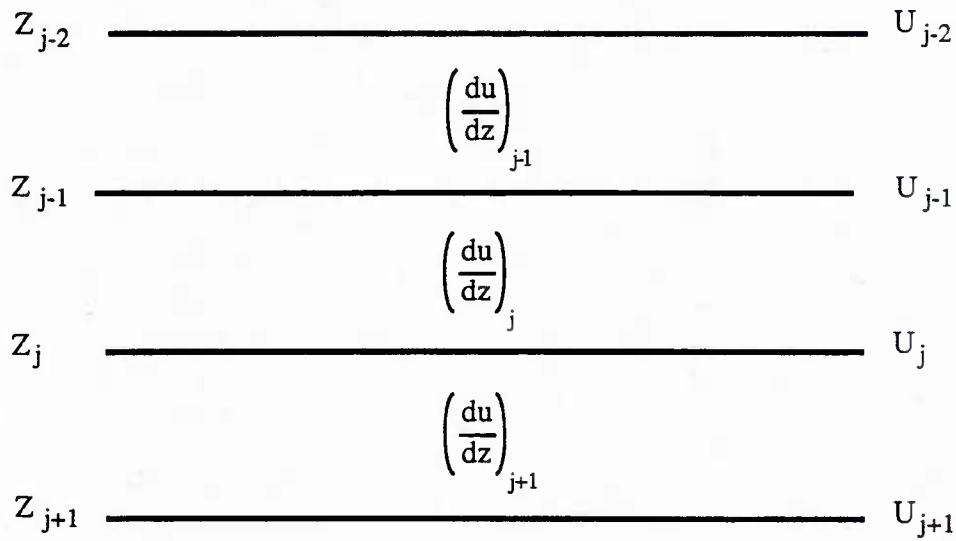


Figure A1.2 Constant gradient model. Each layer has a constant slowness gradient.

Appendix A2

The method of spectral ratios

Amplitude loss in an attenuating medium

Consider a signal that propagates through a layer of an attenuating medium as shown in Figure A2.1. The pathlength (layer thickness in this case) is given by s . Let the amplitude spectrum of the source be given by $A_0(f)$, and the amplitude spectrum of the received time series be $A(f, s)$. The input and output are related by the transfer function $H(f, s)$.

$$A(f, s) = A_0(f)H(f, s) \quad (\text{A2.1})$$

$H(f, s)$ is itself made up of a number of functions which describe the changes the signal undergoes as it propagates through the layer. In general, it will be a function of the pathlength and frequency. The received waveform, after traveling through a layer of sediment, can be modeled as

$$A(f, s) = A_0(f)H(f, s) = A_0(f) \left[I(f) T(s) G(s) L(f, s) \right] \quad (\text{A2.2})$$

where

$A(f, s)$	is the amplitude spectrum of the received signal
$A_0(f)$	is the amplitude spectrum of the source
$I(f)$	is the instrument response
$T(s)$	represents all frequency independent losses (reflection & transmission coefficients, scattering, etc.)
$G(s)$	represents geometrical spreading
$L(f, s)$	is the attenuation operator (includes all frequency dependent attenuation)

Attenuation in the water column is negligible at low frequencies [36, 65 (pg. 106)], so a good representation of $A_0(f)$ can be obtained from the direct water path. The spectrum of the direct water path may be modeled as

$$A_w(f, s_w) = A_0(f) I(f) G_w(s_w), \quad (\text{A2.3})$$

where $G_w(s_w)$ is geometrical spreading and s_w is the pathlength for the direct water path. By dividing the spectrum of the sediment refracted arrival (A2.2) by the spectrum of the direct water path arrival (A2.3), factors involving the source spectrum and instrument response are eliminated.

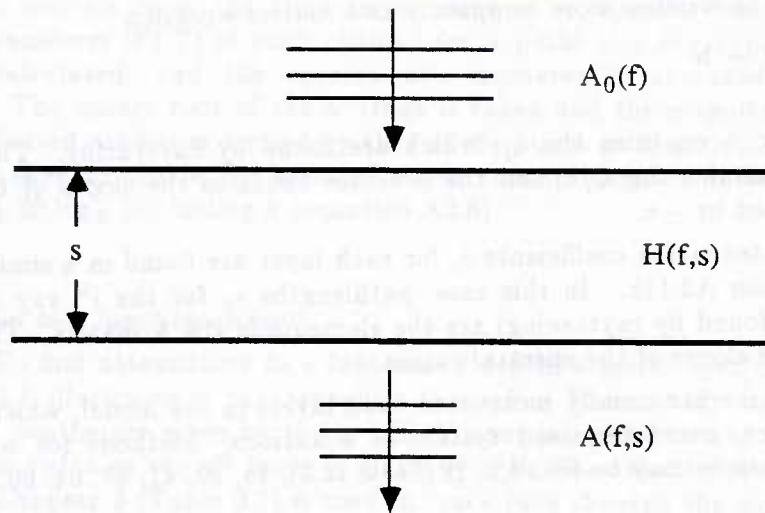


Figure A2.1 Plane wave propagating through an attenuating medium.

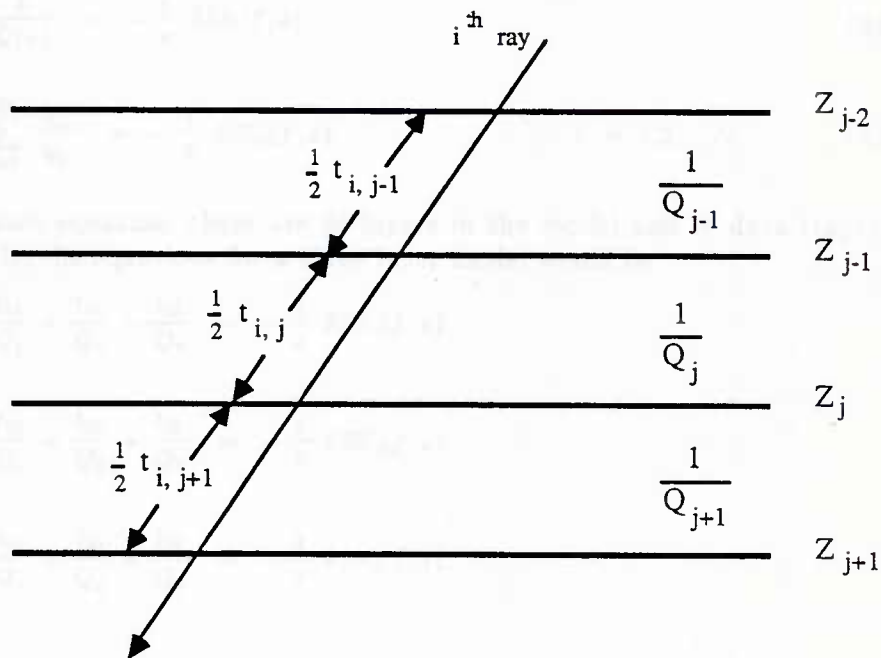


Figure A2.2 Ray propagating through a horizontally layered, attenuating medium.

ONR/MPL GENERAL DISTRIBUTION LIST

Chief of Naval Research
Department of the Navy
Arlington, Virginia 22217-5000
Code 12, 122(2), 102C
111, 112, 113,
1122PO, 425-AC, 460

ONRDET
NSTL Station
Bay St. Louis, Mississippi 39529-5004
Code 112, 1121, 1123CS, 422CB,
1122PO, 1125GG

Director
Office of Naval Research
Branch Office
1030 East Green Street
Pasadena, California 91106-2485

Commander
Naval Sea Systems Command
Washington, D. C. 20362
Code 63, 63R, 63R-23

Commanding Officer
Naval Ocean Research and
Development Activity
NSTL Station
Bay, St. Louis, Mississippi 39529-5004
Code 100, 110, 300, 330,
340, 350, 360, 500

Commander
U.S. Naval Oceanographic Office
STL Station
y St. Louis, Mississippi 39522-5004
Atten: Bill Jobst

Assistant Secretary of the Navy
(Research Engineering & Systems)
Department of the Navy
Washington, D. C. 20350

Defense Advanced Res. Proj. Agency
TTO - Tactical Technology Office
1400 Wilson Boulevard
Arlington, Virginia 22209-2308
Atten: Capt. Kirk Evans

National Oceanic & Atmospheric
Administration
Ocean Engineering Office
6001 Executive Boulevard
Rockville, Maryland 20852

Commander
Space and Naval Warfare
Systems Command
Washington, D. C. 20360
Code PDW-124, 320A

Commander
Naval Ship Res. & Dev. Center
Bethesda, Maryland 20084

Executive Secretary
Naval Studies Board
National Academy of Sciences
2101 Constitution Avenue, N.W.
Washington, D.C. 20418

Director
Strategic Systems Proj. Ofc. (PM-1)
Department of the Navy
Washington, D. C. 20361
Code NSP-2023

Commander
Naval Ocean Systems Center
San Diego, California 92152
Code 00, 01, 16, 94, 531
5301, 71, 72

Commander
Submarine Development Group ONE
Fleet Post Office
San Diego, California 92152

Commanding Officer
Civil Engineering Laboratory
Naval Construction Battalion Center
Port Hueneeme, California 93043
Code L40, L42

Commanding Officer
Naval Underwater Systems Center
Newport, Rhode Island 02844
Atten: Dr. K. A. Kemp, Code 8213

Officer in Charge
Naval Underwater Systems Center
New London Laboratory
New London, Connecticut 06320
Code 900, 905, 910, 930, 960

Director of Research
U.S. Naval Research Laboratory
Washington, D. C. 20375
Code 2620, 2627, 5000, 5100, 5800

Commander
Naval Surface Combat Systems Center
White Oak
Silver Spring, Maryland 20910

Commanding Officer
Naval Coastal Systems Laboratory
Panama City, Florida 32401

STOIA
Battelle Columbus Laboratories
505 King Avenue
Columbus, Ohio 43201

Commander
Naval Air Systems Command
Washington, D. C. 20361
Code 370

Commanding Officer
U.S. Naval Air Development Center
Attention: Jim Howard
Warminster, Pennsylvania 18974

Director
Defense Documentation Center
(TIMA), Cameron Station
5010 Duke Street
Alexandria, Virginia 22314

Institute for Defense Analyses
1801 North Beaugard Street
Arlington, Virginia 22311

Superintendent
U.S. Naval Postgraduate School
Monterey, California 93940

Chief Scientist
Navy Underwater Sound Reference Div.
U.S. Naval Research Laboratory
P.O. Box 8337
Orlando, Florida 32806

Supreme Allied Commander
U.S. Atlantic Fleet
ASW Research Center, APO
New York, New York 09019
Via: ONR 100 M, CNO OP092D1,
Secretariat of Military,
Information Control, Committee

Director
Institute of Marine Science
University of Alaska
Fairbanks, Alaska 99701

Director
Applied Physics Laboratory
Johns Hopkins University
Johns Hopkins Road
Laurel, Maryland 20810
Atten: J. R. Austin

Director
College of Engineering
Department of Ocean Engineering
Florida Atlantic University
Boca Raton, Florida 33431

Director
Marine Research Laboratories
c/o Marine Studies Center
University of Wisconsin
Madison, Wisconsin 53708

Director
Applied Research Laboratory
Pennsylvania State University
P.O. Box 30
State College, Pennsylvania 16802

Director
Applied Physics Laboratory
University of Washington
1013 East 40th Street
Seattle, Washington 98105

Director
The Univ. of Texas at Austin
Applied Research Laboratory
P.O. Box 8029
Austin, Texas 78712

Director
Lamont-Doherty Geological Observatory
Torrey Cliff
Palisades, New York 10964

Director
Woods Hole Oceanographic Institution
Woods Hole, Massachusetts 02543

Director
Inst. of Ocean Science Engineering
Catholic University of America
Washington, D.C. 20017

National Science Foundation
Washington, D. C. 20550

Office of Naval Research
Resident Representative
c/o Univ. of California, San Diego
Mail Code Q023
La Jolla, California 92093

University of California, San Diego
Marine Physical Laboratory
Branch Office
La Jolla, California 92093

DUDLEY KNOX LIBRARY - RESEARCH REPORTS



5 6853 01077944 0

U234553